

# Model Validation and Inversion of Active Implantable Medical Devices

by  
Zhichao Wang

A dissertation submitted to the Department of Electrical and Computer  
Engineering,

Cullen College of Engineering

in partial fulfillment of the requirements for the degree of

Doctor of Philosophy  
in Electrical and Computer Engineering

Chair of Committee: Ji Chen

Committee Member: David Jackson

Committee Member: Jiefu Chen

Committee Member: Benhaddou Driss

Committee Member: Wolfgang Kainz

University of Houston  
May 2020

Copyright 2020, Zhichao Wang

## ACKNOWLEDGMENTS

I would like to give special thanks to my advisor Prof. Ji Chen. He has been providing guidance and support since I came to the USA. Without his guidance and suggestions, my research would not be complete. I would also like to express deep appreciation to the members of my dissertation committee: Dr. David Jackson, Dr. Jiefu Chen, Dr. Driss Benhaddou, and Dr. Wolfgang Kainz for their time and commitment, Their assistance and suggestions are important to my research. I would like to thank the colleagues and friends: Dr. Qingyan Wang, Dr. Jianfeng Zheng, Dr. Qi Zeng, Dr. Ran Guo, Dr. Xiaohe Ji, Dr. Dagang Wu, Dr. Zubiao Xiong, Dr. Yibo Wang, Mr. Yu Wang, Mr. Rui Yang, Mr. Shuo song, Mr. Qianlong Lan, Mr. Jiajun Chang, Ms. Meiqi Xia, Ms. Mengpin Yu, and Mr. Wei Hu for their kindness and friendship. With their company, graduate study life was full of passion and pleasure. Finally, I would like to thank my family and my girlfriend for always being supportive and providing encouragement. I am grateful for their love and support.

## ABSTRACT

The model validation and inversion for active implantable medical devices (AIMD) used for safety evaluations under magnetic resonance imaging (MRI) radio frequency (RF) coil emission were discussed. A mathematical derivation is presented to provide guidance on selecting meaningful pathways for the model validation. Suggested validation pathways from current ISO 10974 are used as examples. It is shown that these standard pathways are 1) inefficient since validations from several pathways are theoretically redundant and 2) incomplete or false since significantly different AIMD models can have identical validation outputs. Based on the developed guidance, two sets of pathways are proposed. It is demonstrated that for efficient and correct model validation, the tangential components of the incident fields along validation pathways should be orthogonal to each other or at least has low correlations between each other. These guidelines can be implemented for future AIMD model validations in ISO 10974. Based on the transmission line model, the AIMD model can be developed semi-analytically using a few direct measurements inside the ASTM phantom. Folded orthogonal pathways based on the Hadamard matrix are used in the model development to make the problem of the AIMD model development to be well-conditioned. Both induced voltage and heating models for the example AIMDs were developed to demonstrate the effectiveness of this method. Furthermore, the optimized validation pathways were designed according to a given AIMD model in a high electric field generator to make sure the validation pathways sufficient and have high signal noise ratios. Still, the circular validation pathways were proposed to be relevant to the clinical validation pathways.

# TABLE OF CONTENTS

<b>ACKNOWLEDGMENTS</b>	<b>iii</b>
<b>ABSTRACT</b>	<b>iv</b>
<b>LIST OF TABLES</b>	<b>vii</b>
<b>LIST OF FIGURES</b>	<b>xii</b>
<b>1 INTRODUCTION</b>	<b>1</b>
1.1 Current Regulations for RF-induced Heating and Voltage by AIMD . . . . .	2
1.2 Motivation . . . . .	3
1.3 Overview . . . . .	4
<b>2 ON THE MODEL VALIDATION OF ACTIVE IMPLANTABLE MEDICAL DEVICE FOR MRI SAFETY ASSESSMENT</b>	<b>5</b>
2.1 RF-Induced Voltage and Heating for AIMD in MRI system . . . . .	5
2.2 Methodology . . . . .	6
2.2.1 AIMD Model and Model Validation . . . . .	6
2.2.2 Matrix Expression . . . . .	8
2.2.3 Spurious AIMD Models . . . . .	10
2.3 Validation with ISO 10974 Pathways . . . . .	11
2.3.1 Standard Pathways for AIMD Model Validation . . . . .	12
2.4 Appropriate Pathways for Validation . . . . .	20
2.5 Discussion . . . . .	29
<b>3 DEVELOPING AIMD MODELS USING ORTHOGONAL PATH- WAYS FRO MRI SAFETY ASSESSMENT</b>	<b>33</b>
3.1 Introduction . . . . .	33
3.2 Methodology . . . . .	35

3.2.1	Voltage AIMD Model Development . . . . .	35
3.2.2	Selection of Appropriate Pathways . . . . .	36
3.2.3	Characteristic Impedance . . . . .	40
3.3	Experimental Studies . . . . .	43
3.3.1	AIMD Model for Induced Voltage . . . . .	44
3.3.2	AIMD Model for Induced Heating . . . . .	48
3.4	Optical Fiber Effects on the AIMD model . . . . .	54
3.4.1	Numerical Study . . . . .	54
3.4.2	Experimental Validation . . . . .	57
3.4.3	Discussion . . . . .	59
3.5	Bending Effects on the AIMD Model . . . . .	59
3.5.1	Numerical Study . . . . .	61
3.5.2	Experimental Validation . . . . .	66
3.6	The AIMD Model Mode Discussion . . . . .	75
3.6.1	The Fourier Transform of the AIMD Model . . . . .	75
3.6.2	Numerical Study . . . . .	76
3.7	Discussion . . . . .	79
<b>4</b>	<b>Optimized Design based on the AIMD Model</b>	<b>80</b>
4.1	Optimized Validation Pathways . . . . .	80
4.2	Numerical Study . . . . .	81
4.3	Discussion . . . . .	91
<b>5</b>	<b>CONCLUSIONS</b>	<b>93</b>
	<b>References</b>	<b>94</b>
<b>A</b>	<b>Appendix</b>	<b>102</b>

# LIST OF TABLES

1	Excitation and Phantom Type of Pathways. . . . .	14
2	The Wave Number and Reflection Coefficient of the AIMD model along Different Pathways. . . . .	66
3	The Wave Number of Different Orders at Different Frequencies. . . . .	78
4	The Induced Voltage Ratio of the Optimized Validation Pathways. . . . .	88

# LIST OF FIGURES

2.1	The ISO 10974 standard advised pathways (pathway 1-5 and 11 are in the linear polarization coil; pathway 6-8 and 10-11 are in the quadrature polarization coil). . . . .	13
2.2	The generic birdcage coil. . . . .	14
2.3	(a) Magnitude of the tangential electric field along the standard pathways; (b) Phase of the tangential electric field along the standard pathways. . . . .	16
2.4	(a) Singular values of the tangential electric field matrix; (b) Magnitude of first six tangential electric field matrix eigenvectors; (c) Phase of first six tangential electric field matrix eigenvectors. . . . .	17
2.5	(a) Magnitude of $\mathbf{TF}_1$ and $\mathbf{TF}_2$ ; (b) Phase of $\mathbf{TF}_1$ and $\mathbf{TF}_2$ . . . . .	18
2.6	(a) Amplitude of induced voltages for $\mathbf{TF}_1$ and $\mathbf{TF}_2$ along the standard validation pathways; (b) Phase of induced voltages for $\mathbf{TF}_1$ and $\mathbf{TF}_2$ along the standard validation pathways. . . . .	19
2.7	(a) Magnitude of $\mathbf{TF}_1$ and $\mathbf{TF}_3$ ; (b) Phase of $\mathbf{TF}_1$ and $\mathbf{TF}_3$ . . . . .	21
2.8	(a) Amplitude of induced voltages for $\mathbf{TF}_1$ and $\mathbf{TF}_3$ along the standard validation pathways; (b) Phase of induced voltages for $\mathbf{TF}_1$ and $\mathbf{TF}_3$ along the standard validation pathways. . . . .	22
2.9	(a) Illustration of V-shaped pathways based on (2.9); (b) Illustration of the pathway position respective to the ASTM phantom. . . . .	23
2.10	(a) Magnitude of the tangential components of the incident field along the V-shaped orthogonal pathways; (b) Phase of the tangential components of the incident field along the V-shaped orthogonal pathways. . . . .	24
2.11	(a) Singular values of the V-shaped tangential electric field matrix; (b) Magnitude of the V-shaped tangential electric field matrix eigenvectors; (c) Phase of the V-shaped tangential electric field matrix eigenvectors. . . . .	25

2.12	(a) Amplitude of induced voltages $\mathbf{TF}_1$ , $\mathbf{TF}_2$ and $\mathbf{TF}_3$ along the V-shaped orthogonal validation pathways; (b) Phase of induced voltages $\mathbf{TF}_1$ , $\mathbf{TF}_2$ and $\mathbf{TF}_3$ along the V-shaped orthogonal validation pathways.	26
2.13	(a) Illustration of U-shaped pathways based on (2.9); (b) Illustration of the pathway position respective to the ASTM phantom. . . . .	27
2.14	(a) Magnitude of the tangential components of the incident field along the U-shaped orthogonal pathways; (b) Phase of the tangential components of the incident field along the U-shaped orthogonal pathways.	28
2.15	(a) Singular values of the U-shaped tangential electric field matrix; (b) Magnitude of the U-shaped tangential electric field matrix eigenvectors; (c) Phase of the U-shaped tangential electric field matrix eigenvectors.	30
2.16	(a) Amplitude of induced voltages $\mathbf{TF}_1$ , $\mathbf{TF}_2$ and $\mathbf{TF}_3$ along the U-shaped orthogonal validation pathways; (b) Phase of induced voltages $\mathbf{TF}_1$ , $\mathbf{TF}_2$ and $\mathbf{TF}_3$ along the U-shaped orthogonal validation pathways.	31
3.1	The relation between the $\mathbf{E}_{tan}$ , $\mathbf{TF}$ and $\mathbf{V}_{ind}$ . . . . .	39
3.2	The cross section of the infinite dielectric coating wire in homogeneous space. . . . .	41
3.3	MITS 1.5 System. (a) Amplifiers and software parts; (b) RF gradient coil. . . . .	44
3.4	Plastic mesh grid used for fixing the lead. . . . .	45
3.5	(a) Magnitude of the tangential components of the incident fields along U-shaped folded pathways; (b) Phase of the tangential components of the incident fields along U-shaped folded pathways; (c) Eigenvalues of the tangential components of the incident field. . . . .	46
3.6	Comparison of voltage transfer functions through proposed method and reciprocity method (a) Magnitude of AIMD models, (b) Phase of AIMD models. . . . .	47

3.7	Comparison of induced voltages from direct measurement in ASTM phantom and predicted ones using the AIMD model developed in the study. . . . .	48
3.8	(a) Z-shaped validation pathways; (b) Pathway position in ASTM phantom. . . . .	49
3.9	(a) Comparison of induced voltages between estimation with AIMD model using reciprocity method, estimation with proposed AIMD model and directly measured voltage in ASTM phantom; (b) the relative errors between direct measurement and estimation from different AIMD models. . . . .	50
3.10	(a) Magnitude of the tangential components of the incident fields along U-shaped folded pathways; (b) Phase of the tangential components of the incident fields along U-shaped folded pathways; (c) Eigenvalues of the tangential components of the incident fields. . . . .	52
3.11	Comparison of heating transfer functions through proposed method and reciprocity method (a) Magnitude of AIMD models, (b) Phase of AIMD models. . . . .	53
3.12	Comparison of induced temperature rises from direct measurement and predicted ones using the AIMD model developed in the study. . . . .	54
3.13	(a) Comparison of induced heating between estimation with AIMD model using reciprocity method, estimation with proposed AIMD model and directly measured voltage in ASTM phantom; (b) the relative errors between direct measurement and estimation from different AIMD models. . . . .	55
3.14	Lead model of the insulated solid wire. . . . .	56
3.15	The insulated solid lead with an optic fiber. . . . .	56
3.16	(a) The AIMD model amplitude of the lead only and the lead with an optic fiber attached in simulation; (b) the AIMD model phase of the lead only and the lead with an optic fiber attached in simulation. . . . .	58
3.17	The AIMD model measurement setup of the lead with an optic fiber. . . . .	59

3.18	(a)The AIMD model shape amplitude of the lead only and the lead with an optic fiber attached in experiment; (b) the AIMD model shape phase of the lead only and the lead with an optic fiber attached in experiment. . . . .	60
3.19	Simulation model of the insulated solid lead. . . . .	61
3.20	Lead path of the insulated solid lead. . . . .	62
3.21	(a) Amplitude of the AIMD model along S, L and U pathway in simulation; (b)Phase of the AIMD model along S, L and U pathway in simulation. . . . .	63
3.22	Lead path of the insulated solid lead. . . . .	64
3.23	(a) Amplitude of the AIMD model along S pathway by simulation and curve fitting; (b)Phase of the AIMD model along S pathway by simulation and curve fitting. . . . .	65
3.24	(a) Amplitude of the AIMD model along L pathway by simulation and curve fitting; (b)Phase of the AIMD model along L pathway by simulation and curve fitting. . . . .	67
3.25	(a) Amplitude of the AIMD model along U pathway by simulation and curve fitting; (b)Phase of the AIMD model along U pathway by simulation and curve fitting. . . . .	68
3.26	The insulated solid lead. . . . .	69
3.27	(a) Amplitude of the AIMD model for the insulated solid lead along S, L and U pathway in experiment; (b)Phase of the AIMD model for the insulated solid lead along S, L and U pathway in experiment. . . . .	70
3.28	The pathways of the insulated solid lead. . . . .	71
3.29	(a) Amplitude of the AIMD model for the helical winding lead along S, L and U pathway in experiment; (b)Phase of the AIMD model for the helical winding lead along S, L and U pathway in experiment. . . . .	72
3.30	The pathways of the insulated solid lead. . . . .	73

3.31	(a) Amplitude of the AIMD model for the helical winding lead along S and U pathway in experiment; (b)Phase of the AIMD model for the helical winding lead along S and U pathway in experiment. . . . .	74
4.1	The clinical pathway used in the deep brain stimulation. . . . .	81
4.2	(a) Amplitude of the AIMD model for the optimized validation pathways; (b)Phase of the AIMD model for the optimized validation pathways. . . . .	84
4.3	The statistic result for all possible pathways. . . . .	85
4.4	The optimized validation pathways. . . . .	86
4.5	The simulated electric field in the ASTM phantom. . . . .	86
4.6	The high electric field generating system. (a) The resonator structure; (b)The whole system constitution. . . . .	88
4.7	The simulated electric field in the box. . . . .	89
4.8	(a) Amplitude of the tangential components of the simulated incident field for the optimized validation pathways; (b)Phase of the tangential components of the simulated incident field for the optimized validation pathways. . . . .	90
4.9	The circular validation pathways. . . . .	91
4.10	(a) Amplitude of the tangential components of the simulated incident field for the circular validation pathways; (b)Phase of the tangential components of the simulated incident field for the circular validation pathways. . . . .	92

# 1 Introduction

Magnetic resonance imaging (MRI) has become an important means to obtain detailed anatomical information inside human bodies [1]. In the United States, more than 110 out of 1000 patients did MRI scans in 2017. For patients with pacemakers or implantable defibrillator system, many of them need MRI scans during the lifetime of their devices. However, patients with active implantable medical devices (AIMDs) are often prohibited from such procedures due to safety concerns [2]. Most of the issues are associated with the interaction between electromagnetic field produced by MR system and medical devices. In 2009, a set of MRI labeling terms for medical devices was developed and released [3]. This terminology, which is currently recognized by the Food and Drug Administration (FDA), is as follows: (a) MR Safe - an item that poses no known hazards in all MRI environments. (b) MR Conditional - an item that has been demonstrated to pose no known hazards in a specified MRI environment with specified conditions of use. Conditions that define the MRI environment may include the strength of the static magnetic field value, the spatial gradient magnetic field value, the time-varying magnetic field value, the radio frequency (RF) field value, and the specific absorption rate (SAR) level. Additional conditions, including the specific configuration for the item may be required. (c) MR Unsafe - an item that is known to pose hazards in all MRI environments

During MRI scans, the electromagnetic signals emitted by a RF coil can penetrate into human bodies and interact strongly with AIMDs [4]–[16]. The metallic part of pacemaker lead will collect energy and depositing it through the lead tip into human tissues or the proximal end of lead to the implantable pulse generator (IPG). The lead acts as an antenna and currents induced along the lead will cause two safety problems. One is related to the malfunction of the device injury. The induced voltage between

the device electrode and IPG can be high enough to damage the device circuitry [4]. Another concern is the heating induced by the RF field at the lead tip. The temperature rise may cause tissue damage [17]–[21]. RF-induced voltage and heating are the two major safety concerns for AIMD in the MRI environment. In this study, we focus on the RF-induced heating and voltage of AIMD.

## 1.1 Current Regulations for RF-induced Heating and Voltage by AIMD

To perform accurate safety assessment for induced voltage or the RF-induced heating, numerical and experimental investigations were performed [15]–[25]. The accurate full-wave modeling of AIMD is very challenging due to the submillimeter helical structures on lead conducting coils [26], especially when anatomical human models and the MRI RF coil need to be modeled together. *In vivo* measurements are often not feasible, either. Consequently, neither the experimental nor the numerical simulation approach alone is sufficient to assess the RF-induced heating or the RF-induced rectification voltage. The following standards are defined recently to assess safety of medical devices in MRI, especially in RF heating aspect.

The ASTM 2182 standard entitled Standard Test Method for Measurement of Radio Frequency Induced Heating On or Near Passive Implants during Magnetic Resonance Imaging covers measurements of RF induced heating on or near the AIMD during MRI. This test method assumes that testing is done on devices that will be entirely inside the body [27]. The ISO 10974 standard entitled Assessment of the safety of magnetic resonance imaging for patients with an active implantable medical device is applicable to implantable parts of active implantable medical devices (AIMDs) intended to be used in patients who undergo a magnetic resonance scan in

1.5 T [28].

Among the proposed methods as described in [27], [28], the transfer function (TF) method is widely used [24]. The transfer function approach divides the safety evaluation into two parts: 1) the development and validation of the AIMD model under the RF field [24], [25], and 2) the evaluation of incident electric fields inside the human bodies without electrodes. By integrating the AIMD model with the tangential components of the incident fields along the lead pathways, the induced voltage and heating can be estimated [29], [30].

## 1.2 Motivation

According to ISO 10974, the developed TF needs to be validated using clinical pathways or some other related ones to ensure the AIMD model can be used for all clinical relevant cases. It is observed that the tangential components of the incident fields along the suggested pathways are highly correlated. Using these validation pathways, two different AIMD models can be validated. Folded validation pathways based on the Hadamard matrix were proposed to address this problem. As the AIMD model can be taken as the transmission line model, three complex variables are needed to validate. In order to validate the AIMD model sufficiently, six sufficient validation pathways are needed according to the transmission line model at least. It is showed that accurate and sufficient validation can be done by using these validation pathways. After validation, the AIMD model can be inverted by performing the validation experiments. By using global searching algorithm, the unknown variable of the AIMD model based on the transmission line model can be calculated.

### 1.3 Overview

The remainder of the proposal is organized as follows. In Chapter 2, the model validation of the AIMD is discussed. Through eigenvalue analysis, the validation of the AIMD model was analyzed and discussed. In order to make sure the validation sufficient, the condition number of the tangential components of the incident field should be as small as possible. Two different AIMD model can be validated using the suggested pathways due to the high condition number. Two sets of validation pathways were proposed based on the Hadamard matrix to make the validation accurate and sufficient.

In Chapter 3, the AIMD model inverse based on the transmission line model was discussed. By using the folded validation pathways proposed in Chapter 2, the AIMD model can be inverted accurately. It is shown that the accuracy of the inverse is determined by the condition number of the tangential components of the incident fields.

In Chapter 4, optimized validation pathways were proposed to get high signal noise ratio and keep each validation pathway orthogonal to each other. By using the high E field generator, the optimized validation pathways were simulated and discussed. In order to make the validation more close to the clinical pathways, the circular validation pathways were proposed. Still, the condition number of them can be quite small.

Conclusions are drawn in Chapter 5.

## 2 On the Model Validation of Active Implantable Medical Device for MRI Safety Assessment

### 2.1 RF-Induced Voltage and Heating for AIMD in MRI system

To ensure the AIMD model can be used for all clinically relevant cases, extensive validation should be performed [28]. Several suggested pathways were proposed in ISO 10974 for AIMD model validation. The tangential components of the incident fields along the pathways should be extracted and combined with the AIMD models to estimate the induced temperature rises at the tip electrode or the induced voltage at the IPG side. Direct measurement of temperature rises or induced voltage should also be performed by placing AIMDs along the same pathways inside phantoms that are exposed to RF coil emissions. If the results of the direct measurement agree well with those predicted by the AIMD model, the model is considered to be validated.

However, it is observed that the tangential components of the incident fields along the suggested pathways often have simple phase variations [28]. It is our speculation that the tangential components of the incident fields along these pathways may be correlated with each other. This would lead to redundant validation and make the validation process inefficient. To examine the correlations among the the tangential components of the incident fields along these pathways, a rigorous eigenvalue decomposition method should be used [31]. Based on the results of eigen-analyses, we can derive a criterion on how to evaluate the effectiveness of the pathways for AIMD models. It is observed that if inappropriate pathways were selected for validation, two

different AIMD models can be validated along these pathways. To address these concerns, two sets of pathways based on the Hadamard matrix were proposed for accurate and effective AIMD model validation [32]. It showed that by using these specifically designed pathways, accurate and meaningful validation of the AIMD models can be achieved.

The remainder of this chapter is organized as follows. In Section 2, we present the theory on how to select appropriate pathways for AIMD model validation. In Section 3, numerical examples were used to show the deficiency of ISO 10974 pathways in AIMD model validation. In Section 4, two sets of pathways were proposed, and their effectiveness on model validation was presented. Discussion and conclusions were presented in Sections 4 and 5.

## 2.2 Methodology

In this section, the procedure of the AIMD model validation is presented in a matrix form. Through eigen-analysis, the basic requirement for pathway selection is proposed.

### 2.2.1 AIMD Model and Model Validation

To evaluate the AIMD device safety under MRI RF coil emission, the transfer function method described in ISO 10974 should be used [28]. The induced voltage near the IPG can be evaluated by [29], [30]

$$\begin{aligned}
 V_{ind} &= \int_L \vec{E}_{inc} \cdot TF d\hat{l} \\
 &= \int_L E_{tan} \times TF dl,
 \end{aligned}
 \tag{2.1}$$

where  $\vec{E}_{inc}$  is the incident electric field along a trajectory due to MRI RF coil emission,  $E_{tan}$  is the the tangential components of the incident fields along the path,  $TF$  is the AIMD model of the lead electrodes, and  $V_{ind}$  is the induced voltage. In discrete form, the induced voltage in (2.1) can be approximately calculated by

$$V_{ind} \approx \Delta l \sum_{i=1}^N E_{tan}(i) \times TF(i), \quad (2.2)$$

where  $\Delta l$  is the step size used in the integration and  $N$  is the total number of segments for the discretized AIMD model. As long as the step size is much smaller than the incident field wavelength, the induced voltage can be evaluated accurately. Before the AIMD model can be used together with the the tangential components of the incident fields extracted from the in vivo simulations for device safety evaluation [29], [30], the AIMD model should be placed in a set of pre-defined pathways inside the ASTM or similar phantoms under the RF coil emission for further validation as required in Annex M of [28]. In the validation test, both the direct measurements of the induced voltages and the predicted voltages should be obtained and compared with each other. The predicted voltages should be evaluated using the developed AIMD model together with the tangential components of the incident fields along these pre-defined pathways. Statistical analysis would be used based on these comparisons and the overall measurement and modeling uncertainty is then evaluated. If the differences between the modeling and measurement results are within two-sigma variation, one can use one sigma as the uncertainty of the AIMD model [33]. Under such circumstances, the AIMD model is considered validated [28].

### 2.2.2 Matrix Expression

According to [28], a set of tangential electric field exposures should be used for AIMD model validation. If  $M$  pathways are used in the validation, (2.2) can be expressed in a matrix form as

$$\mathbf{V}_{ind} = \Delta l \mathbf{E}_{tan} \cdot \mathbf{TF} \quad (2.3a)$$

or

$$\begin{bmatrix} V_{ind}^1 \\ V_{ind}^2 \\ \dots \\ V_{ind}^M \end{bmatrix} = \Delta l \begin{bmatrix} E_{tan}^{11} & E_{tan}^{12} & \dots & E_{tan}^{1N} \\ E_{tan}^{21} & E_{tan}^{22} & \dots & E_{tan}^{2N} \\ \dots & \dots & \dots & \dots \\ E_{tan}^{M1} & E_{tan}^{M2} & \dots & E_{tan}^{MN} \end{bmatrix} \begin{bmatrix} TF(1) \\ TF(2) \\ \dots \\ TF(N), \end{bmatrix} \quad (2.3b)$$

where  $[E_{tan}^{i1}, E_{tan}^{i2}, \dots, E_{tan}^{iN}]$  is the  $1 \times N$  tangential component vector of the incident field along the  $i^{th}$  pathway and  $V_{ind}^i$  is the induced voltage when the AIMD is placed along the  $i^{th}$  pathway. For a 40 cm lead electrode,  $N = 40$  if one uses 1 cm as the step size. Often time, the number of the validation pathway  $M$  should be more than 10 to ensure a sufficient validation procedure. Therefore, if 10 pathways were used in the AIMD model validation for a 40 cm long lead electrode, the matrix dimension of  $\mathbf{E}_{tan}$  should be  $10 \times 40$ . To understand the relationship among the tangential components of the incident fields along these pathways, one can perform the singular value decomposition on the tangential components of the incident fields  $\mathbf{E}_{tan}$  as

$$\mathbf{E}_{tan} = \mathbf{U} \mathbf{\Sigma} \mathbf{D} \quad (2.4a)$$

or

$$\begin{bmatrix} E_{tan}^{11} & E_{tan}^{12} & \dots & E_{tan}^{1N} \\ E_{tan}^{21} & E_{tan}^{22} & \dots & E_{tan}^{2N} \\ \dots & \dots & \dots & \dots \\ E_{tan}^{M1} & E_{tan}^{M2} & \dots & E_{tan}^{MN} \end{bmatrix} = [u_1, u_2, \dots, u_M] \sum [d_1, d_2, \dots, d_N]^H, \quad (2.4b)$$

where  $u_i$  is the  $M \times 1$  complex unitary vector,  $d_i$  is the complex  $N \times 1$  unitary vector, and  $\sum = \text{diag}(\sigma_1, \sigma_2, \dots, \sigma_M)$  is an  $M \times N$  rectangular diagonal matrix with non-negative real numbers on the diagonal where  $\sigma_1 \geq \sigma_2 \geq \dots \geq \sigma_M \geq 0$ . The relative value of  $\sigma$  represents the energy level for each eigenvector. Based on this decomposition, the tangential components of the incident fields along  $M$  pathways can also be considered as the superposition of the eigenvectors  $[d_1, d_2, \dots, d_N]$ . Combining (2.3b) and (2.4b), we have

$$\begin{bmatrix} V_{ind}^1 \\ V_{ind}^2 \\ \dots \\ V_{ind}^M \end{bmatrix} = \Delta l [u_1, u_2, \dots, u_M] \sum [d_1, d_2, \dots, d_N]^H \begin{bmatrix} TF(1) \\ TF(2) \\ \dots \\ TF(N) \end{bmatrix}. \quad (2.5)$$

If the tangential components of the incident fields along each pathway are not totally orthogonal to each other,  $\sigma_i$  would have a different value. In addition, if the first  $k$  eigenvalues are much larger than the last few ones, the first few eigenvectors would contribute more to the tangential electric field distributions for all pathways. In other words, the electric field distribution along these  $M$  pathways can be approximately determined by the first  $k$  eigenvectors. Consequently, the projection of the AIMD model on these eigenvectors contributes more to the induced voltage while its projection on other eigenvectors would only have minimal effect on the RF-induced voltage.

Based on this, if a subset of  $k$  dominant eigenvectors were found, only  $k$  validations are meaningful since the tangential electric field distributions are a simple superposition of these  $k$  eigenvectors [34]. In order to have  $M$  sets of meaningful validation, one should select pathways along which the field distributions are orthogonal to each other. Under such circumstance,  $\sigma_i$  would have similar values and all  $M$  eigenvectors are meaningfully represented in the pathways.

### 2.2.3 Spurious AIMD Models

In the previous section, for those  $M$  pathways with  $k$  dominant eigenvectors, only  $k$  validation measurements are meaningful or non-redundant. In this section, we show that false validations can occur if we use these pathways for AIMD model validation.

We can generate a spurious AIMD model  $\mathbf{TF}_2$  by adding any eigenvector from  $[d_{k+1}, d_{k+2}, \dots, d_N]^H$  to an original AIMD model  $\mathbf{TF}_1$ . This spurious AIMD model  $\mathbf{TF}_2$  can also generate similar induced voltage values as those from  $\mathbf{TF}_1$  along these  $M$  pathways.

The spurious AIMD model can be generated by

$$\mathbf{TF}_2 = \mathbf{TF}_1 + d_i \quad (k < i \leq M, \sigma_k \gg \sigma_i), \quad (2.6)$$

where  $d_i$  is the eigenvector in the space whose eigenvalue meets the condition  $\sigma_k \gg \sigma_i$ .

The induced voltages along these pathways by two AIMD models can be evaluated via

$$\begin{bmatrix} V_{ind}^1 \\ V_{ind}^2 \\ \dots \\ V_{ind}^M \end{bmatrix} = \Delta l [u_1, u_2, \dots, u_M] \sum [d_1, d_2, \dots, d_N]^H \begin{bmatrix} TF_1(1) \\ TF_1(2) \\ \dots \\ TF_1(N) \end{bmatrix} \quad (2.7a)$$

and

$$\begin{bmatrix} V_{ind}^1 \\ V_{ind}^2 \\ \dots \\ V_{ind}^M \end{bmatrix} = \Delta l [u_1, u_2, \dots, u_M] \sum [d_1, d_2, \dots, d_N]^H \begin{bmatrix} TF_2(1) \\ TF_2(2) \\ \dots \\ TF_2(N) \end{bmatrix}. \quad (2.7b)$$

The relative difference between two sets of induced voltage is

$$\frac{\|\mathbf{V}' - \mathbf{V}\|}{\|\mathbf{V}\|} = \frac{\Delta l \sigma_i}{\|\mathbf{V}\|} \leq \frac{\sigma_i}{\|\mathbf{E}_{tan} \mathbf{TF}_1\|} \leq \frac{\sigma_i}{\sigma_k} \frac{\|d_i\|}{\|\mathbf{TF}_1\|}. \quad (2.8)$$

Hence two different AIMD models would predict nearly the same induced voltages along these pathways as long as  $\sigma_i$  is much smaller than  $\sigma_k$ . This can also be explained as the  $d_i$  ( $k < i < M$ ) are orthogonal to the first  $k$  eigenvectors, the projection/inner product of different transfer functions onto the first domain  $k$  modes will lead to induced voltages bounded by the ratio of  $\sigma_i/\sigma_k$ .

### 2.3 Validation with ISO 10974 Pathways

In this section, we used the standard pathways defined in [28] to demonstrate the theory developed earlier. As shown in the following, validations using these pathways are 1) not efficient or redundant, and 2) also incomplete since two significantly different AIMD models can be validated using these pathways.

### 2.3.1 Standard Pathways for AIMD Model Validation

Eleven pathways from ISO 10974 were selected in our numerical study. The illustration of these pathways in the ASTM phantom, oval phantom, and circular phantom are given in Fig. 2.1 [28].

The ASTM phantom has a length of 650 mm, a width of 420 mm, and was filled with gelled saline for 90 mm in depth. The oval phantom has a short-axis of 400 mm, a long-axis of 600 mm, and was filled with the gelled saline of 90 mm in depth. The diameter of the circular phantom is 220 mm and it is also filled with a gel of 90 mm in depth. According to the standard ASTM F2182-11a [27], the gelled saline should have a relative permittivity of 80.38 and a conductivity of 0.47 S/m to mimic the human tissue for 1.5T system testing. The RF coil used here is a birdcage coil that has a diameter of 630 mm and a height of 650 mm as shown in Fig. 2.2. The RF coil consists of eight rungs and each rung is excited by a current source. The blue lines at the end rings are the turning capacitors. These capacitors were tuned to make the entire system resonate at 64 MHz, which corresponded to the operating frequency of a 1.5T MRI system. All simulations were performed using the standard electromagnetic computer-aided design (SEMCAD) package. Under the emission of the RF coil, the electric field distributions along these pathways were evaluated for different excitations. A summary of the excitation and phantom type for these pathways is given in Table 1. Detailed placement of the phantoms inside the RF coils can be found in [28].

The extracted incident field distributions along all pathways are shown in Fig. 2.3. It appears that some of the electric field distributions are similar to each other, indicating potential correlation among them. With an electrode length of 40 cm, the incident electric field matrix has a dimension of  $11 \times 40$ . Singular value decomposition

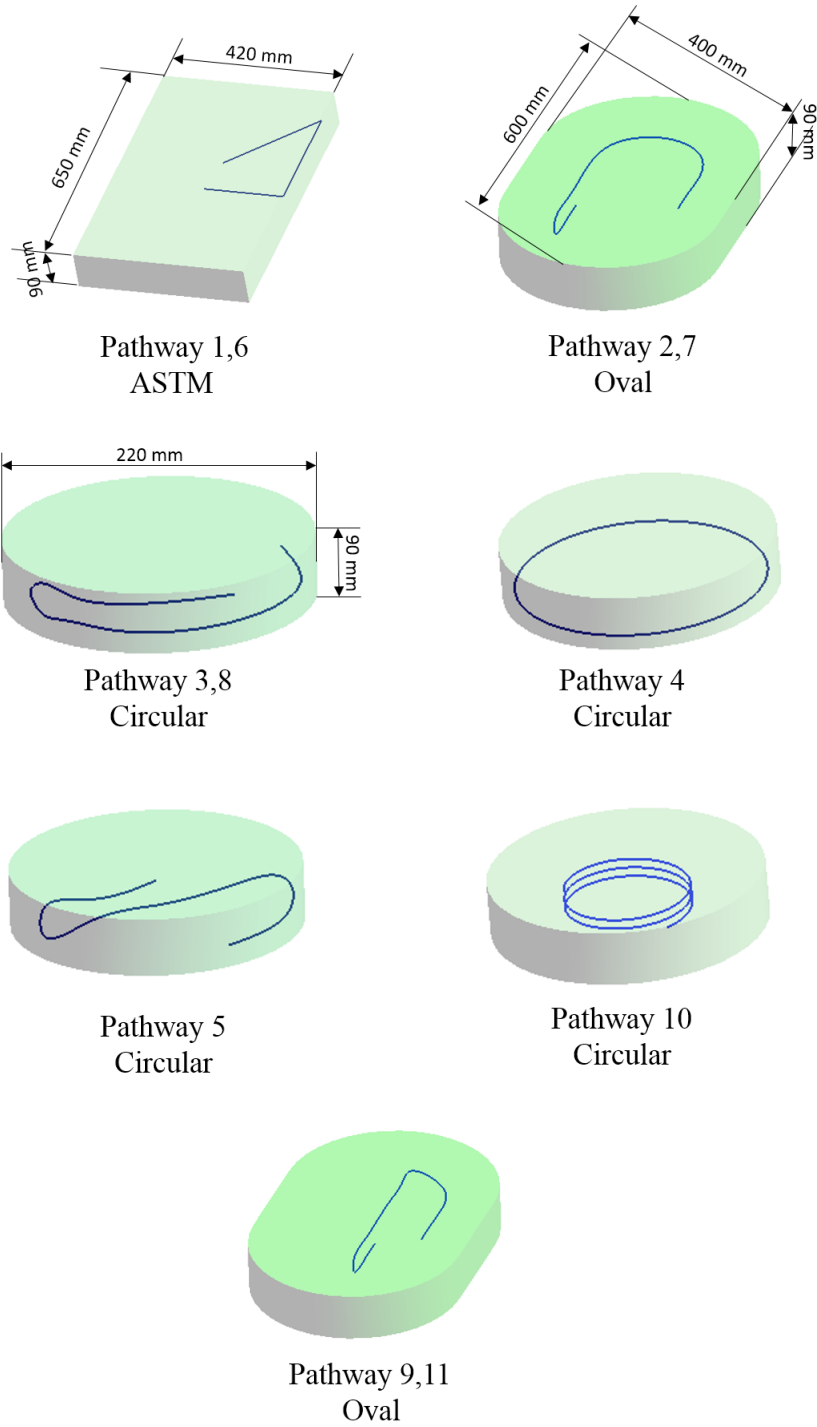


Fig. 2.1: The ISO 10974 standard advised pathways (pathway 1-5 and 11 are in the linear polarization coil; pathway 6-8 and 10-11 are in the quadrature polarization coil).

Table 1: Excitation and Phantom Type of Pathways.

Pathway index	RF coil excitation	Phantom type
1	Linear	ASTM
2	Linear	Oval
3	Linear	Circular
4	Linear	Circular
5	Linear	Circular
6	Quadrature	Circular
7	Quadrature	Oval
8	Quadrature	Circular
9	Linear	Oval
10	Quadrature	Circular
11	Quadrature	Oval

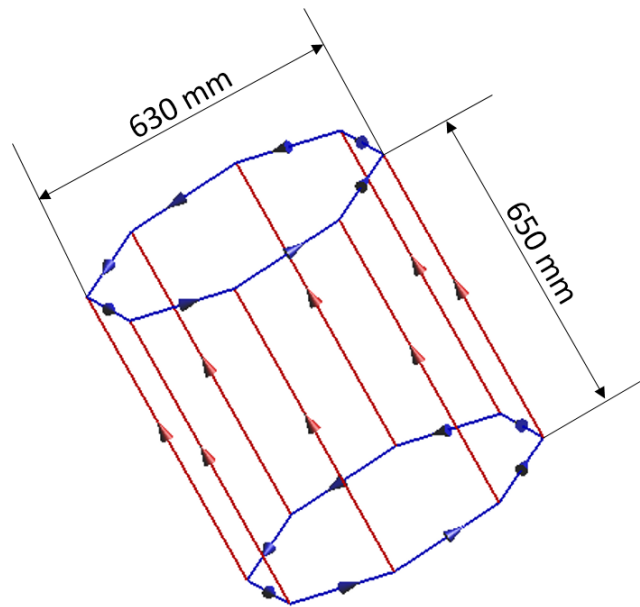


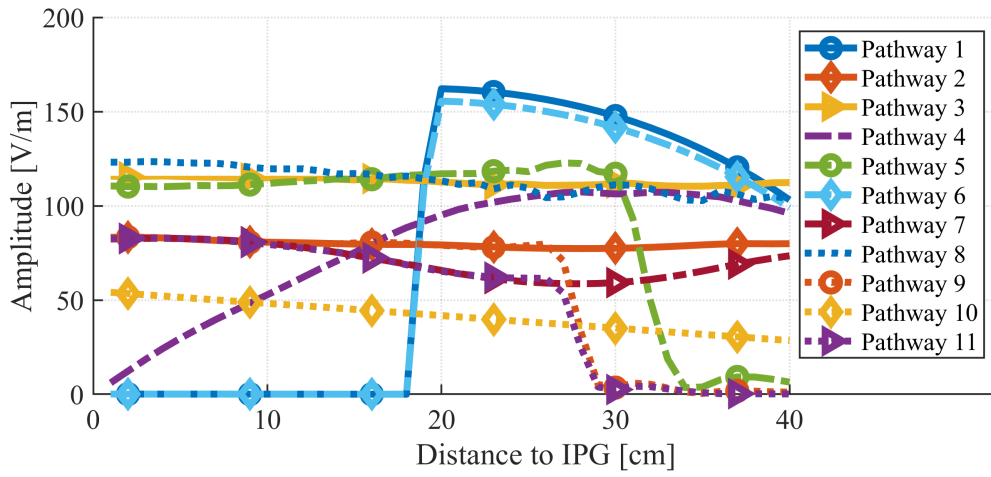
Fig. 2.2: The generic birdcage coil.

was performed on this incident electric field matrix. The eigenvalues for all 11 eigenvectors were plotted in Fig. 4. As clearly indicated in the figure, starting with the sixth eigenvalue, these values become much smaller than previous ones. This means that the tangential electric field distributions along these 11 pathways are mainly composed of the first five eigenvectors. Therefore, only five validations are meaningful. Other validations would be a simple repetition of the incident field superposition. This confirmed our first observation that these pathways cannot provide meaningful validations for all 11 pathways. Only five of them can be considered as meaningful and not redundant.

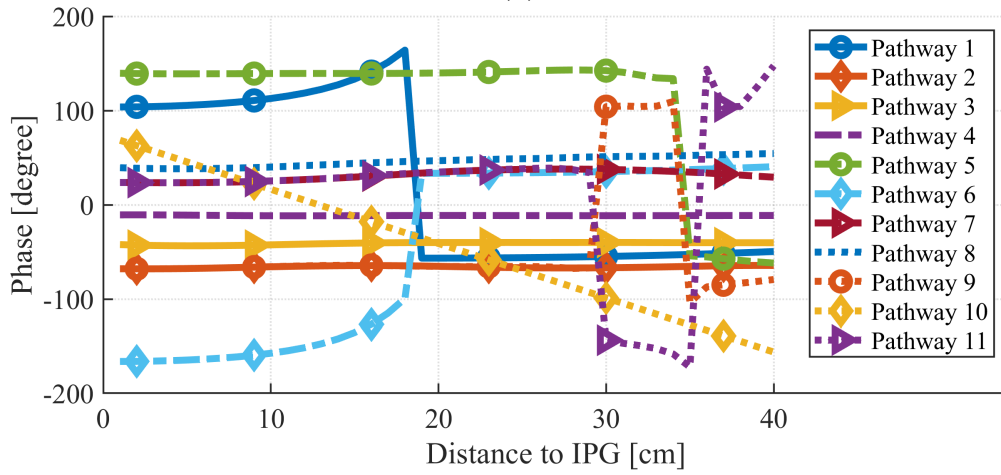
To demonstrate that these pathways can also lead to false validation, we generated two significantly different AIMD models. The first AIMD model ( $\mathbf{TF}_1$ ) was numerically developed for a 40 cm solid lead using the reciprocity method [25]. The discretized step size of the AIMD model was set to 1 cm. The second spurious AIMD model ( $\mathbf{TF}_2$ ) was generated by adding the sixth eigenvector from the incident field matrix to the first AIMD model. As shown in Fig. 5, these two models are quite different.

With pathways defined in ISO 10974, the induced voltages estimated from these two different AIMD models were shown in Fig. 2.6. As clearly indicated in the Fig. 2.6, these two different AIMD models can generate almost identical induced voltages. This further demonstrated that the current ISO 10974 suggested pathways cannot be used to provide validation for a unique AIMD model or the validation is incomplete.

Practical AIMD models often have slow magnitude variation along the electrodes due to the long wavelength at 64 MHz [24], [25]. We also developed a smoothed spurious AIMD model  $\mathbf{TF}_3$  by filtering out those unrealistic high-frequency variations as shown in [35]. Comparisons of  $\mathbf{TF}_1$  and  $\mathbf{TF}_3$  are given in Fig. 7. Using these two

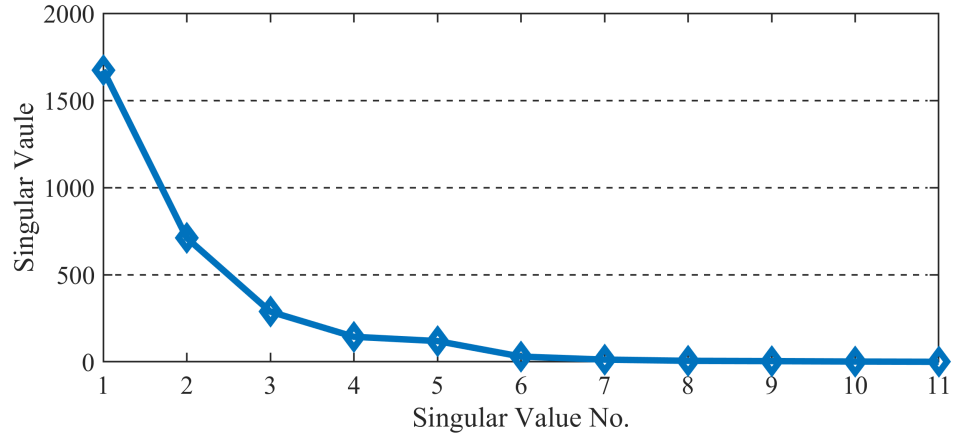


(a)

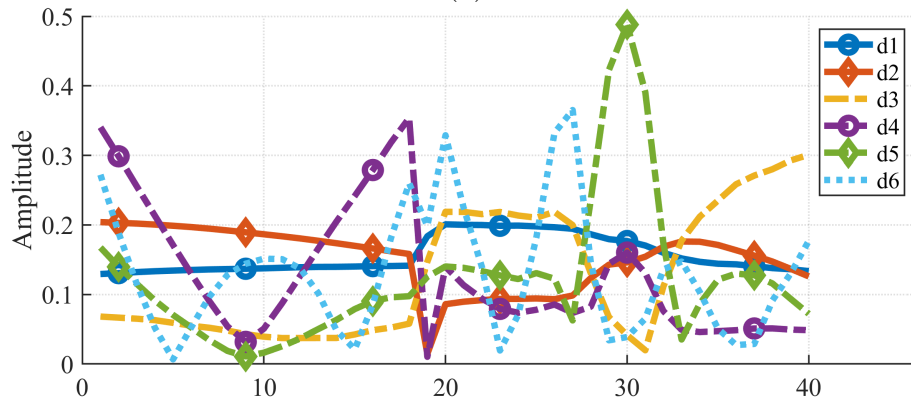


(b)

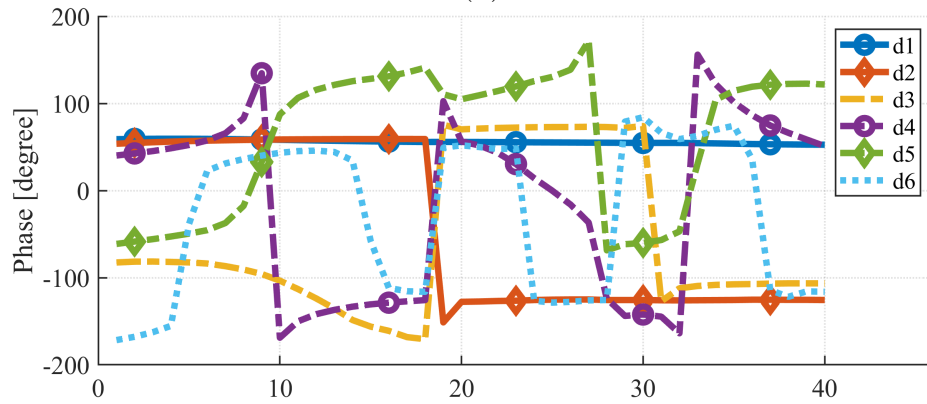
Fig. 2.3: (a) Magnitude of the tangential electric field along the standard pathways; (b) Phase of the tangential electric field along the standard pathways.



(a)

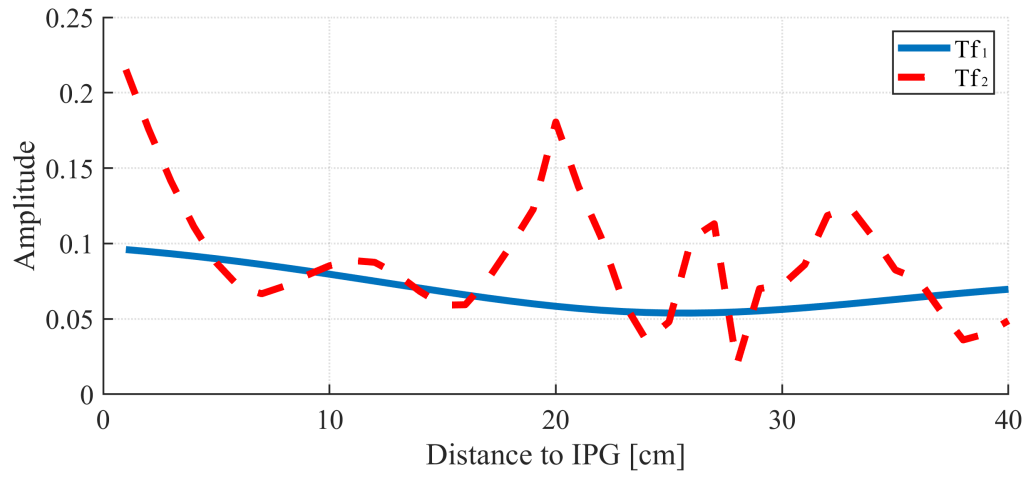


(b)

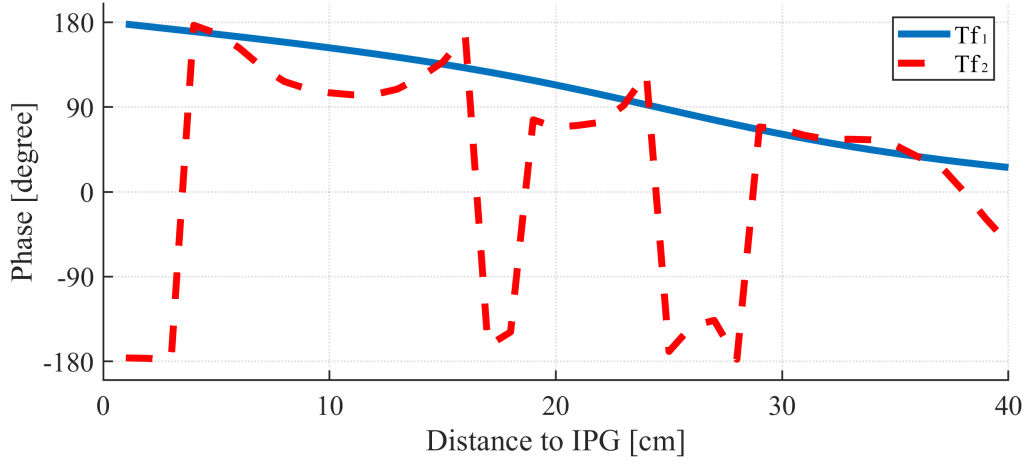


(c)

Fig. 2.4: (a) Singular values of the tangential electric field matrix; (b) Magnitude of first six tangential electric field matrix eigenvectors; (c) Phase of first six tangential electric field matrix eigenvectors.

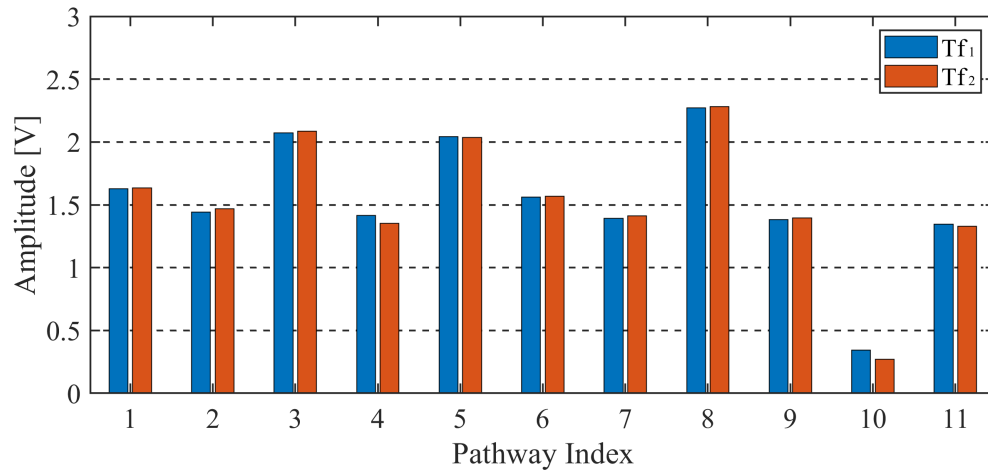


(a)

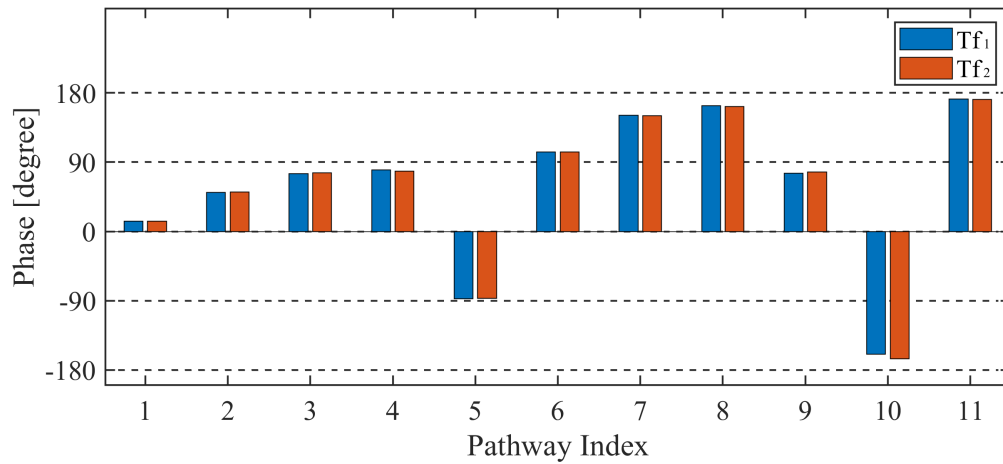


(b)

Fig. 2.5: (a) Magnitude of  $\mathbf{TF}_1$  and  $\mathbf{TF}_2$ ; (b) Phase of  $\mathbf{TF}_1$  and  $\mathbf{TF}_2$ .



(a)



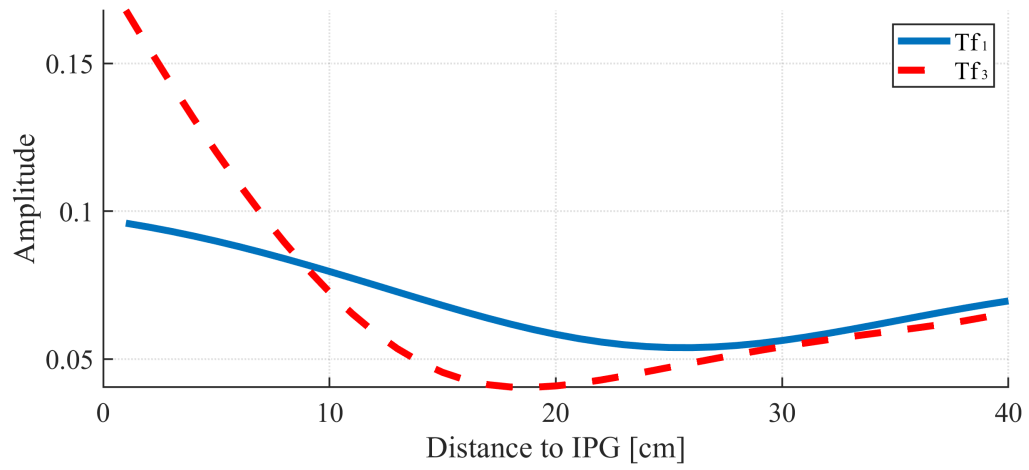
(b)

Fig. 2.6: (a) Amplitude of induced voltages for  $\mathbf{TF}_1$  and  $\mathbf{TF}_2$  along the standard validation pathways; (b) Phase of induced voltages for  $\mathbf{TF}_1$  and  $\mathbf{TF}_2$  along the standard validation pathways.

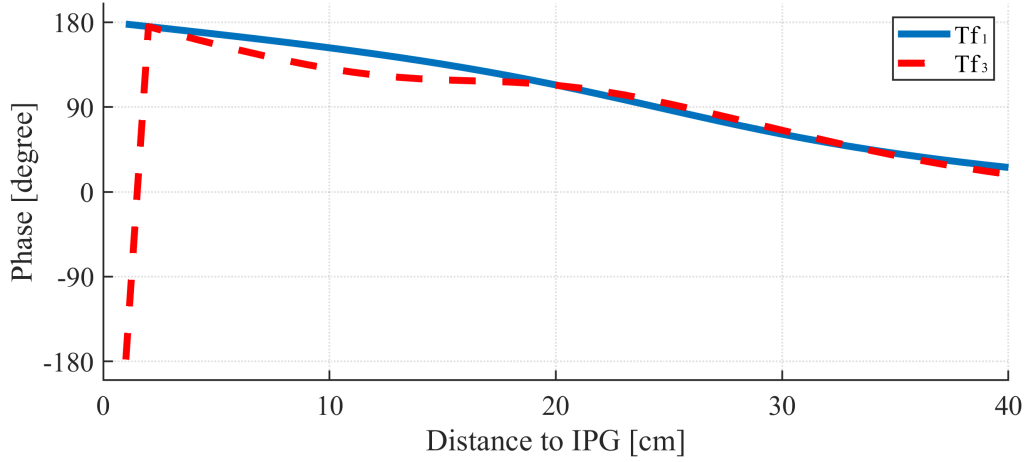
models, a comparison of the induced voltages is given in Fig. 8. Again, these values are very close to each other. This demonstrated our second point: ISO 10974 could validate two AIMD models with a significant difference as long as the difference was represented by those eigenvectors with smaller eigenvalues from the incident matrix. Therefore, the model validation is incomplete. However, we should point out that the pitfall here is only related to the selected pathways for validation. It is not related to errors of the transfer function method itself. It is shown in the later section that if appropriate pathways are selected, such a pitfall can be avoided.

## 2.4 Appropriate Pathways for Validation

As shown in the previous section, the standard pathways defined in ISO 10974 cannot provide meaningful AIMD model validation. Based on the theory described in Section II, two sets pathways are proposed here. Ideally, these pathways should have tangential electric fields orthogonal to each other. To develop pathways with orthogonal electric field distributions among them, we used the concept from the Hadamard matrix [32]. The convenience of the Hadamard matrix is that its entries are 1 or -1, which behaves like a forward or backward direction of a pathway for our practical application. For practical purposes, the Hadamard matrix of order eight was used and is shown in (2.9). Based on this matrix and also the knowing the electric field distribution inside the ASTM phantom, the proposed V-shaped pathways are given in Fig. 2.9. This kind of a folding pathway was observed in clinical settings [36]. The forward and backward folding along the pathways is shown as positive and negative values in (2.9). For each folding corner, the distance is 1 cm away from the previous folding corner. Each segment is 5 cm so that the overall length is at 40 cm. For each pathway, its center along the vertical direction was at the phantom center.

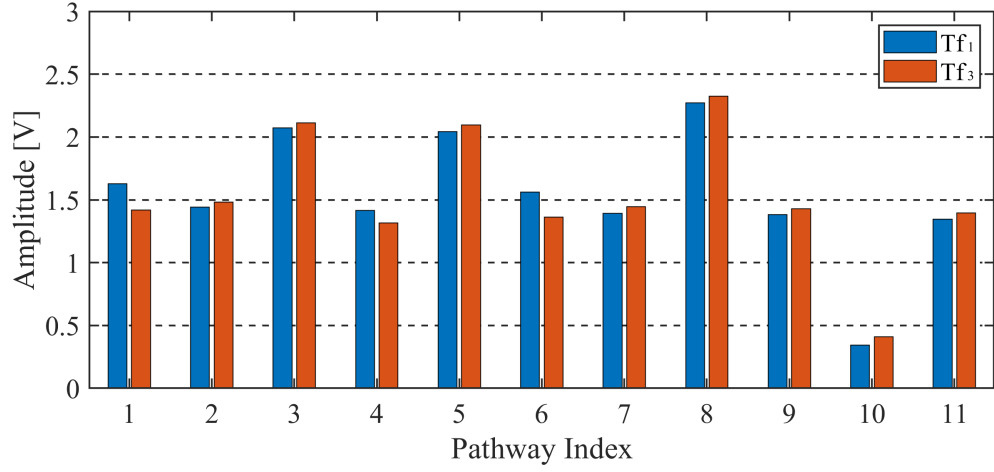


(a)

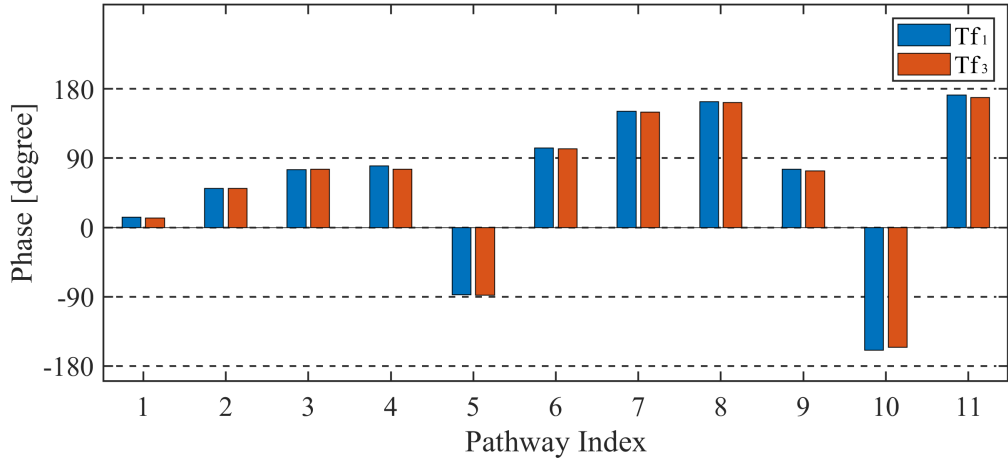


(b)

Fig. 2.7: (a) Magnitude of  $\mathbf{TF}_1$  and  $\mathbf{TF}_3$ ; (b) Phase of  $\mathbf{TF}_1$  and  $\mathbf{TF}_3$ .



(a)



(b)

Fig. 2.8: (a) Amplitude of induced voltages for  $\mathbf{TF}_1$  and  $\mathbf{TF}_3$  along the standard validation pathways; (b) Phase of induced voltages for  $\mathbf{TF}_1$  and  $\mathbf{TF}_3$  along the standard validation pathways.

Its left side was 2 cm away from the border of the phantom. These pathways were all 4.5 cm under the gel surface.

$$H_8 = \begin{bmatrix} 1 & 1 & 1 & 1 & 1 & 1 & 1 & 1 \\ 1 & -1 & 1 & -1 & 1 & -1 & 1 & -1 \\ 1 & 1 & -1 & -1 & 1 & 1 & -1 & -1 \\ 1 & -1 & -1 & 1 & 1 & -1 & -1 & 1 \\ 1 & 1 & 1 & 1 & -1 & -1 & -1 & -1 \\ 1 & -1 & 1 & -1 & -1 & 1 & -1 & 1 \\ 1 & 1 & -1 & -1 & -1 & -1 & 1 & 1 \\ 1 & -1 & -1 & 1 & -1 & 1 & 1 & -1 \end{bmatrix} \quad (2.9)$$

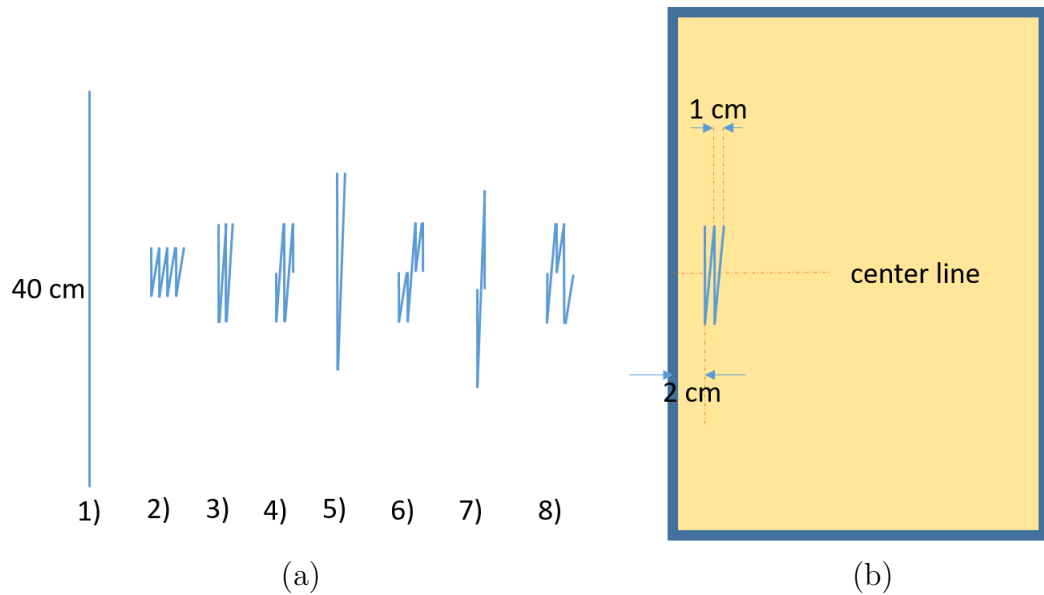
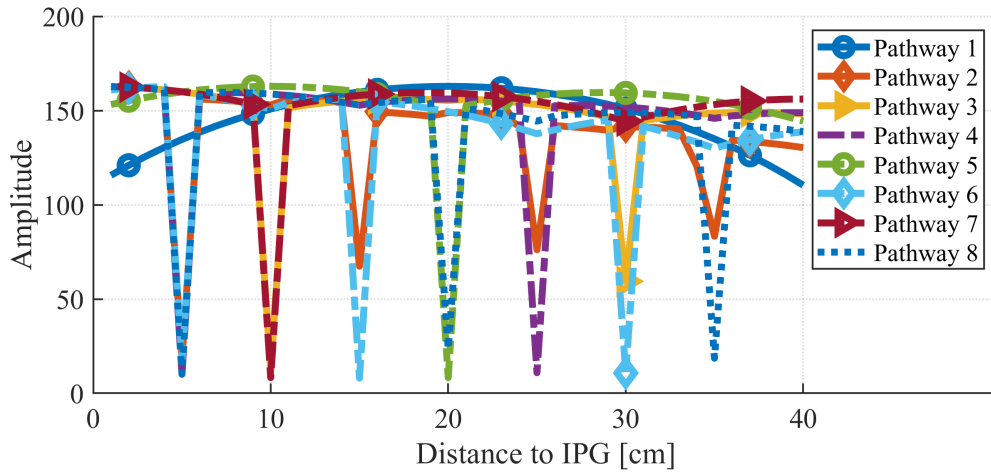


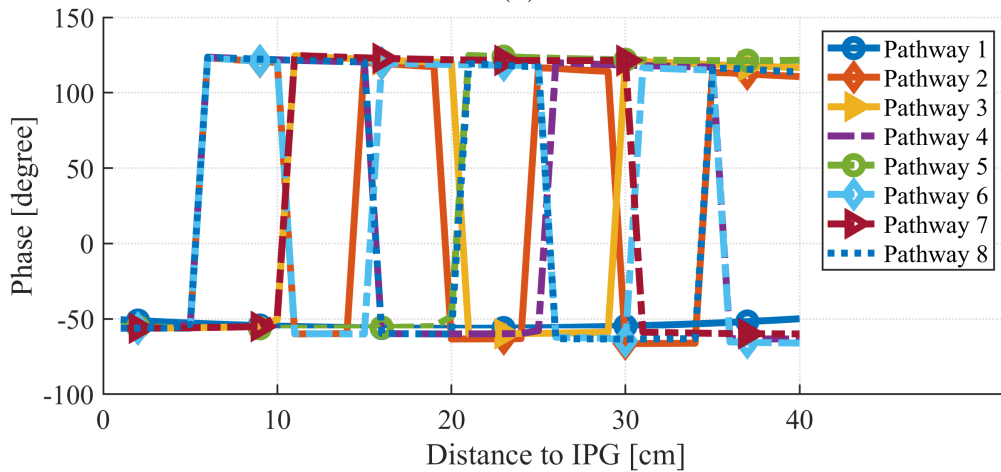
Fig. 2.9: (a) Illustration of V-shaped pathways based on (2.9); (b) Illustration of the pathway position relative to the ASTM phantom.

The magnitude and phase of the electric field along the V-shaped pathways are shown in Fig. 2.10. The magnitude changed at the folding point along the pathways,

and the phase switched after each turn. Singular value decomposition was also performed on the tangential electric field matrix of the V-shaped pathways. The singular values are shown in Fig. 2.11. As one can see from the figure, all eigenvalues were similar to each other, indicating each validation pathway can be treated as mutually independent.

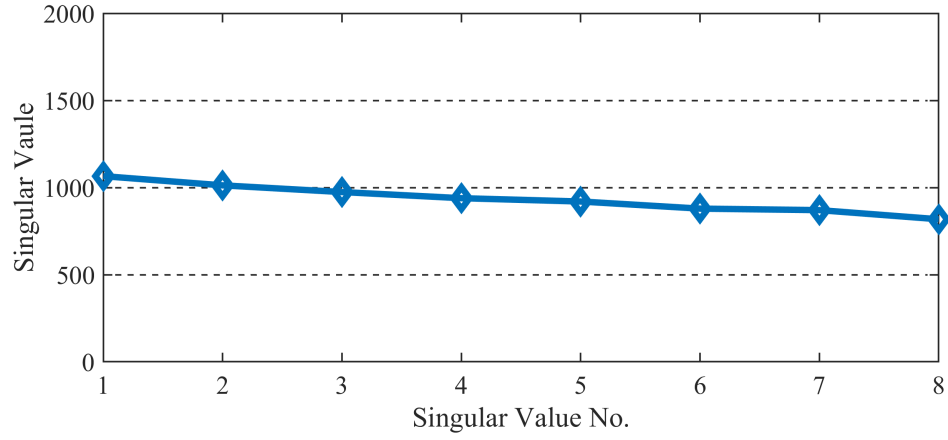


(a)

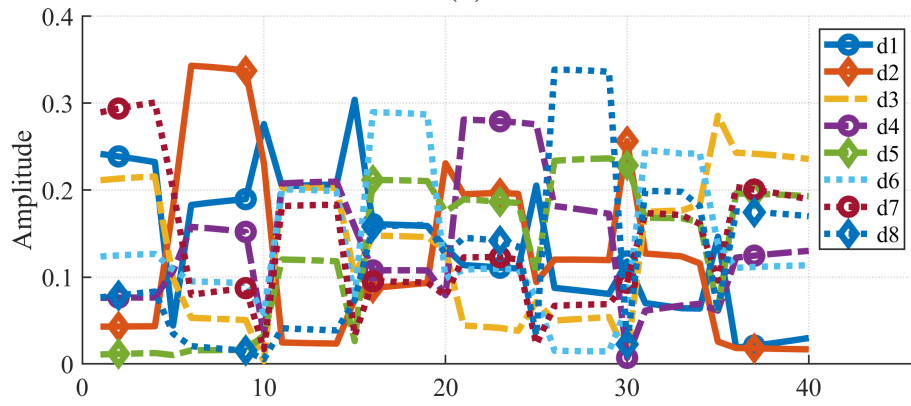


(b)

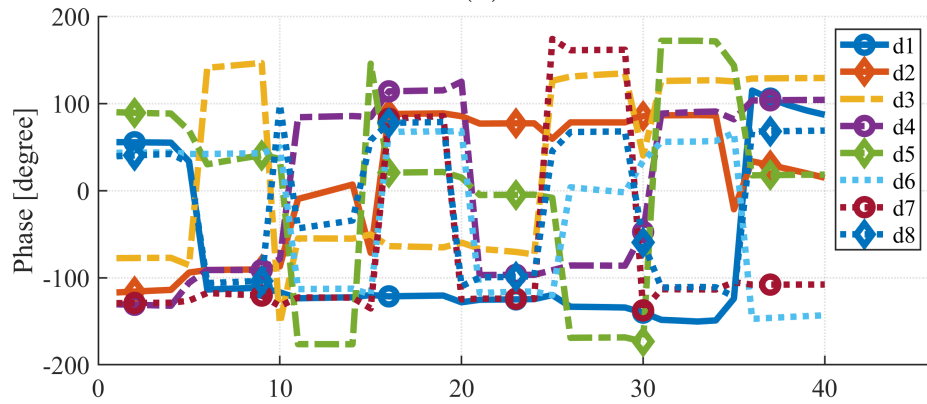
Fig. 2.10: (a) Magnitude of the tangential components of the incident field along the V-shaped orthogonal pathways; (b) Phase of the tangential components of the incident field along the V-shaped orthogonal pathways.



(a)



(b)



(c)

Fig. 2.11: (a) Singular values of the V-shaped tangential electric field matrix; (b) Magnitude of the V-shaped tangential electric field matrix eigenvectors; (c) Phase of the V-shaped tangential electric field matrix eigenvectors.

The induced voltages  $\mathbf{TF}_1$ ,  $\mathbf{TF}_2$  and  $\mathbf{TF}_3$  were calculated as shown in Fig. 2.12. As clearly shown in the figure, the validation of the AIMD models along these pathways showed significant differences in the induced voltages.

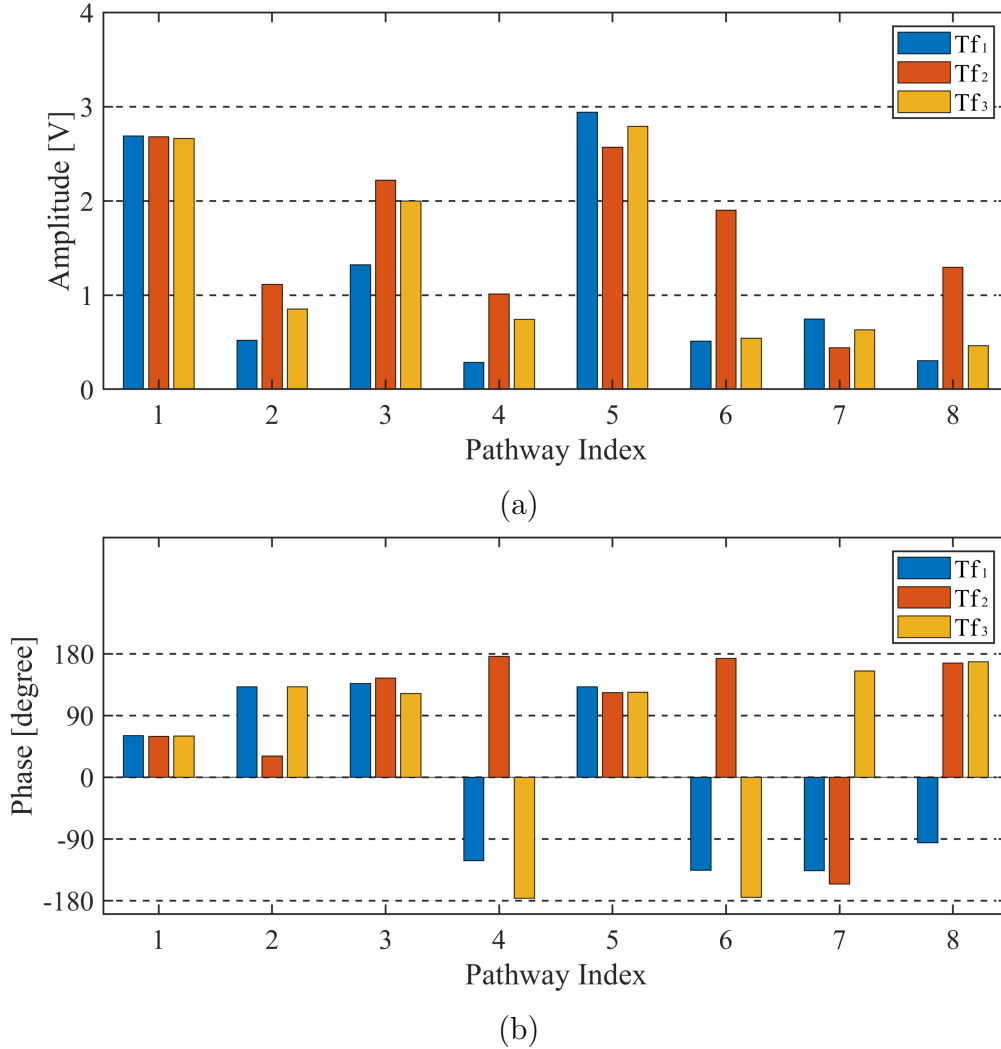


Fig. 2.12: (a) Amplitude of induced voltages  $\mathbf{TF}_1$ ,  $\mathbf{TF}_2$  and  $\mathbf{TF}_3$  along the V-shaped orthogonal validation pathways; (b) Phase of induced voltages  $\mathbf{TF}_1$ ,  $\mathbf{TF}_2$  and  $\mathbf{TF}_3$  along the V-shaped orthogonal validation pathways.

The only pathway that led to similar RF-induced voltages was pathway 1, which has a uniform electric field distribution along the pathway, similar to those defined in ISO

10974. Therefore, these pathways not only provided eight meaningful validations, but they also showed significant differences in induced voltages due to differences in the AIMD models.

In practice, it may not be feasible to bend the leads along the V-shaped pathways. An alternative pathway set as shown in Fig. 2.13 was proposed.

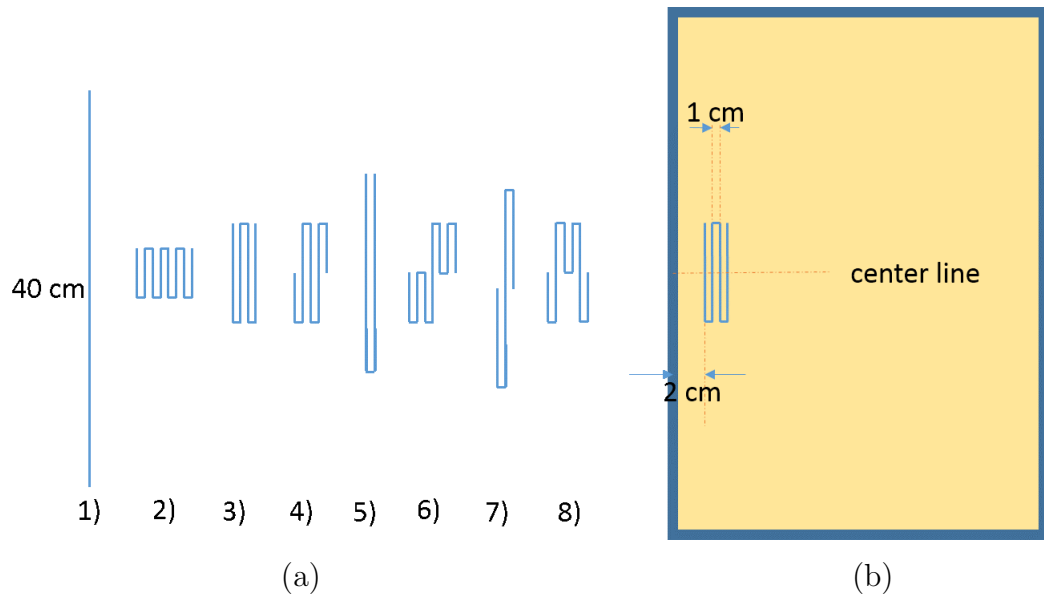
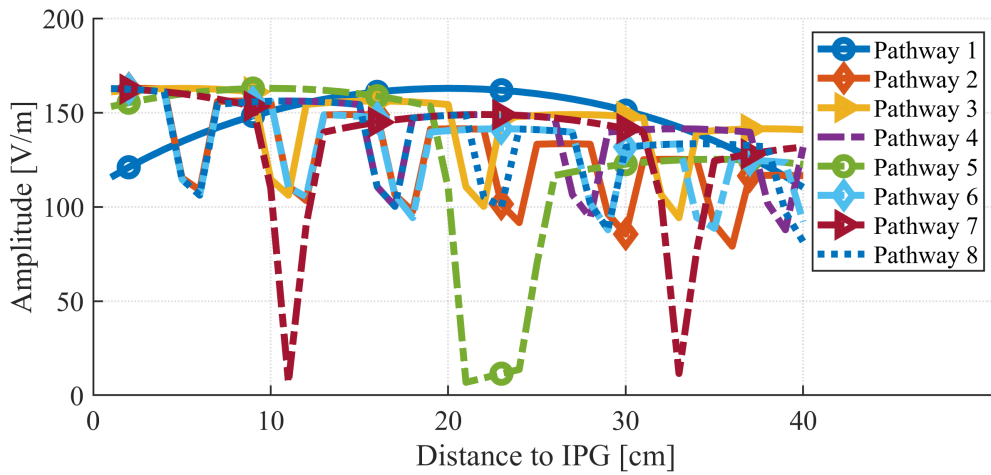


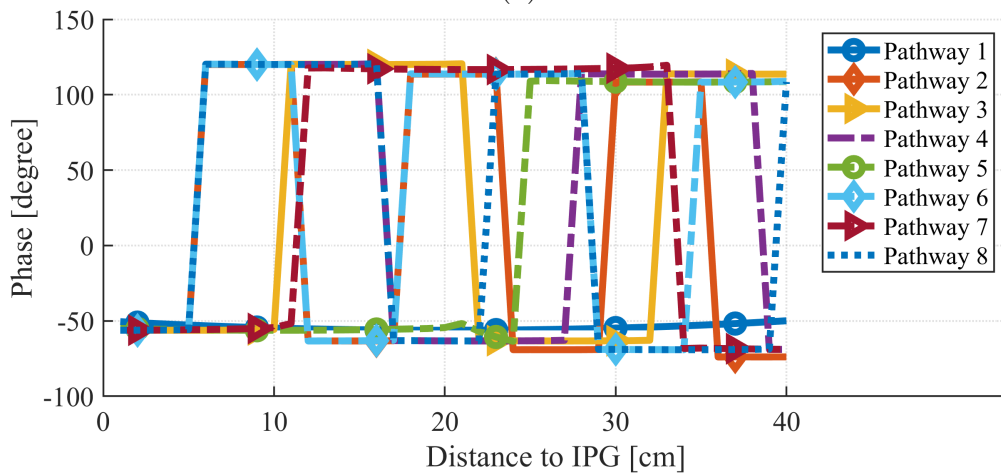
Fig. 2.13: (a) Illustration of U-shaped pathways based on (2.9); (b) Illustration of the pathway position relative to the ASTM phantom.

For each turning point, an additional 1 cm distance was used to ease the folding of the electrodes. Electromagnetic simulations were then performed to extract incident electric field distributions along these pathways. The tangential electric field along the U-shaped pathways is shown in Fig. 2.14.

Singular value decomposition of the tangential electric field matrix along the U-shaped pathways was performed, and the results are shown in Fig. 2.15. The smallest singular value was still about one-third of the largest singular value. This indicated the electric field distributions along these pathways were still quite orthogonal to each



(a)



(b)

Fig. 2.14: (a) Magnitude of the tangential components of the incident field along the U-shaped orthogonal pathways; (b) Phase of the tangential components of the incident field along the U-shaped orthogonal pathways.

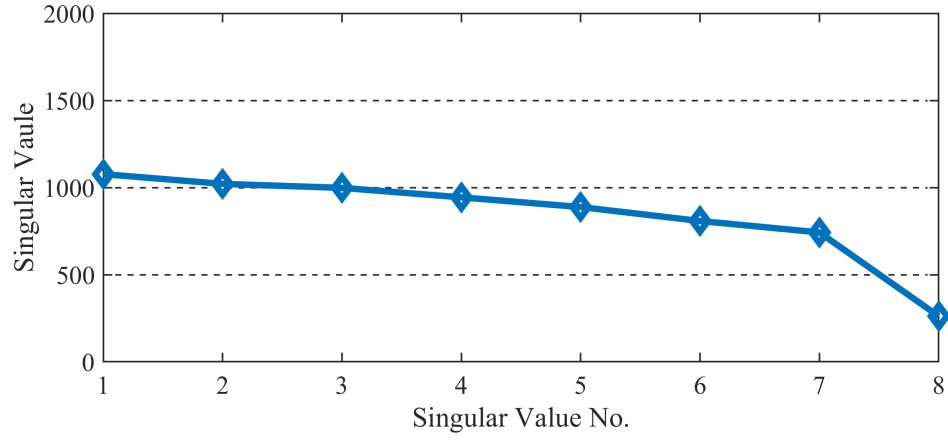
other. Therefore, these can also be used as a meaningful validation set.

The induced voltages of three AIMD models were calculated and the results are shown in Fig. 2.16. Induced voltages generated by three AIMD models showed significant differences. This confirmed that these U-shaped pathways can also provide eight meaningful validations and also captured the differences among different AIMD models.

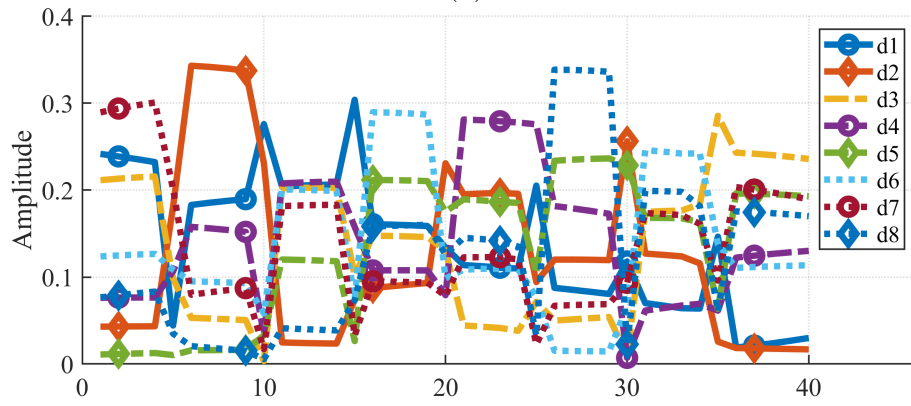
## 2.5 Discussion

The AIMD model validation is a critical part of the safety assessment of AIMD under harsh MRI RF coil emissions. A theory based on eigen-analysis was presented on how to evaluate appropriate pathways. It indicated that one would need to select pathways that have independent incident electric field distributions among them. Without independent incident field distributions among these pathways, only a subset of the validation is meaningful. In addition, inappropriate pathway sets could also erroneously validate two different AIMD models, leading to incomplete validation.

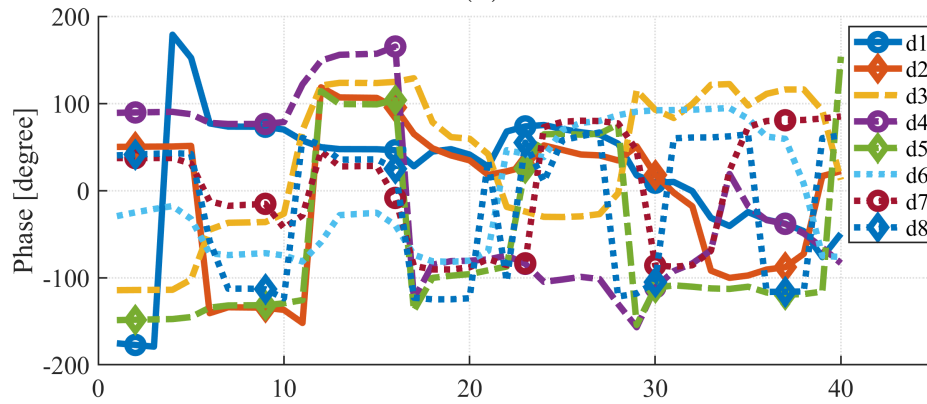
Current AIMD models were developed based on either forward or reciprocity measurements that needed to be performed at 1 cm or less spatial resolution. For a 40 cm long electrode, the AIMD model would be represented by at least 40 discretized values. This is similar to the use of a sub-domain basis function in the method of moments to represent the solution space [37]. All 40 discretized values are needed to represent the AIMD model. Under this circumstance, a total of 40 validations should be performed for the AIMD model. Otherwise, the validation process can only be considered as partial validation or incomplete model validation. But complete validation for AIMD models based on the current method is not feasible considering the number of pathways to be used.



(a)

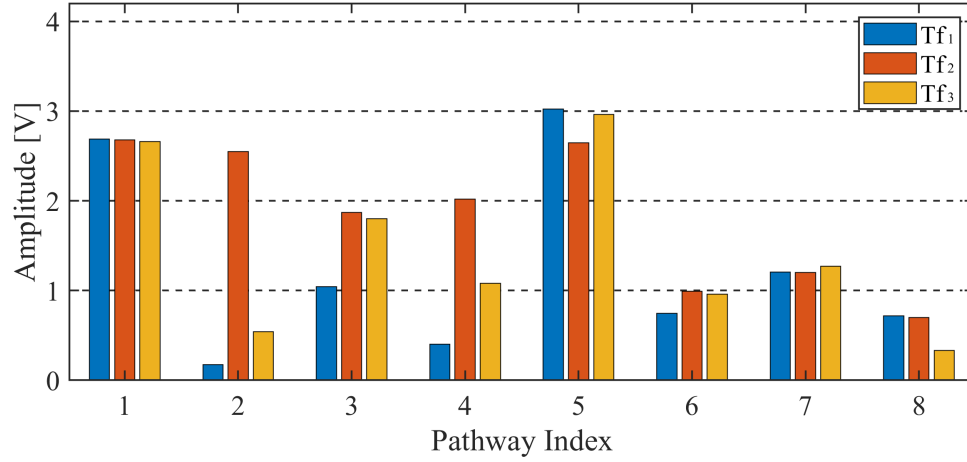


(b)

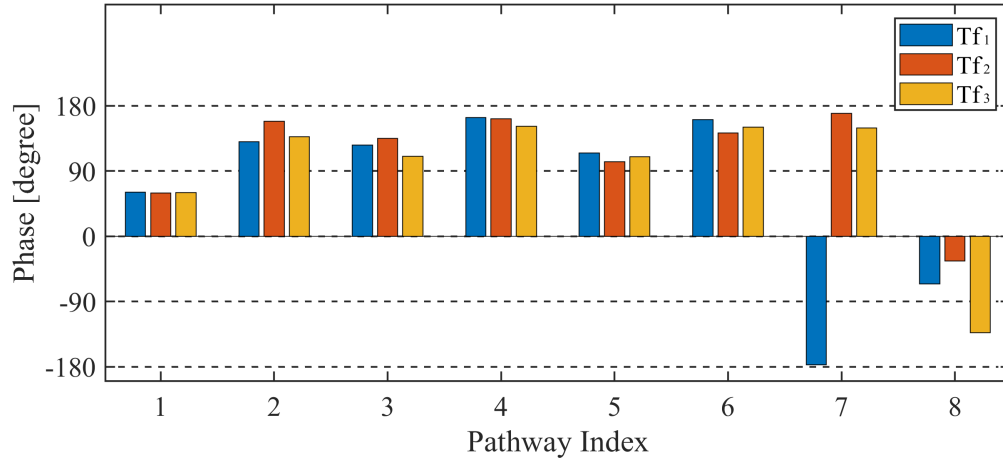


(c)

Fig. 2.15: (a) Singular values of the U-shaped tangential electric field matrix; (b) Magnitude of the U-shaped tangential electric field matrix eigenvectors; (c) Phase of the U-shaped tangential electric field matrix eigenvectors.



(a)



(b)

Fig. 2.16: (a) Amplitude of induced voltages  $\mathbf{TF}_1$ ,  $\mathbf{TF}_2$  and  $\mathbf{TF}_3$  along the U-shaped orthogonal validation pathways; (b) Phase of induced voltages  $\mathbf{TF}_1$ ,  $\mathbf{TF}_2$  and  $\mathbf{TF}_3$  along the U-shaped orthogonal validation pathways.

An alternative approach for the AIMD model validation is to use the transmission line model described in [38]. Using the transmission line model for the AIMD device, only requires one to use four complex parameters: the tip impedance, the IPG impedance, the characteristic impedance of the lead body, and the wavenumber of the lead body. Since the validation of RF-induced heating can only measure the temperature rise as a scalar number, it would now require eight meaningful validations. The proposed two sets of validation pathways can clearly meet this requirement and one can now fully validate the transmission line based AIMD model with these pathways. This would provide meaningful and accurate validation for all AIMD models. The uncertainty of the numerical study is 9.86%. It includes the leads path uncertainty and material property uncertainty. By shifting the lead path 1 cm and electrical property 10%, the electric field was compared to the original one.

# 3 Developing AIMD Models Using Orthogonal Pathways from MRI Safety Assessment

## 3.1 Introduction

As mentioned in previous section, the transfer function (TF) method was commonly used for such safety evaluations [24], [25]. In this approach, the AIMD models are a series of piece-wise values that relate the incident electromagnetic fields along the lead to the RF-induced voltage or heating. One can obtain the AIMD models through measurement and then combine them with electromagnetic simulations to estimate the safety hazards for both temperature rise at the electrode and induced voltage inside the IPG. For a 40 cm long lead, it would be represented by 40 piece-wise values along the lead if a resolution of 1 cm is adopted. In this conventional approach of AIMD model development, the first step is to measure the relative magnitude and phase of the AIMD model using the forward or reciprocity method [24], [25]. In the second step, additional ASTM phantom measurement is required to determine the appropriate model coefficient while the device is under the RF emission system [28]. Although the AIMD model could be obtained through direct measurement, there are some disadvantages which limit its application: 1) special extra measurement systems are needed to directly measure the AIMD using either forward or reciprocity method and 2) it is difficult, if not impossible, to measure the AIMD model while not affect the RF behaviors of the AIMD, since the AIMD and the measurement system are coupled due to the tight RF interactions [39]. An alternative way to represent the AIMD model is to use the transmission line concept [38]. In this approach, the AIMD model can be constructed using 4 complex parameters: IPG impedance, tip (electrode) impedance, lead body wavenumber and lead body characteristic impedance in the

test medium. Within this in mind, if one can accurately extract these four complex parameters, the AIMD model can be developed. Therefore, instead of using a series of piece-wise values along the lead body for model development, a semi-analytical model can be generated.

To determine the four parameters described above, at least four experimental measurements need to be performed. In the measurements, the device should be placed along different pathways inside the ASTM phantom and the induced heating or induced voltages are then recorded. Based on the directly measured data as well as the semi-analytical AIMD model, optimization algorithms can be used to estimate these parameters based on the measurements. Using this proposed approach, rather than requiring specific equipment for the relative magnitude and phase measurement, the AIMD model development can be performed in the standard ASTM phantom.

To ensure a good AIMD model development, the incident field distributions along the test pathways need to be independent of each other since the correlated incident field can make the problem to be ill-conditioned. To address this requirement, a set of pathways based on the Hadamard matrix is used in the study [32], [40]. Besides, if one can normalize all impedance, the AIMD models can be developed with three parameters. Based on the measured data, the particle swarm optimization method (PSO) is used for parameter estimation. As the semi-analytical model is developed based on induced heating or voltage only, the uncertainty involved by the equipment measuring the AIMD model shape is eliminated.

The remainder of this chapter is organized as follows. In Section 2, the theory of choosing appropriate pathways for AIMD model development is presented. In Section 3, using the theory described in Section 2, two sets of experiments are used to develop the AIMD models. Based on the results of our studies, the conclusions are given in

Section 4.

## 3.2 Methodology

In this section, we present the methods for the AIMD model development. For simplicity, we use the voltage AIMD model development for illustration but the procedure is also applicable to the heating AIMD model development.

### 3.2.1 Voltage AIMD Model Development

A voltage AIMD model relates the incident electric field along the lead body to the induced voltage at the device IPG end. As shown in [24], [25], the induced voltage in the IPG can be evaluated by the integration of the incident electric fields along the device pathways with the AIMD model along the lead as

$$\begin{aligned} V_{ind} &= \int_L \vec{E}_{inc} \cdot TF d\hat{l} \\ &= \int_L E_{tan} \times TF dl, \end{aligned} \tag{3.1}$$

where  $\vec{E}_{inc}$  is the incident electric field along the pathways in the MRI RF field,  $L$  is the length of the lead body,  $E_{tan}$  is the tangential components of the  $\vec{E}_{inc}$  along the pathways,  $TF$  is the AIMD model, and  $V_{ind}$  is the induced voltage. One can further evaluate the  $V_{ind}$  in a discrete form as

$$V_{ind} \approx \Delta l \sum_{i=1}^N E_{tan}(i) \times TF(i), \tag{3.2}$$

where  $\Delta l$  is the step size (resolution) and  $N$  is the total number of segments for the discretized lead body. Using the transmission line model [38], the AIMD model can be expressed as

$$TF(i) = Ce^{jk_z i \Delta l} (1 - \Gamma_{tip} e^{-j2k_z i \Delta l}). \quad (3.3)$$

Then  $V_{ind}$  can be obtained by

$$V_{ind} \approx C \Delta l \sum_{i=1}^N E_{tan}(i) \times e^{jk_z i \Delta l} (1 - \Gamma_{tip} e^{-j2k_z i \Delta l}), \quad (3.4)$$

where  $k_z$  is the complex wavenumber of the transmission line model,  $C$  is the scaling coefficient to be determined, and  $\Gamma_{tip}$  is the complex reflection coefficient at tip part from the direction of the IPG to the tip. Since the AIMD models can be expressed by three complex terms, i.e.  $C$ ,  $k_z$  and  $\Gamma_{tip}$ , it is possible that we can perform several sets of independent measurements and use the measured voltage values to directly derive the AIMD model.

### 3.2.2 Selection of Appropriate Pathways

If  $M$  pathways are used, then  $M$  induced voltage values can be obtained. The equation (3.2) can be expressed in matrix form as

$$\mathbf{V}_{ind} = \Delta l \mathbf{E}_{tan} \cdot \mathbf{TF} \quad (3.5a)$$

or

$$\begin{bmatrix} V_{ind}^1 \\ V_{ind}^2 \\ \dots \\ V_{ind}^M \end{bmatrix} = \Delta l \begin{bmatrix} E_{tan}^{11} & E_{tan}^{12} & \dots & E_{tan}^{1N} \\ E_{tan}^{21} & E_{tan}^{22} & \dots & E_{tan}^{2N} \\ \dots & \dots & \dots & \dots \\ E_{tan}^{M1} & E_{tan}^{M2} & \dots & E_{tan}^{MN} \end{bmatrix} \begin{bmatrix} TF(1) \\ TF(2) \\ \dots \\ TF(N) \end{bmatrix}, \quad (3.5b)$$

where  $\mathbf{V}_{ind}$ ,  $\mathbf{E}_{tan}$  and  $\mathbf{TF}$  are the vector/matrix forms of  $V_{ind}$ ,  $E_{tan}$  and  $TF$ ,

$[E_{tan}^{i1}, E_{tan}^{i2}, \dots, E_{tan}^{iN}]$  is the  $1 \times N$  vector consisting of the tangential components of

the incident electric fields along the  $i^{th}$  pathway ,  $V_{ind}^i$  is the induced voltage at the AIMD IPG side along the  $i^{th}$  pathway and  $TF(i)$  is the  $i^{th}$  value of the AIMD model. The optimization procedure is to find the appropriate AIMD model parameters to satisfy the following equation

$$\mathbf{V}_{ind} - \Delta l \mathbf{E}_{tan} \cdot \mathbf{TF} = 0, \quad (3.6)$$

where  $\mathbf{TF}$  is the ideal AIMD model to be developed. Due to potential measurement errors in the induced voltages, the measured voltage is  $\hat{\mathbf{V}}_{ind} = \mathbf{V}_{ind} + \Delta \mathbf{V}_{ind}$ , where  $\Delta \mathbf{V}_{ind}$  is the perturbation of the  $V_{ind}$  that comes from errors including system errors and random errors. The approximate AIMD model minimizes the following equation

$$\left\| \hat{\mathbf{V}}_{ind} - \Delta l \mathbf{E}_{tan} \cdot \widehat{\mathbf{TF}} \right\|, \quad (3.7)$$

where  $\widehat{\mathbf{TF}}$  is the estimated AIMD model to be developed. Our aim is to solve the AIMD model by given induced voltage. As there is round-off error in induced voltage and electric field usually, the error needs to be estimated. Equation (3.6) can be transformed into

$$\mathbf{E}_{tan}^H \mathbf{V}_{ind} = \mathbf{E}_{tan}^H \mathbf{E}_{tan} \mathbf{TF}, \quad (3.8)$$

where  $\mathbf{E}_{tan}^H$  is the conjugate transpose of the  $\mathbf{E}_{tan}$ . The first order perturbation relation is

$$\Delta \mathbf{E}_{tan}^H \mathbf{V}_{ind} + \mathbf{E}_{tan}^H \Delta \mathbf{V}_{ind} = \Delta \mathbf{E}_{tan}^H \mathbf{E}_{tan} \mathbf{TF} + \mathbf{E}_{tan}^H \Delta \mathbf{E}_{tan} \mathbf{TF} + \mathbf{E}_{tan}^H \mathbf{E}_{tan} \Delta \mathbf{TF}, \quad (3.9)$$

which it is arranged to get

$$\begin{aligned}\Delta\mathbf{TF} &= (\mathbf{E}_{tan}^H \mathbf{E}_{tan})^{-1} \mathbf{E}_{tan}^H (\Delta\mathbf{V}_{ind} - \Delta\mathbf{E}_{tan} \mathbf{TF}) + \\ &\quad (\mathbf{E}_{tan}^H \mathbf{E}_{tan})^{-1} \Delta\mathbf{E}_{tan}^H (\mathbf{V}_{ind} - \mathbf{E}_{tan} \mathbf{TF}).\end{aligned}\quad (3.10)$$

If one defines  $\mathbf{r} = \mathbf{V}_{ind} - \mathbf{E}_{tan} \mathbf{TF}$ , (3.10) can be transformed into below equation by the definition of the second norm

$$\begin{aligned}\|\Delta\mathbf{TF}\| &\leq \left\| (\mathbf{E}_{tan}^H \mathbf{E}_{tan})^{-1} \mathbf{E}_{tan}^H \right\| (\|\Delta\mathbf{V}_{ind}\| + \|\Delta\mathbf{E}_{tan}\| \|\mathbf{TF}\|) + \\ &\quad \left\| (\mathbf{E}_{inc}^H \mathbf{E}_{inc})^{-1} \right\| \|\Delta\mathbf{E}_{tan}^H\| \|\mathbf{r}\|.\end{aligned}\quad (3.11)$$

Dividing through by  $\|\mathbf{TF}\|$  and doing some algebra so that  $\|\Delta\mathbf{E}_{tan}\|$  and  $\|\Delta\mathbf{V}_{ind}\|$  only appear in ratios with  $\|\mathbf{E}_{tan}\|$  and  $\|\mathbf{V}_{ind}\|$ , (3.11) can be transformed into

$$\begin{aligned}\frac{\|\Delta\mathbf{TF}\|}{\|\mathbf{TF}\|} &\leq \left\| (\mathbf{E}_{tan}^H \mathbf{E}_{tan})^{-1} \mathbf{E}_{tan}^H \right\| \|\mathbf{E}_{tan}\| \left( \frac{\|\Delta\mathbf{V}_{ind}\|}{\|\mathbf{V}_{ind}\|} \frac{\|\mathbf{V}_{ind}\|}{\|\mathbf{E}_{tan}\| \|\mathbf{TF}\|} + \frac{\|\Delta\mathbf{E}_{tan}\|}{\|\mathbf{E}_{tan}\|} \right) + \\ &\quad \left( \left\| (\mathbf{E}_{tan}^H \mathbf{E}_{tan})^{-1} \right\| \|\mathbf{E}_{inc}\|^2 \right) \frac{\|\Delta\mathbf{E}_{tan}^H\|}{\|\mathbf{E}_{tan}\|} \frac{\|\mathbf{r}\|}{\|\mathbf{E}_{tan}\| \|\mathbf{TF}\|},\end{aligned}\quad (3.12)$$

which is also

$$\begin{aligned}\frac{\|\Delta\mathbf{TF}\|}{\|\mathbf{TF}\|} &\leq \kappa(\mathbf{E}_{tan}) \left( \frac{\|\Delta\mathbf{V}_{ind}\|}{\|\mathbf{V}_{ind}\|} \frac{\|\mathbf{V}_{ind}\|}{\|\mathbf{E}_{tan}\| \|\mathbf{TF}\|} + \frac{\|\Delta\mathbf{E}_{tan}\|}{\|\mathbf{E}_{tan}\|} \right) + \\ &\quad \kappa^2(\mathbf{E}_{tan}) \frac{\|\Delta\mathbf{E}_{tan}^H\|}{\|\mathbf{E}_{tan}\|} \frac{\|\mathbf{r}\|}{\|\mathbf{E}_{tan}\| \|\mathbf{TF}\|},\end{aligned}\quad (3.13)$$

where  $\kappa(\mathbf{E}_{tan})$  is the condition number of  $\mathbf{E}_{tan}$ . A triangle is drawn to illustrate the relation between the  $\mathbf{E}_{tan}$ ,  $\mathbf{TF}$  and  $\mathbf{V}_{ind}$  in Fig. 3.1.

And we have

$$\frac{\|\mathbf{r}\|}{\|\mathbf{E}_{tan}\| \|\mathbf{TF}\|} \leq \frac{\|\mathbf{r}\|}{\|\mathbf{E}_{tan} \mathbf{TF}\|} = \tan \theta \quad (3.14a)$$

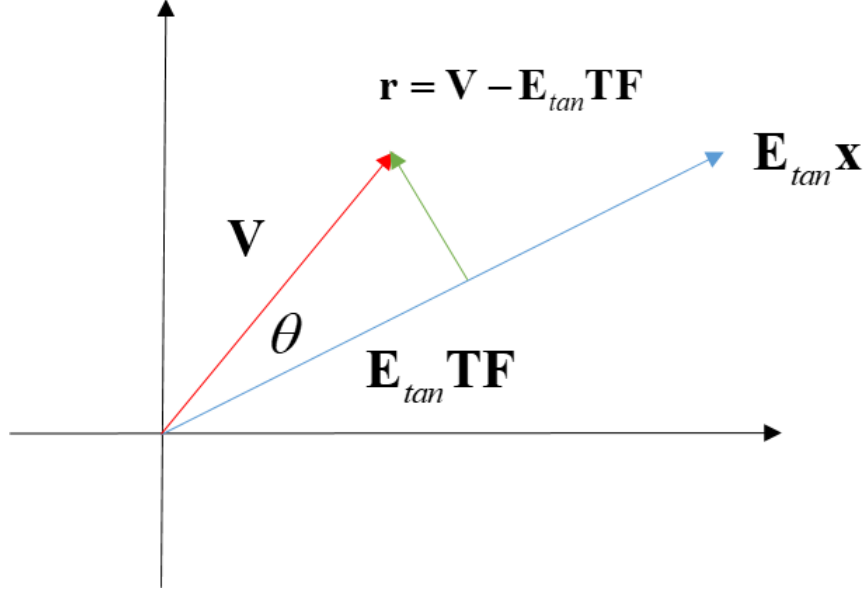


Fig. 3.1: The relation between the  $\mathbf{E}_{tan}$ ,  $\mathbf{TF}$  and  $\mathbf{V}_{ind}$ .

and

$$\frac{\|\mathbf{V}_{ind}\|}{\|\mathbf{E}_{tan}\| \|\mathbf{TF}\|} \leq \frac{\|\mathbf{V}_{ind}\|}{\|\mathbf{E}_{tan} \mathbf{TF}\|} = \frac{1}{\cos \theta}. \quad (3.14b)$$

Putting everything together, we have

$$\frac{\|\Delta \mathbf{TF}\|}{\|\mathbf{TF}\|} \leq (\kappa^2(\mathbf{E}_{tan}) \tan \theta + \kappa(\mathbf{E}_{tan})) \frac{\|\Delta \mathbf{E}_{tan}\|}{\|\mathbf{E}_{tan}\|} + \frac{\kappa(\mathbf{E}_{tan})}{\cos \theta} \frac{\|\Delta \mathbf{V}_{ind}\|}{\|\mathbf{V}_{ind}\|}. \quad (3.15)$$

As shown in [41], the upper bound of relative AIMD model error is proportional to the condition number with the relative difference of induced voltage for simplified form as

$$\frac{\|\widehat{\mathbf{TF}} - \mathbf{TF}\|}{\|\mathbf{TF}\|} \leq \kappa(\mathbf{E}_{tan}) \frac{\|\Delta \mathbf{V}_{ind}\|}{\|\mathbf{V}_{ind}\|}. \quad (3.16)$$

Hence in order to reduce the error in AIMD model development, the condition number of  $\mathbf{E}_{tan}$  should be small. Ideally, if the tangential components of the incident field along all the pathways are orthogonal to each other, the condition number would be equal to 1. A set of folded orthogonal pathways in phantom is proposed based on the Hadamard matrix [32] as shown in (2.9). The realization in the ASTM phantom is illustrated in Fig. 2.13. Since there are three complex unknowns to be solved, the induced voltages should be measured along at least 6 pathways if the phase information for the induced voltage cannot be estimated accurately. Once six individual measurements along six of the pathways described in Fig. 2.13 are performed, a global optimization method can be used to solve equation (3.7), the parameters in equation (2.4a) can be estimated to obtain the AIMD model.

### 3.2.3 Characteristic Impedance

As the AIMD model can be taken as a transmission line model, there will be character impedance for this model although it is not used here. This part will illustrate how to get the character impedance for an insulated solid lead in saline.

As shown in Fig. 3.2, an infinite dielectric coating wire has an inner conductor which its radius is  $a$ . And the outer radius is  $b$  with an permittivity of  $\epsilon_1$  and an permeability  $\mu_1$ . Out of the wire, it is infinite space with an permittivity of  $\epsilon_2$  and an permeability  $\mu_2$ .

The potential field of the transmission model along this coating wire can be expressed as

$$A_{z1} = e^{-jk_z z} [J_0(k_{\rho 1} \rho) + AY_0(k_{\rho 1} \rho)] \quad (3.17a)$$

and

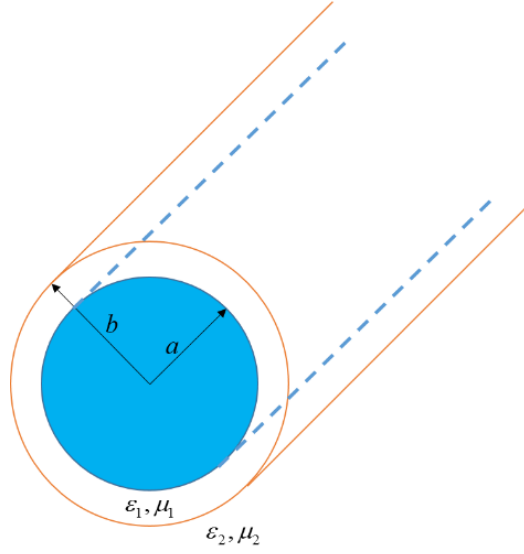


Fig. 3.2: The cross section of the infinite dielectric coating wire in homogeneous space.

$$A_{z2} = e^{-jk_z z} \left[ B H_0^{(2)}(k_{\rho 2} \rho) \right], \quad (3.17b)$$

where  $A_{z1}$  and  $A_{z2}$  are the potential field for the transmission line model,  $J_0$ ,  $Y_0$  and  $H_0^{(2)}$  are the Bessel functions of the zero order,  $A$  and  $B$  are the constant for the potential field, and  $k_{\rho 1}$  and  $k_{\rho 2}$  are the wave number along the radius direction which can be calculated by

$$k_{\rho 1} = \sqrt{k_1^2 - k_z^2} \quad (3.18a)$$

and

$$k_{\rho 2} = \sqrt{k_2^2 - k_z^2}, \quad (3.18b)$$

where  $k_1$  and  $k_2$  are the wave number of the dielectric coating and space,  $k_z$  is the wave number along the wire direction. When the region 2 is air,  $k_{\rho 2}$  is pure real number. If region 2 is a high permittivity material,  $k_{\rho 2}$  is pure imaginary or complex number, which is improper and it is a leaky mode. According to the electric field

boundary condition at the radius of a, we have

$$E_{z1} = 0 \quad @\rho = a, \quad (3.19)$$

which is

$$\frac{k_{\rho 1}}{j\omega\mu\varepsilon_1} e^{-jk_z z} [J_0(k_{\rho 1}a) + AY_0(k_{\rho 1}a)] = 0. \quad (3.20)$$

Then the constant  $A$  is

$$A = -\frac{J_0(k_{\rho 1}a)}{Y_0(k_{\rho 1}a)}. \quad (3.21)$$

To make it simple,

$$A_{z1} = e^{-jk_z z} [Y_0(k_{\rho 1}a) J_0(k_{\rho 1}\rho) - J_0(k_{\rho 1}a) Y_0(k_{\rho 1}\rho)]. \quad (3.22)$$

According to the electric field boundary condition at the radius of b, we have

$$E_{z1} = E_{z2} \quad @\rho = b, \quad (3.23)$$

which is also

$$\frac{k_{\rho 1}^2}{j\omega\mu\varepsilon_1} e^{-jk_z z} [Y_0(k_{\rho 1}a) J_0(k_{\rho 1}b) - J_0(k_{\rho 1}a) Y_0(k_{\rho 1}b)] = \frac{k_{\rho 2}^2}{j\omega\mu\varepsilon_2} e^{-jk_z z} BH_0^{(2)}(k_{\rho 2}b). \quad (3.24)$$

Then the constant  $B$  is

$$B = \frac{\varepsilon_2 k_{\rho 1}^2 Y_0(k_{\rho 1}a) J_0(k_{\rho 1}b) - J_0(k_{\rho 1}a) Y_0(k_{\rho 1}b)}{\varepsilon_1 k_{\rho 2}^2 H_0^{(2)}(k_{\rho 2}b)}. \quad (3.25)$$

According to the magnetic field boundary condition at the radius of b, we have

$$H_{\phi 1} = H_{\phi 2} \quad @\rho = b, \quad (3.26)$$

which is also

$$\frac{-k_{\rho 1}}{\mu_1} e^{-jk_z z} [Y_0(k_{\rho 1} a) J_0'(k_{\rho 1} b) - J_0(k_{\rho 1} a) Y_0'(k_{\rho 1} b)] = \frac{-k_{\rho 2}}{\mu_2} e^{-jk_z z} B H_0^{(2)'}(k_{\rho 2} b). \quad (3.27)$$

Here  $k_z$  can be solved numerically. Then the character impedance is calculated by

$$\begin{aligned} Z_s &= \left. \frac{E_z}{H_\phi} \right|_{\rho=b} = \frac{\frac{1}{j\omega\mu_1\varepsilon_1} k_{\rho 1}^2 A_{z1}}{-\frac{1}{\mu_2} \frac{\partial A_{z2}}{\partial \rho}} \\ &= -\frac{k_{\rho 1}}{j\omega\varepsilon_1} \frac{Y_0(k_{\rho 1} a) J_0(k_{\rho 1} b) - J_0(k_{\rho 1} a) Y_0(k_{\rho 1} b)}{Y_0(k_{\rho 1} a) J_0'(k_{\rho 1} b) - J_0(k_{\rho 1} a) Y_0'(k_{\rho 1} b)}. \end{aligned} \quad (3.28)$$

The wave number and character impedance are the same as the result in [38].

### 3.3 Experimental Studies

In experimental studies, the heating and voltage AIMD model of two different AIMDs were measured and their induced voltage and heating models under a 1.5 T MRI system were developed using the method described above. The Medical Implant Test System MITS 1.5 (Zurich MedTech ZMT, Zurich, Switzerland), illustrated in Fig. 3.3, was used to emulate the RF exposure of the implant in MRI scanners. The RF coil of the MITS 1.5 system was implemented as a band-pass birdcage coil. The birdcage coil is 650 mm long and has an inner diameter of 700 mm. The MITS 1.5 system can generate a circular polarized RF magnetic fields.

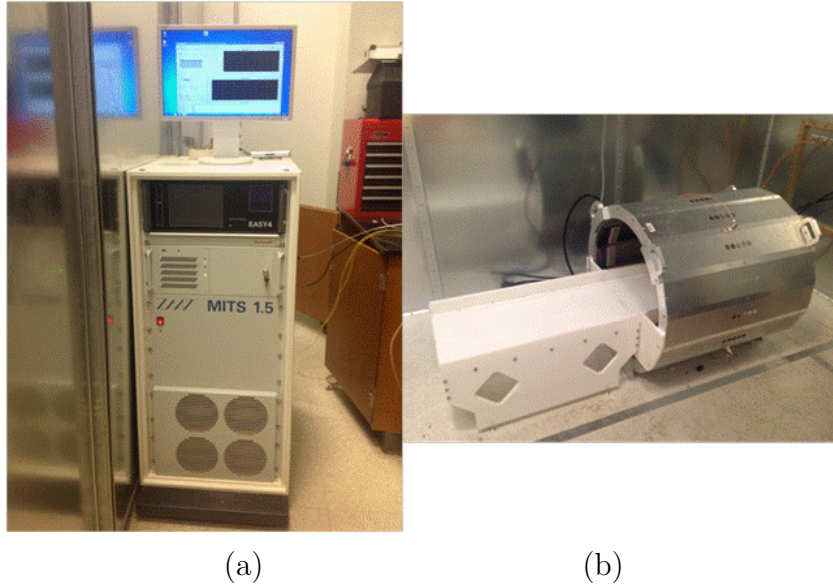


Fig. 3.3: MITS 1.5 System. (a) Amplifiers and software parts; (b) RF gradient coil.

### 3.3.1 AIMD Model for Induced Voltage

For induced voltage measurements, a 52 cm long lead was used with the IPG. This is a commercially available device with 3 electrodes at the distal end of the lead. These electrodes are connected to 3 inner conductors which are parallel to each other in a helical winding pattern. And these conductors are encapsulated inside an insulating layer. An SMA (SubMiniature version A) connector was attached to the IPG to pick the induced voltage between the inner conductor and the case of the IPG. The waterproof clay covered the connection part of the SMA and the IPG. The lead was fixed by rubber bands on a plastic mesh grid as in Fig. 3.4. By placing the lead inside the ASTM phantom along eight U-shaped folded pathways shown in Fig. 2.13, the induced voltage values were measured using an oscilloscope.

The tangential components of the incident fields along all 8 pathways are shown in Fig. 3.5. The magnitudes and phases of the tangential electric fields along these

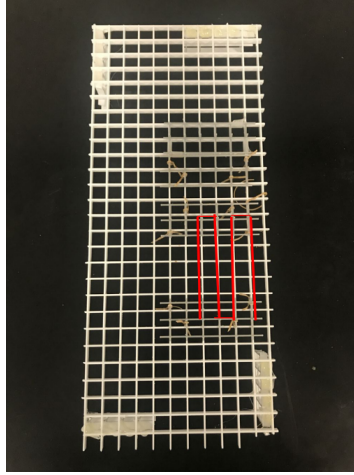
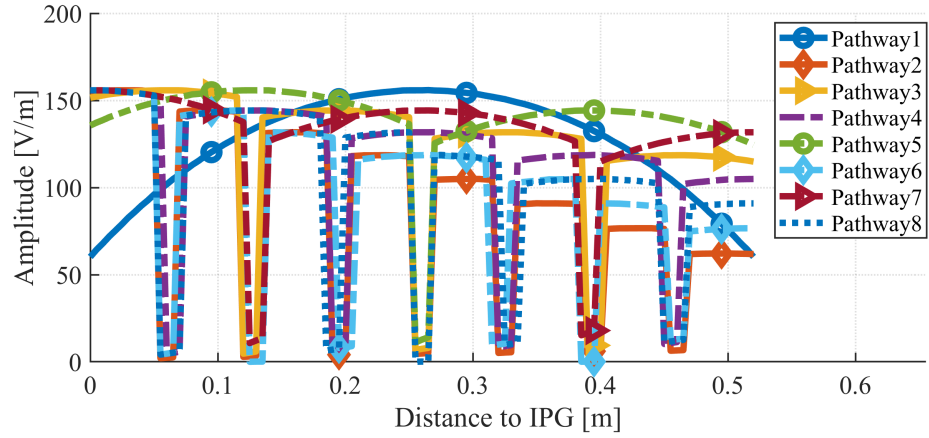


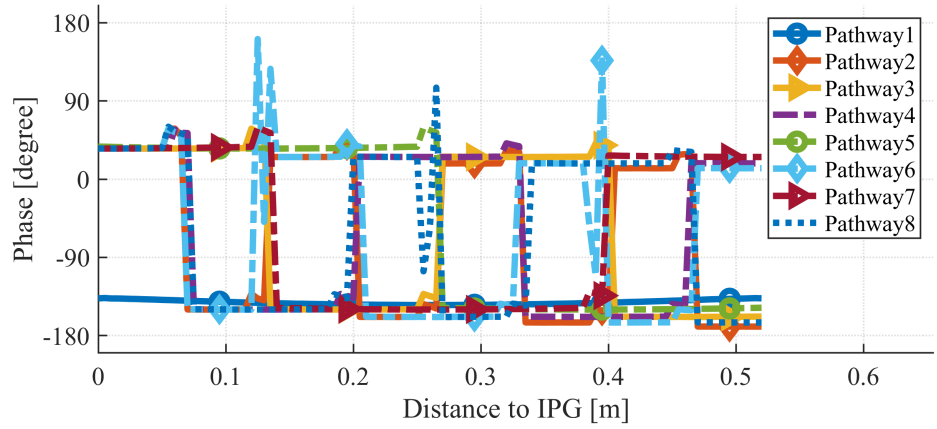
Fig. 3.4: Plastic mesh grid used for fixing the lead.

pathways resemble row elements in the Hadamard matrix changing from 1 to  $-1$  or  $-1$  to 1 [32]. As shown in Fig. 3.5(b), the phase change along each pathway ensures the quasi-orthogonality of the tangential components of the incident fields along the pathways. Furthermore, the eigenvalues of the tangential components of the incident fields are shown in Fig. 3.5(c). These eigenvalues are very close to each other. This means the tangential components of the incident fields along these pathways can be considered as almost orthogonal to each other. With such a condition number around 2.4, a small error in the AIMD development is expected [40].

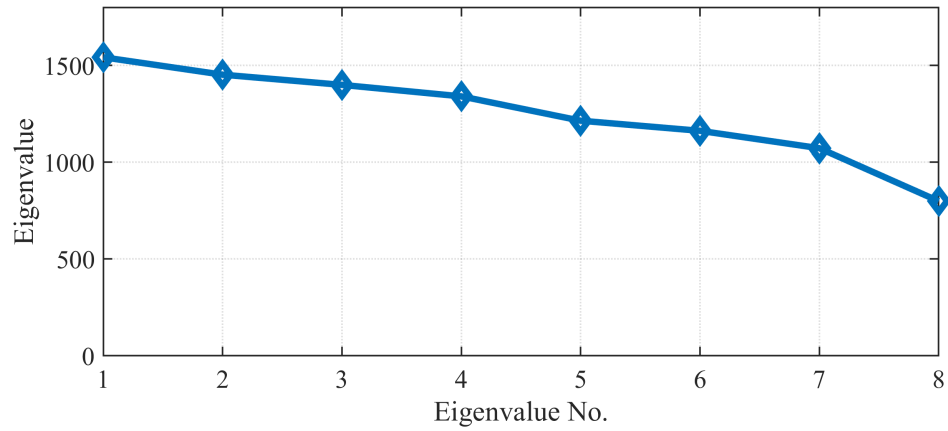
Using the method described earlier, the developed AIMD model is shown in the blue line in Fig. 3.6 using measured results along all eight pathways. For comparison, the measured AIMD model based on the reciprocity method was also shown in the red line in the same figure [25]. As seen from the results, these two AIMD models agree very well with each other. The induced voltages obtained through direct measurements and estimated using the proposed approach are shown in Fig. 3.7. As shown in the figure, the consistency of the estimated and measured induced voltages



(a)



(b)



(c)

Fig. 3.5: (a) Magnitude of the tangential components of the incident fields along U-shaped folded pathways; (b) Phase of the tangential components of the incident fields along U-shaped folded pathways; (c) Eigenvalues of the tangential components of the incident field.

confirms that the developed model based on the semi-analytical model is effective in predicting the induced voltage.

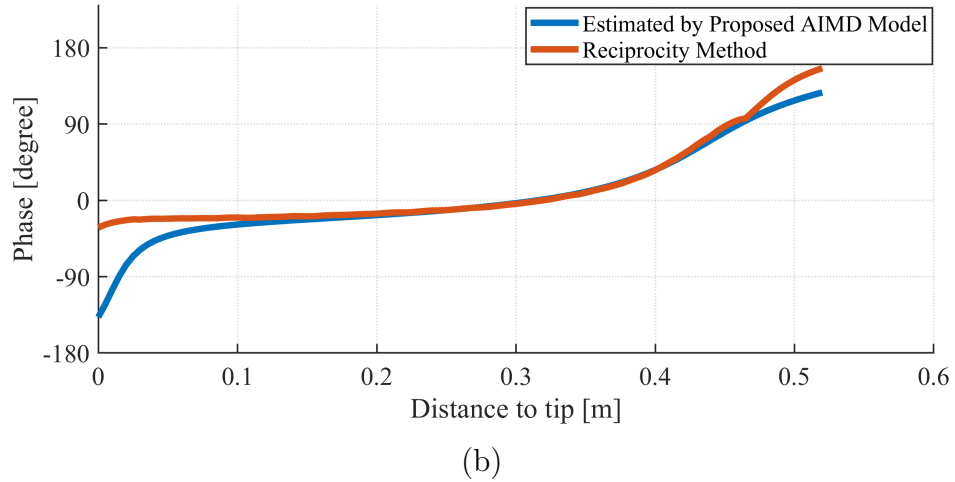
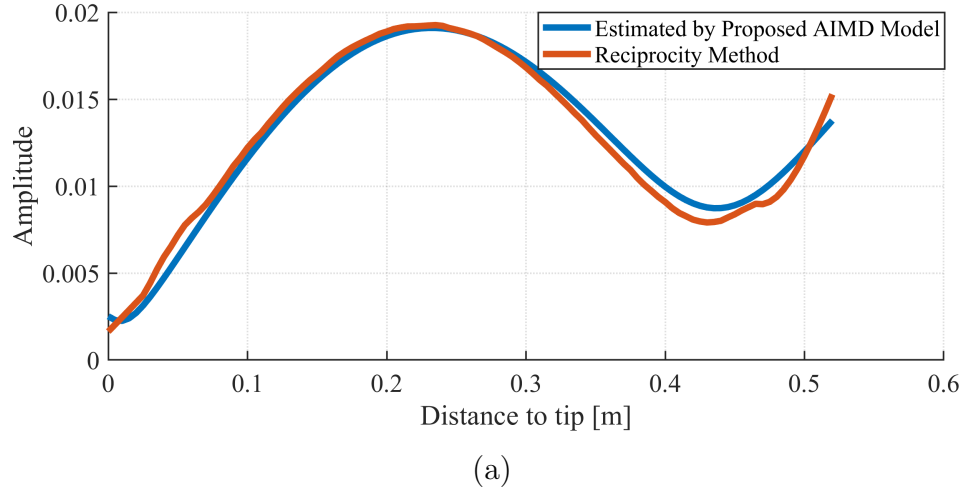


Fig. 3.6: Comparison of voltage transfer functions through proposed method and reciprocity method (a) Magnitude of AIMD models, (b) Phase of AIMD models.

To further validate the developed AIMD model, another set of validation pathways were proposed as shown in Fig. 3.8. These pathways were selected since they can lead to higher induced voltages for a higher signal to noise ratio. However, the condition number of the  $\mathbf{E}_{tan}$  is 16.8. Therefore, it is more appropriate for validation rather

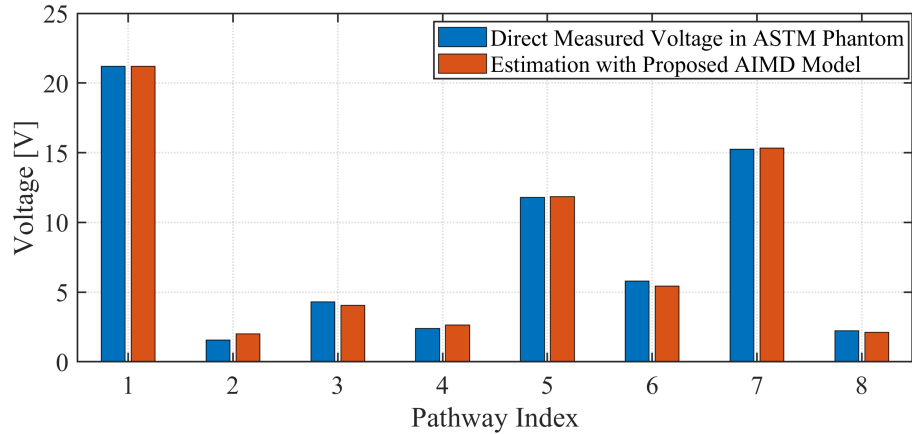


Fig. 3.7: Comparison of induced voltages from direct measurement in ASTM phantom and predicted ones using the AIMD model developed in the study.

than AIMD model development.

The validation results are shown in Fig. 3.9. The relative errors between the direct measurements and estimations by the developed AIMD models using the semi-analytical model are within 15 %. Besides, the relative errors of estimation with AIMD model using the reciprocity method and estimation with the proposed AIMD model compared to the direct measurement are also shown. As shown in the figure, the relative errors of these two models are very similar.

### 3.3.2 AIMD Model for Induced Heating

To demonstrate the effectiveness of this approach for AIMD induced heating model development, a 38 cm long lead was used in the measurements. This system is a commercial neuro-stimulation system with 4 electrodes at the distal end of the lead. An optical fiber thermal probe was fixed to the electrode to measure the temperature rises. Similar pathways as used earlier were used for model development, but each segment length was shorter since the overall device length was shorter. The tangential

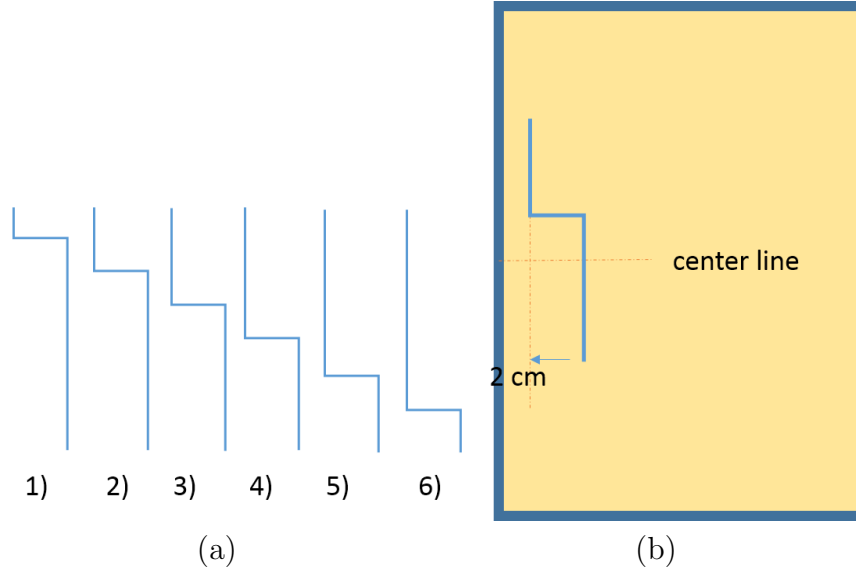
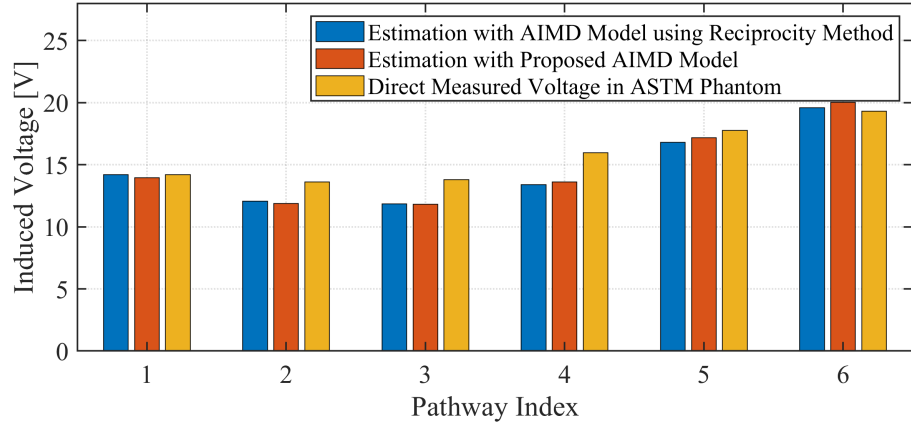
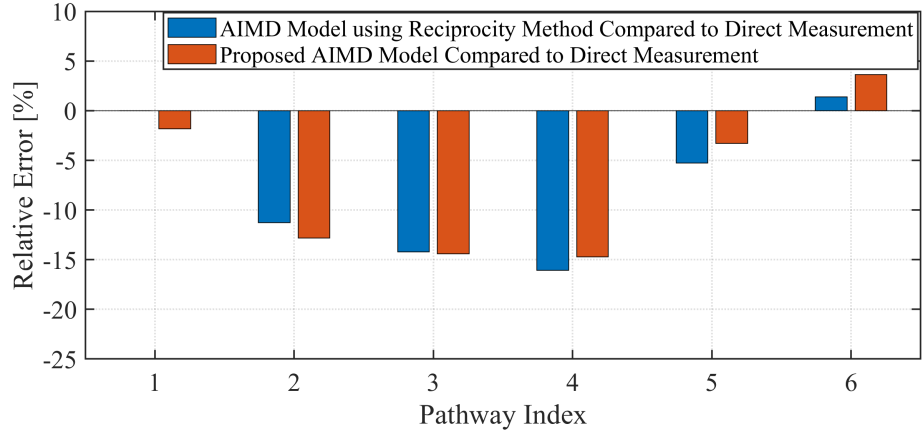


Fig. 3.8: (a) Z-shaped validation pathways; (b) Pathway position in ASTM phantom.

components of the incident fields and their eigenvalue are shown in Fig. 3.10. The tangential components of the incident fields along each pathway can be also considered quasi-orthogonal since the condition number is 2.0. The comparison of the AIMD models obtained from both methods was provided in Fig. 3.10. The tangential components of the incident fields along each pathway can be also considered quasi-orthogonal since the condition number is 2.0. The comparison of the AIMD models obtained from both methods was provided in Fig. 3.11. Again, we can see that the AIMD models for the RF induced-heating agree well with each other. It is shown that the AIMD model developed using the reciprocity method has increased magnitude near the tip electrode. This is probably caused by the direct coupling between the excitation and the current probe. At this point, the AIMD model developed by the semi-analytical model can prevent the disturbance by the equipment of the AIMD model measurement. The induced heating along these pathways was also shown in Fig. 3.12, indicating that the developed model can accurately predict the induced



(a)

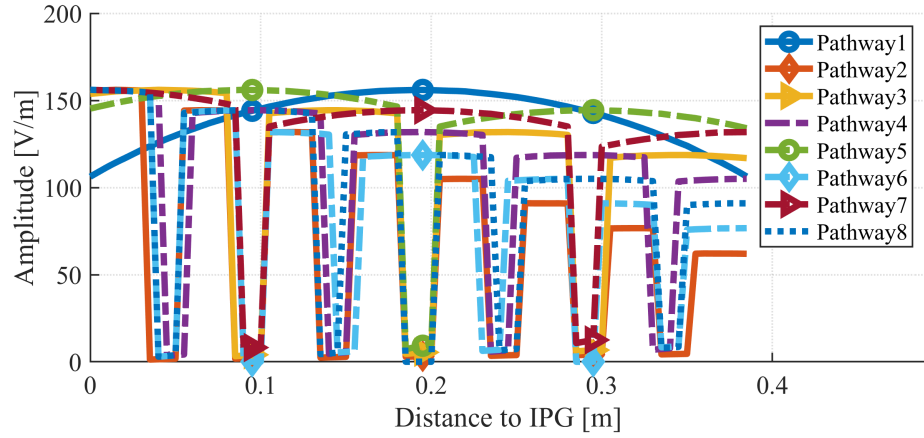


(b)

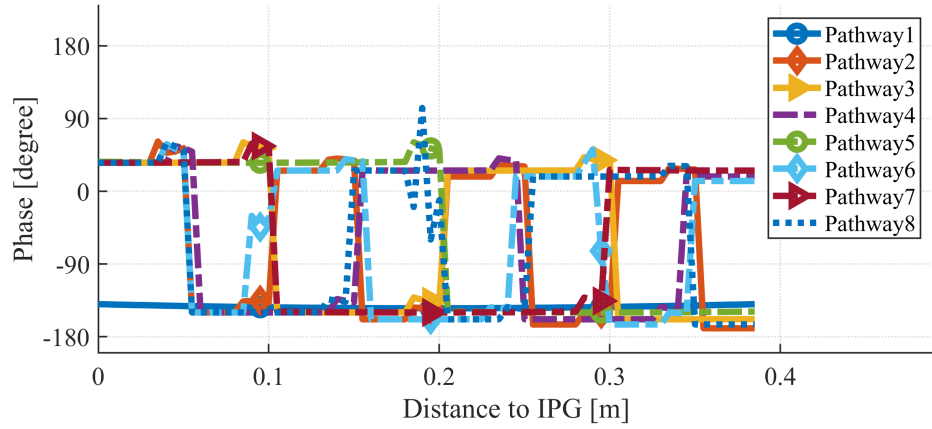
Fig. 3.9: (a) Comparison of induced voltages between estimation with AIMD model using reciprocity method, estimation with proposed AIMD model and directly measured voltage in ASTM phantom; (b) the relative errors between direct measurement and estimation from different AIMD models.

RF heating. As clearly indicated in the figure, the AIMD model developed by the semi-analytical model can effectively predict induced heating over a large range of temperature rises.

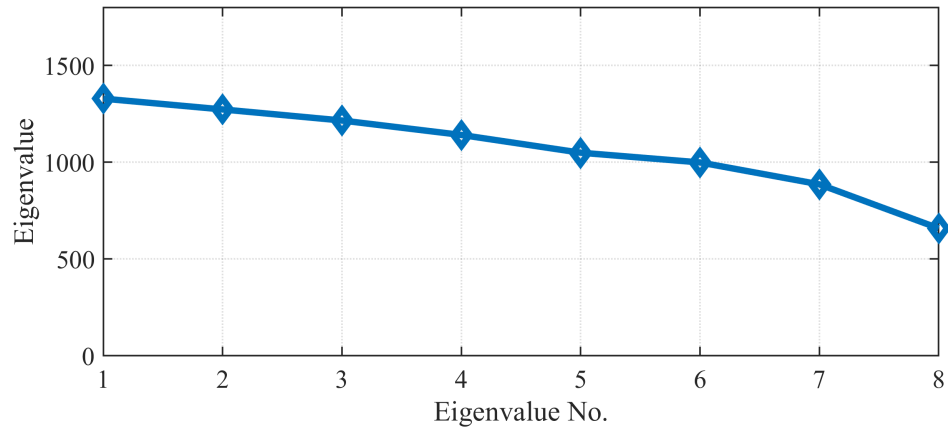
Using the same concept in Fig. 3.8, the validation study was performed for the developed heating AIMD model. The condition number of the  $\mathbf{E}_{tan}$  is 16.8. The induced heating for each pathway becomes generally higher than the folded ones. The relative error of the estimation with the proposed AIMD model is below 15% as shown in the figure.



(a)

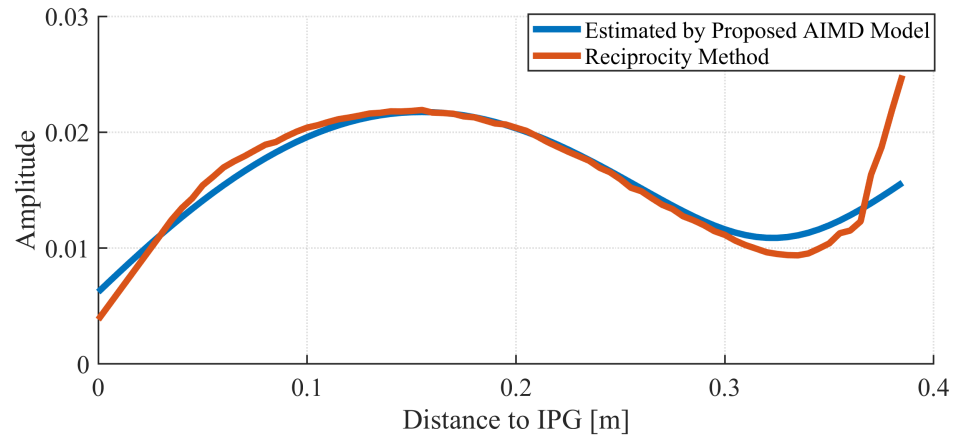


(b)

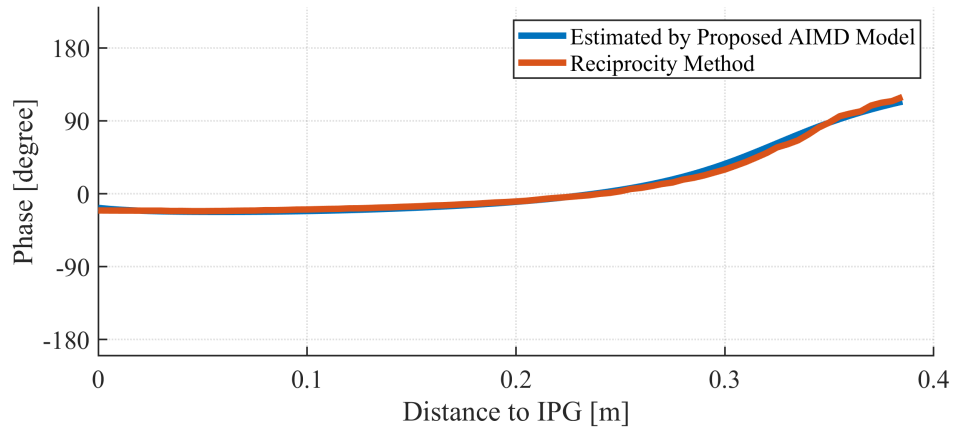


(c)

Fig. 3.10: (a) Magnitude of the tangential components of the incident fields along U-shaped folded pathways; (b) Phase of the tangential components of the incident fields along U-shaped folded pathways; (c) Eigenvalues of the tangential components of the incident fields.



(a)



(b)

Fig. 3.11: Comparison of heating transfer functions through proposed method and reciprocity method (a) Magnitude of AIMD models, (b) Phase of AIMD models.

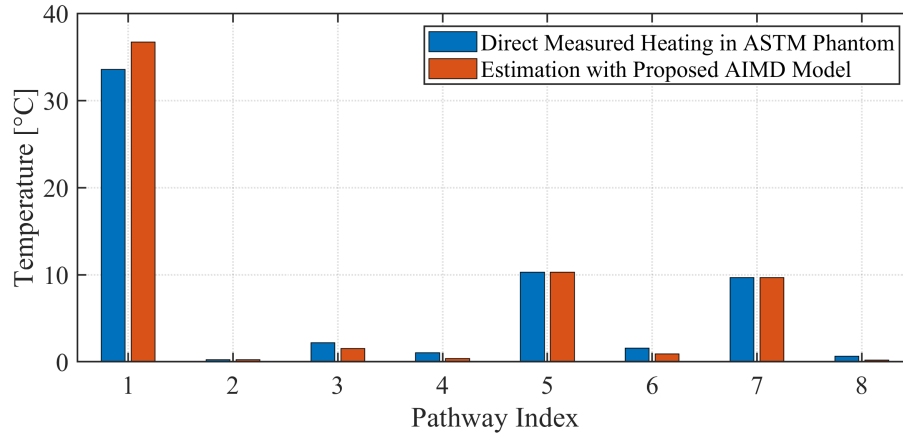


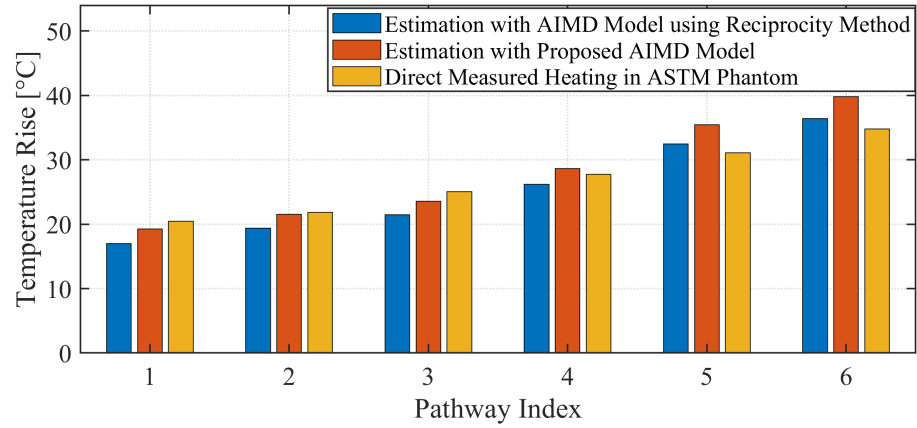
Fig. 3.12: Comparison of induced temperature rises from direct measurement and predicted ones using the AIMD model developed in the study.

### 3.4 Optical Fiber Effects on the AIMD model

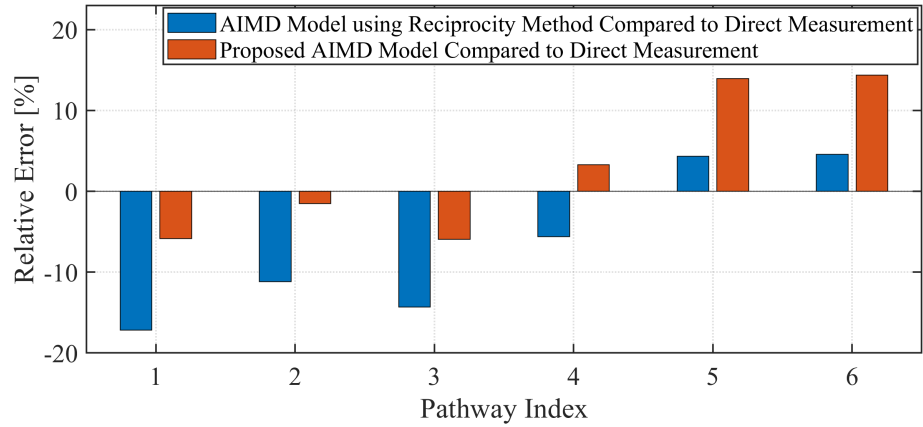
This part investigates the effect of fiber optic probe on the AIMD model development. When the AIMD is under heating measurement in the RF field, an optic fiber temperature probe shall be used to measure the temperature rise to avoid potential influence from the metal parts of the probe. During the measurement, the probe shall be attached to the lead tightly, which may change the AIMD model under test. Hence, it is necessary to investigate the TF of a lead with or without a fiber optic probe attached. Both simulation and experiment were used to investigate the effect of an optic fiber near lead.

#### 3.4.1 Numerical Study

In the first step, a solid lead connected to a dummy IPG, as shown in Fig. 3.14, was simulated using reciprocity method. The solid lead is composed of an inner conductor and an insulation layer. The inner conductor has a radius of 0.4 mm and is made of PEC. The insulation layer has a radius of 0.8 mm and is made of Teflon



(a)



(b)

Fig. 3.13: (a) Comparison of induced heating between estimation with AIMD model using reciprocity method, estimation with proposed AIMD model and directly measured voltage in ASTM phantom; (b) the relative errors between direct measurement and estimation from different AIMD models.

with a relative permittivity of 3.0. The length of lead is 30 cm and it is connected to a dummy IPG. The source of this lead was applied on the distal end of lead. The AIMD model of the solid lead was extracted after simulation was completed.

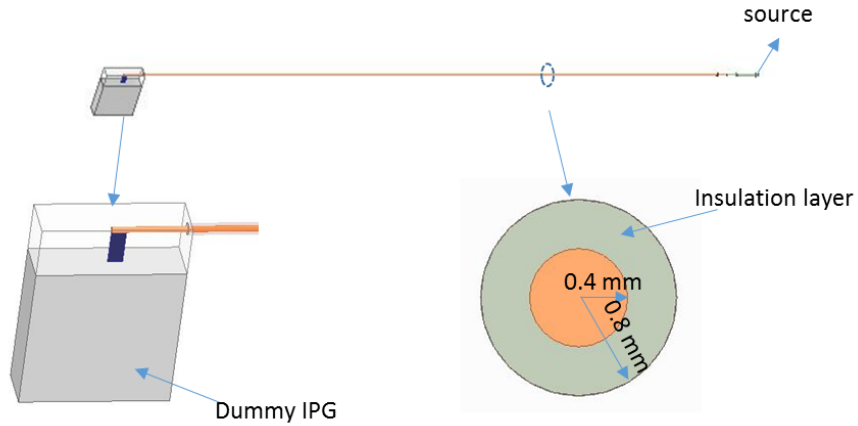


Fig. 3.14: Lead model of the insulated solid wire.

In the second step, a solid lead with an optic fiber attached was simulated as shown in Fig. 3.15.

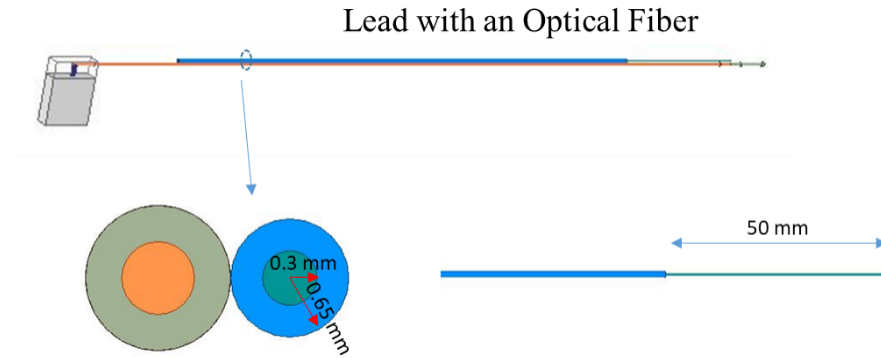


Fig. 3.15: The insulated solid lead with an optic fiber.

All the simulation setup was the same as the previous simulation except that an optic fiber was attached in parallel to the lead. The optic fiber model has the same

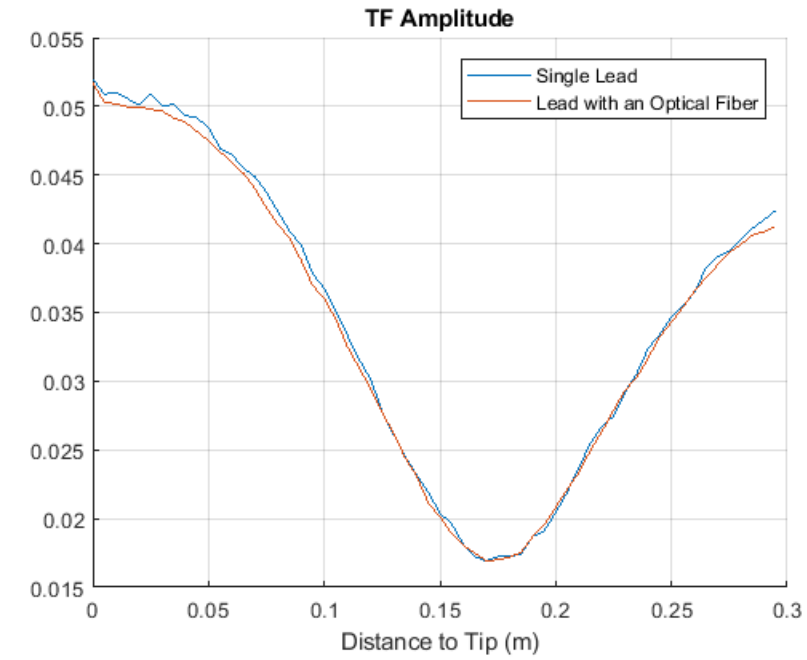
structure of a T1S-05-PT05 probe from Neoptix which contains two layers. The inner layer is made of silica with a relative permittivity of 3.8 and a radius of 0.4 mm. The outer layer is made of Teflon with a relative permittivity of 2.1 and a radius of 0.8 mm. The tip part of the optic fiber is 50 mm long as shown in Fig. 3.15. The AIMD model of the lead with the optic fiber was also extracted using the reciprocity method.

The comparison of the AIMD models for these two cases are shown in Fig. 3.16. It is shown that the amplitude and the phase of both AIMD models agree well with each other. From the simulation result, the effect of an optic fiber is negligible.

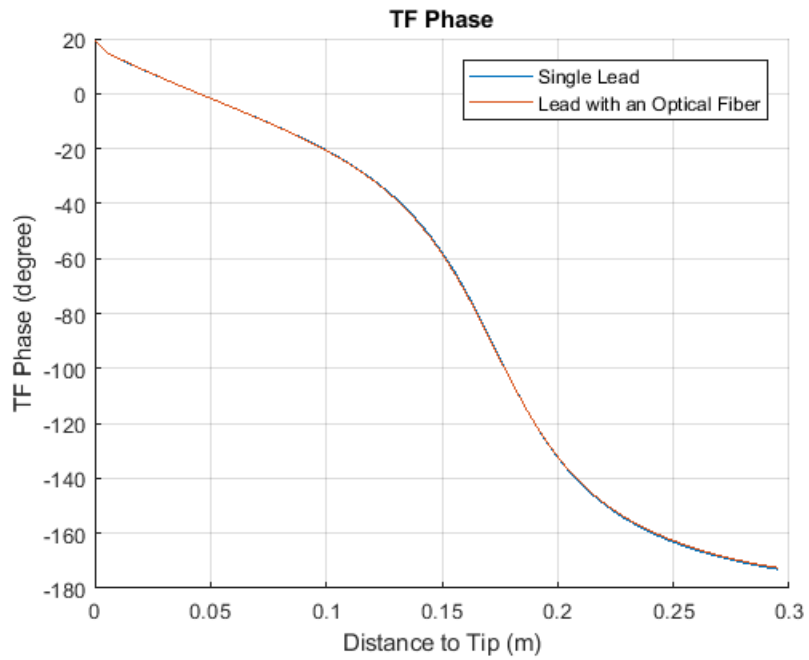
### **3.4.2 Experimental Validation**

The heating AIMD models of a commercial lead with or without an optic fiber attached were also measured using the reciprocity method. The optic fiber model is T1S-05-PT05 from Neoptix. The tip of the optic fiber was attached to the lead as shown in Fig. 3.17, which has the same setup when the heating was measured inside a RF environment. By measuring the AIMD model shapes in both cases, the amplitude and phase were compared.

The measurement results are shown in Fig. 3.18. The amplitude and phase of both AIMD model shapes agree well with each other. From the experiment result, the AIMD model shape of the lead with an optic fiber is the same as that of the lead without an optic fiber attached.



(a)



(b)

Fig. 3.16: (a) The AIMD model amplitude of the lead only and the lead with an optic fiber attached in simulation; (b) the AIMD model phase of the lead only and the lead with an optic fiber attached in simulation.

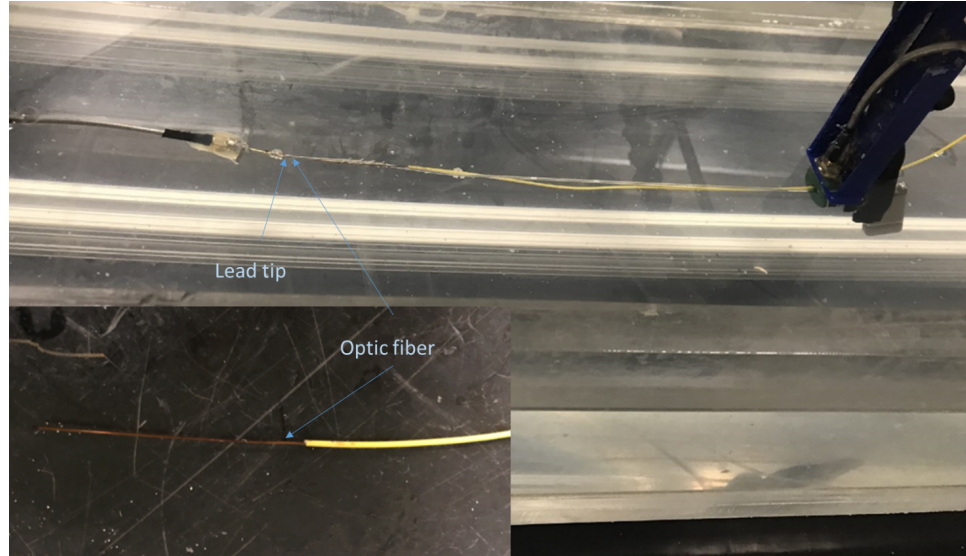


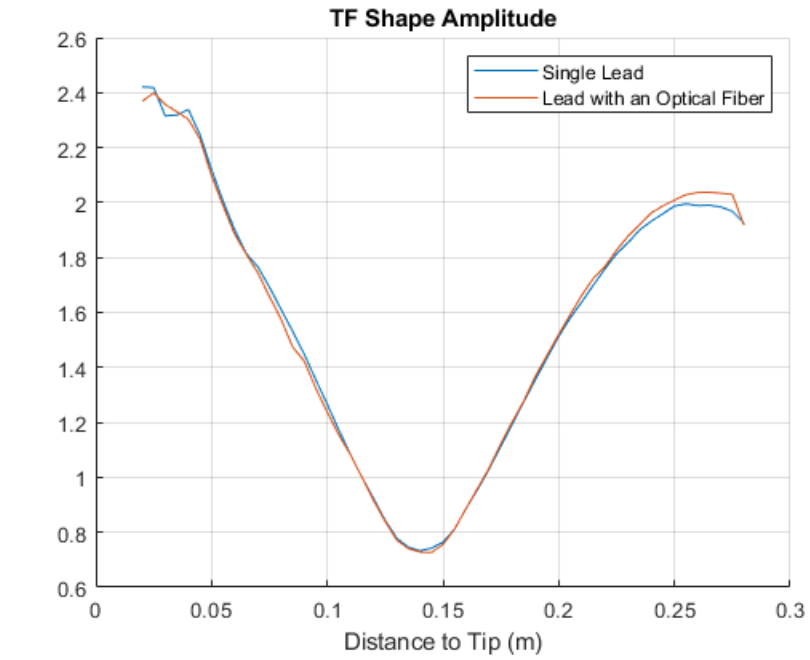
Fig. 3.17: The AIMD model measurement setup of the lead with an optic fiber.

### 3.4.3 Discussion

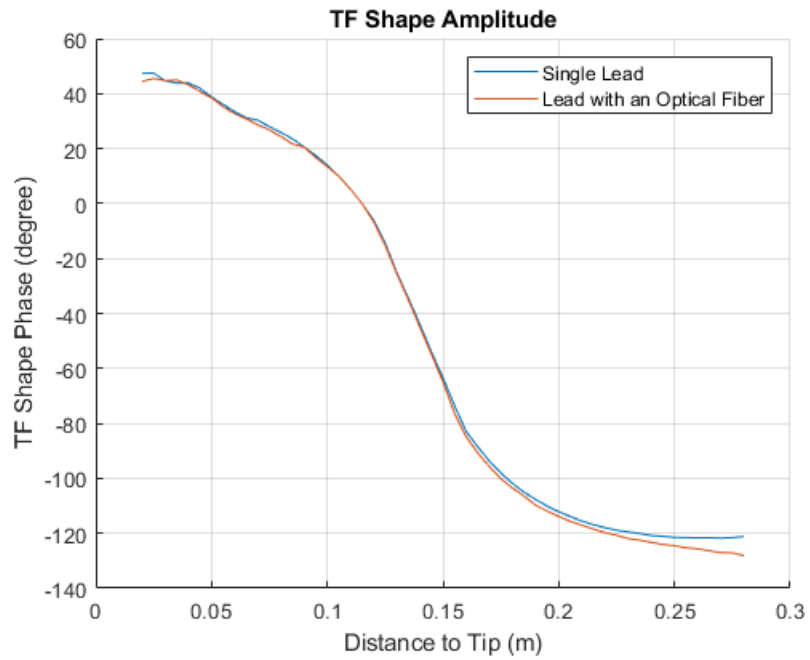
Both simulation and experiment methods were used to investigate the difference between the AIMD models of a lead with or without an optic fiber attached. In the simulation, a solid lead only and a solid lead with an optic fiber attached were simulated to extract the AIMD models using the reciprocity method. In the experiment, AIMD models of a commercial lead only and a commercial lead with an optic fiber attached were measured using the reciprocity method. The AIMD models of both cases in simulation and experiment were compared. Based on the results, it is concluded that the optic fiber has minimum effect on the AIMD model development.

## 3.5 Bending Effects on the AIMD Model

During the AIMD model inversion, folded pathways were used to develop the AIMD model. As the AIMD model is based on the transmission line model, it is necessary to investigate whether the AIMD model of the lead along folded pathways



(a)



(b)

Fig. 3.18: (a)The AIMD model shape amplitude of the lead only and the lead with an optic fiber attached in experiment; (b) the AIMD model shape phase of the lead only and the lead with an optic fiber attached in experiment.

changes. The change may come from the bending parts or the coupling from near folded parts. In this part, a solid lead was used in both simulation and experiment to study the AIMD model change when the pathway changes. Also a helical lead was used in experiment.

### 3.5.1 Numerical Study

An insulated solid lead was used in simulation as shown in Fig. 3.19. The solid lead is composed of an inner conductor and an insulation layer. The conductor has a radius of 0.4 mm and is made of PEC. The insulation layer has a radius of 0.8 mm and is made of Teflon with a relative permittivity of 3.0. The length is 40 cm and the tip part is 10 mm. The source of this lead was applied on the end of the lead.

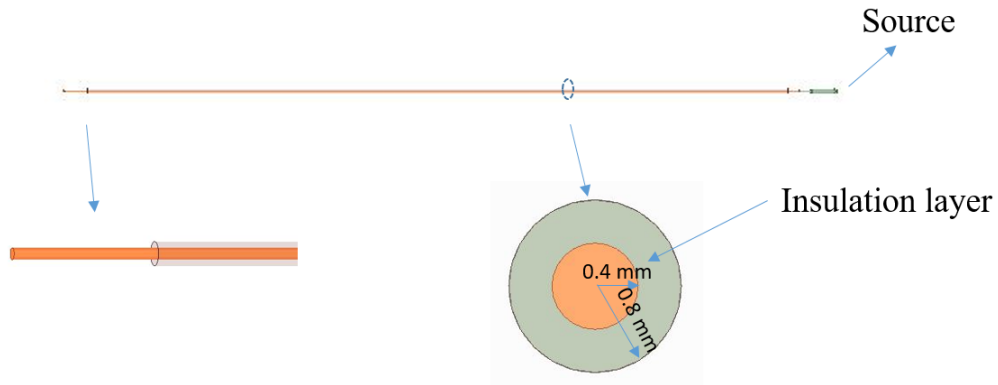


Fig. 3.19: Simulation model of the insulated solid lead.

According to the transmission line theory, discontinuity effects can become important at high frequency. And the bending parts of the transmission line may cause the wave reflected and induce radiation effects. Twin leads and balun structure can reduce this effects. The AIMD model contains multiple conductors with helical winding. For simulation, it is difficult to model the exact same structure and helical

winding. Hence, the single insulated solid lead was used here. By changing the lead path, straight, L shape and U shape were studied as shown in Fig. 3.20.

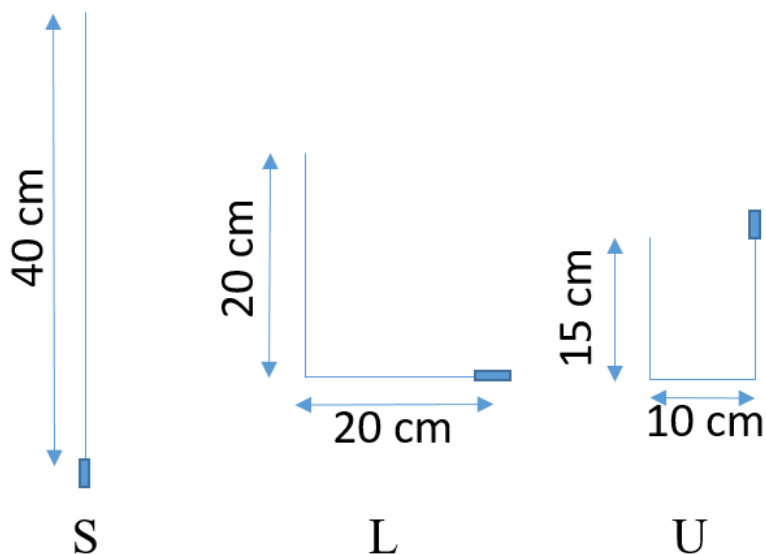


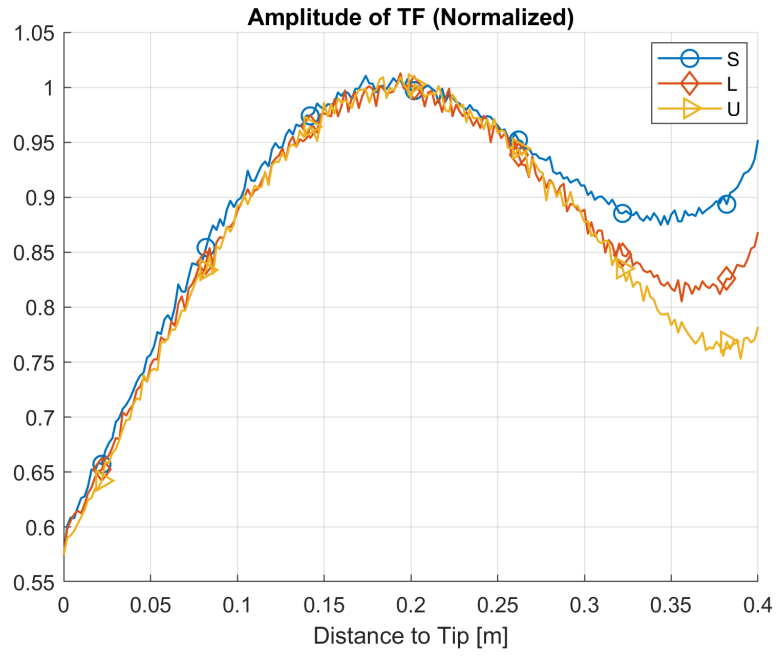
Fig. 3.20: Lead path of the insulated solid lead.

The AIMD models were extracted using the reciprocity method and compared as shown in Fig. 3.21. The phase of the AIMD models keeps nearly the same. The amplitude of the AIMD models changes when the pathway changes.

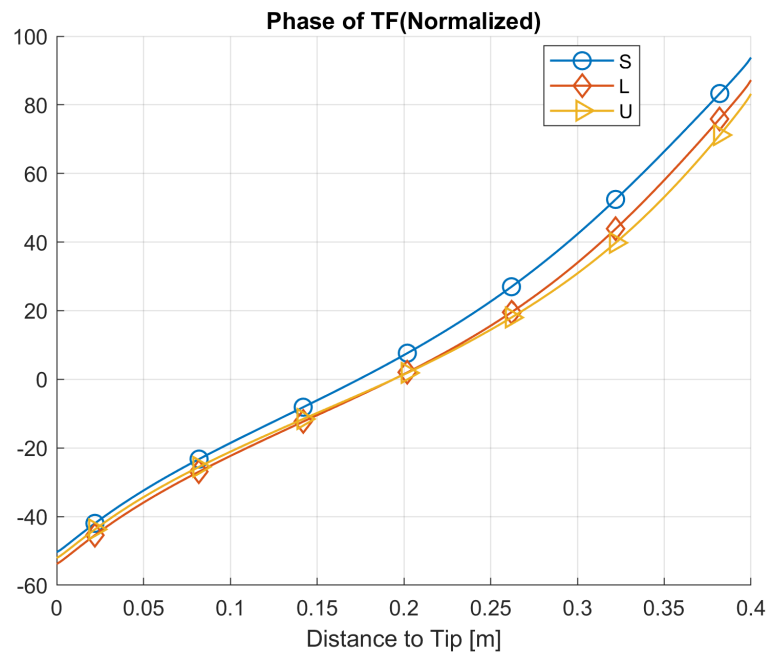
Hence the bending changes the AIMD model of the insulated solid lead. It is possible that the wave reflected at the bending parts. Based on this assumption, an AIMD model with multiple parts of the transmission line model was proposed [42]. For each bending part as shown in Fig. 3.22, a separate transmission line model was used.

For part *a*, the AIMD model is

$$TF(z) = C_1 e^{-jk_z z} (1 - \Gamma_1 e^{+j2k_z z}). \quad (3.29)$$



(a)



(b)

Fig. 3.21: (a) Amplitude of the AIMD model along S, L and U pathway in simulation; (b) Phase of the AIMD model along S, L and U pathway in simulation.

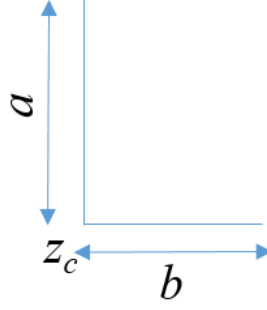


Fig. 3.22: Lead path of the insulated solid lead.

For part  $b$ , the AIMD model is

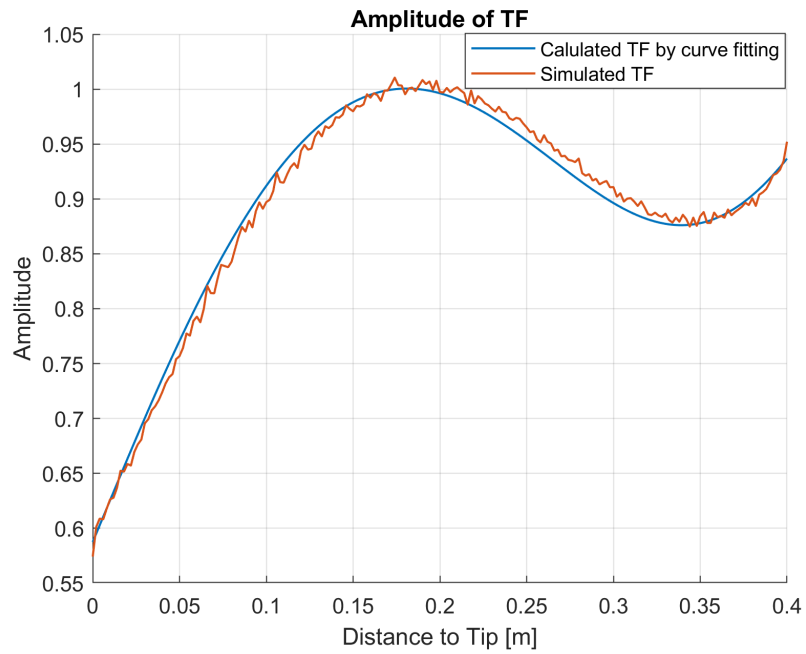
$$TF(z) = C_2 e^{-jk_z z} (1 - \Gamma_1 e^{+j2k_z z}). \quad (3.30)$$

For bending corner  $z_c$ , the AIMD model is

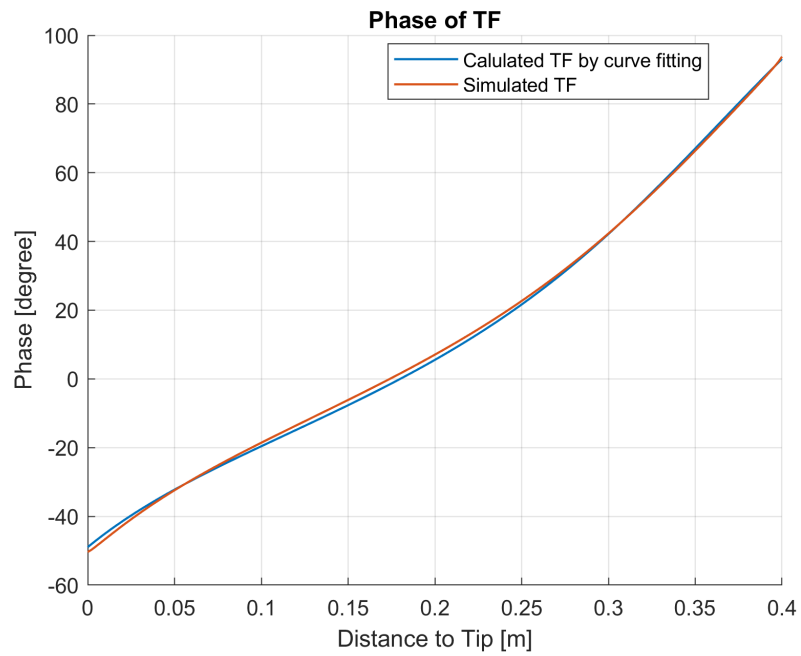
$$C_1 (1 - \Gamma_1 e^{+j2k_z z_c}) = C_2 (1 - \Gamma_2 e^{+j2k_z z_c}). \quad (3.31)$$

where  $C_1$  and  $C_2$  are the constants for the transmission line models at part  $a$  and  $b$ ,  $z_c$  is the position at the bending corner. Although the reflection coefficient and the constant are different for different parts, the wave number  $k_z$  keeps the same. Besides, for the insulated lead, the wave number can be calculated which has been introduced in details in the previous section. By using the (3.29), (3.30) and (3.31), curve fitting method was used to calculate  $k_z$ . For the straight pathway, the  $k_z$  by curve fitting is  $6.92 - j1.16$  and that by formula is  $6.90 - j1.04$ . The amplitude and phase were shown in Fig. 3.23. The calculated  $k_z$  is quite close to one by the formula.

The AIMD models along L pathway by curve fitting and simulation were as shown in Fig. 3.24. The AIMD model by curve fitting is quite close to that in simulation.



(a)



(b)

Fig. 3.23: (a) Amplitude of the AIMD model along S pathway by simulation and curve fitting; (b) Phase of the AIMD model along S pathway by simulation and curve fitting.

The  $k_z$  in the curve fitted model is  $6.72 - j1.05$  which is also close to the  $k_z$  calculated by formula.

The AIMD model along U pathway by curve fitting and simulation were as shown in Fig. 3.25. The AIMD model by curve fitting is still close to that in simulation. The  $k_z$  in the curve fitted model is  $6.92 - j1.16$ .

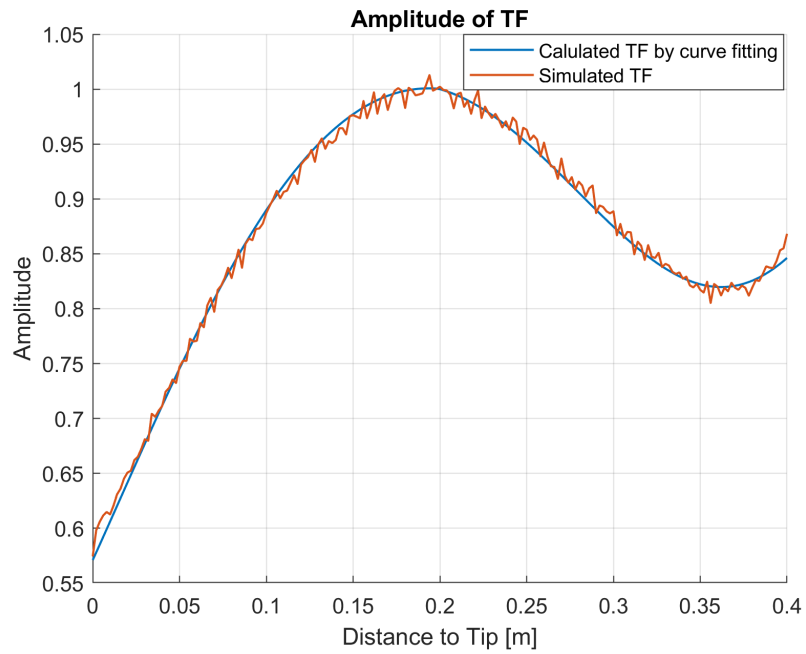
Besides, the reflection coefficients at the tip part for different pathways should keep the same if the separate transmission line model holds. The reflection coefficient and  $k_z$  are given in Table 2. From the data, the reflection coefficient and  $k_z$  are quite stable when the pathway changes. Besides, the  $k_z$  calculated by curve fitting is quite close to that by formula. Hence, there is reflection at the bending when the pathway changes and the AIMD model changes for leads with structure like the insulated solid lead. During the experiment in previous section, helical winding leads were used and that is the reason. Although leads with helical winding and multiple conductors are challenging for simulation, experimental validation is still available. In next part, the experimental validation for the insulated solid lead and the helical winding lead was performed.

Table 2: The Wave Number and Reflection Coefficient of the AIMD model along Different Pathways.

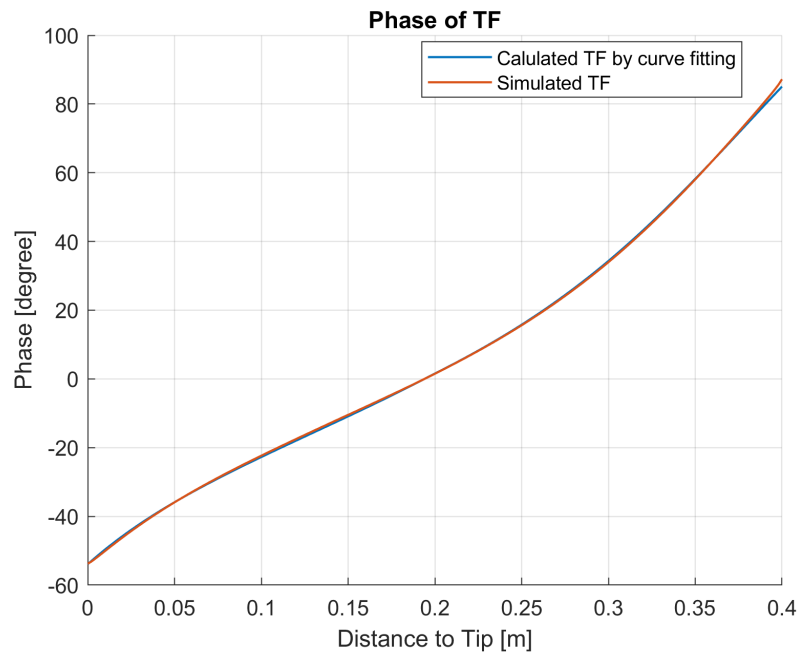
Pathway	$k_z$	$\Gamma$
S	$6.92 - j1.16$	$0.17 - j0.28$
L	$6.72 - j1.05$	$0.20 - j0.25$
U	$6.76 - j1.12$	$0.19 - j0.25$

### 3.5.2 Experimental Validation

From previous simulation study, the AIMD model of the insulated solid lead changes when the pathway has bending. The solid lead used in experiment has the

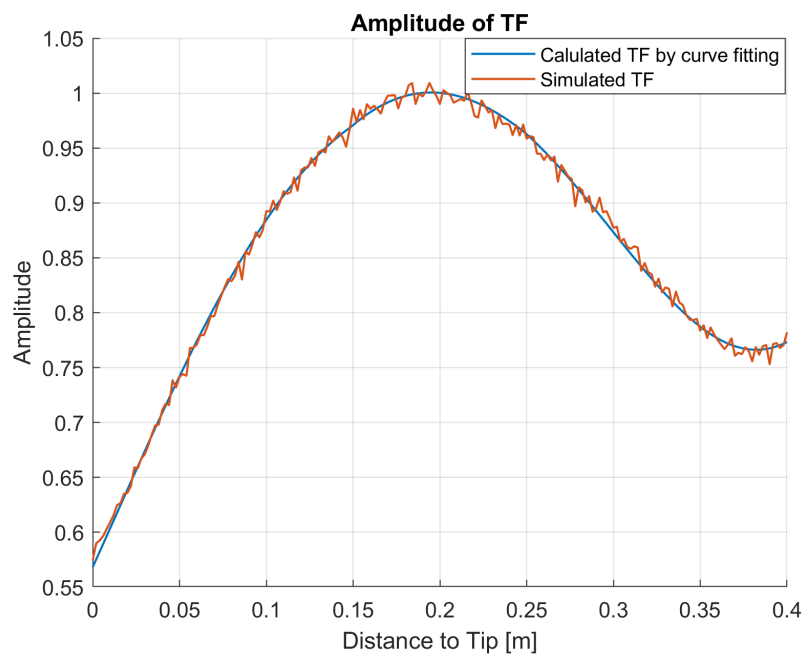


(a)

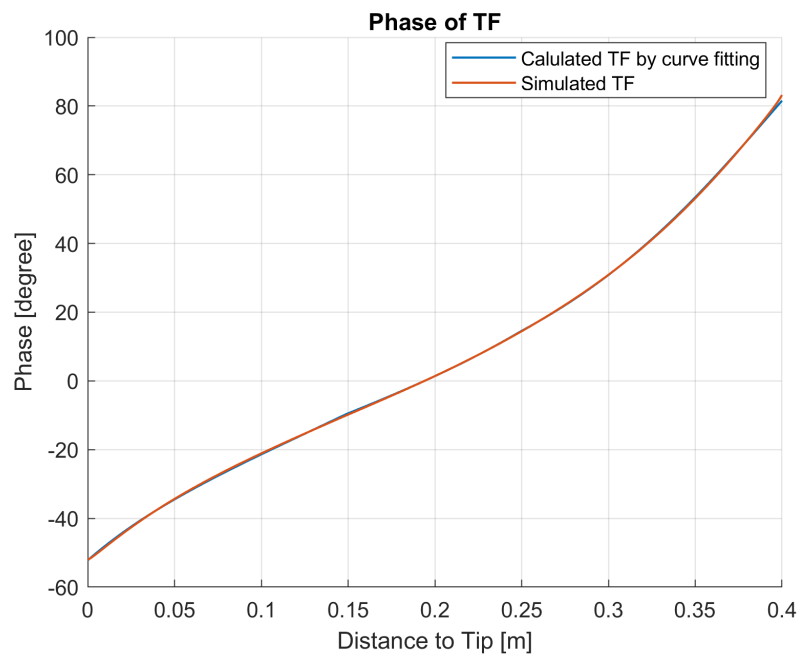


(b)

Fig. 3.24: (a) Amplitude of the AIMD model along L pathway by simulation and curve fitting; (b)Phase of the AIMD model along L pathway by simulation and curve fitting.



(a)



(b)

Fig. 3.25: (a) Amplitude of the AIMD model along U pathway by simulation and curve fitting; (b)Phase of the AIMD model along U pathway by simulation and curve fitting.

same material and geometry as in simulation as shown in Fig. 3.26.

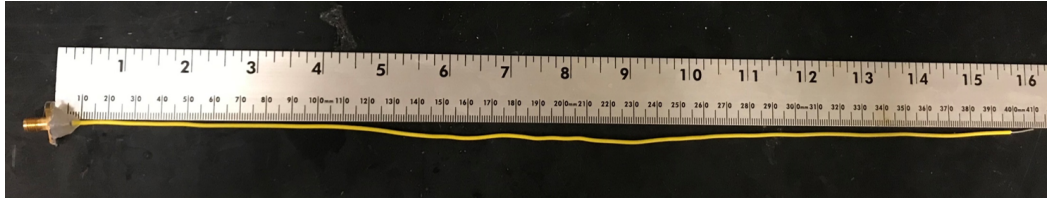
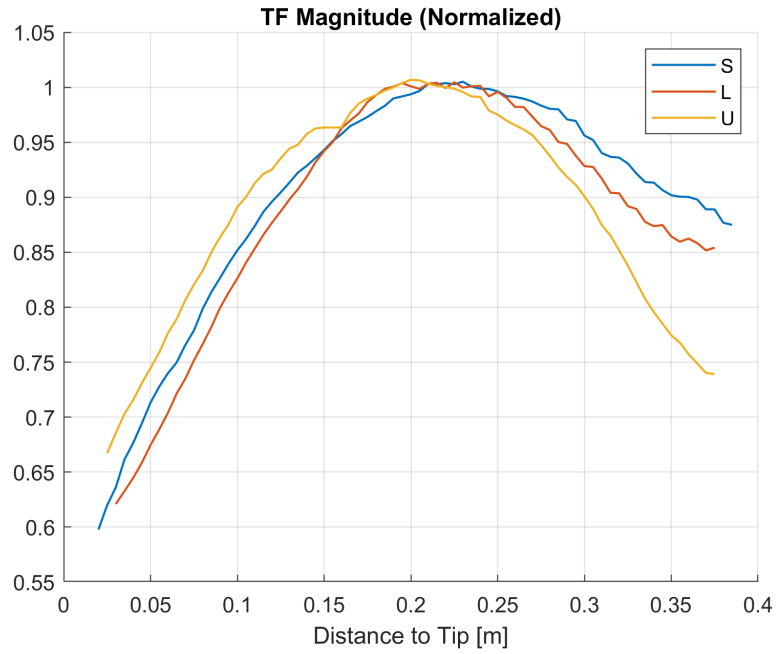


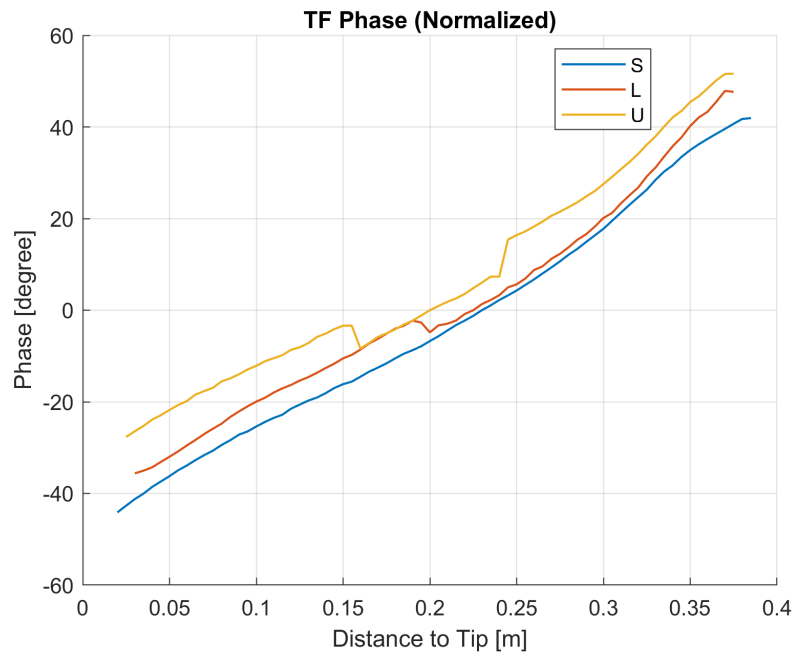
Fig. 3.26: The insulated solid lead.

The AIMD model was measured using the reciprocity method and the result was shown in Fig. 3.27. The little discontinuity for the phase of the AIMD models along L and U pathways is from the measurement method. During the measurement, the AIMD model was measured separately for each bending part. This would make the AIMD model not continuous. At the proximal end of the lead, the AIMD model changes similarly in simulation. It is validated that bending pathway will change the AIMD model of the insulated solid lead.

In order to avoid this effect, a commercial lead with helical winding structure was used. This lead has a length of 52 cm and 3 conductors. Each conductor is helical wound in parallel to others. And an insulated layer covers all conductors. Same experiments were performed to compare the AIMD models using the pathways as shown in Fig. 3.28.



(a)



(b)

Fig. 3.27: (a) Amplitude of the AIMD model for the insulated solid lead along S, L and U pathway in experiment; (b) Phase of the AIMD model for the insulated solid lead along S, L and U pathway in experiment.

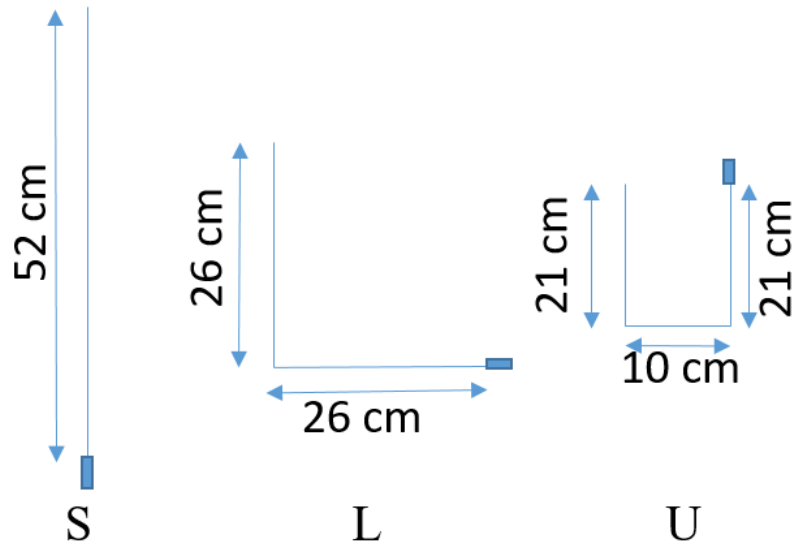
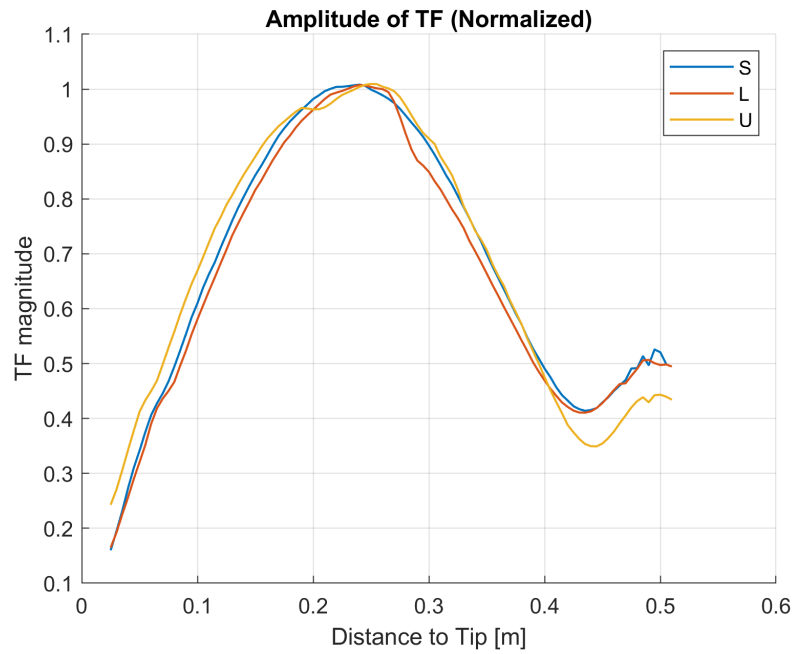


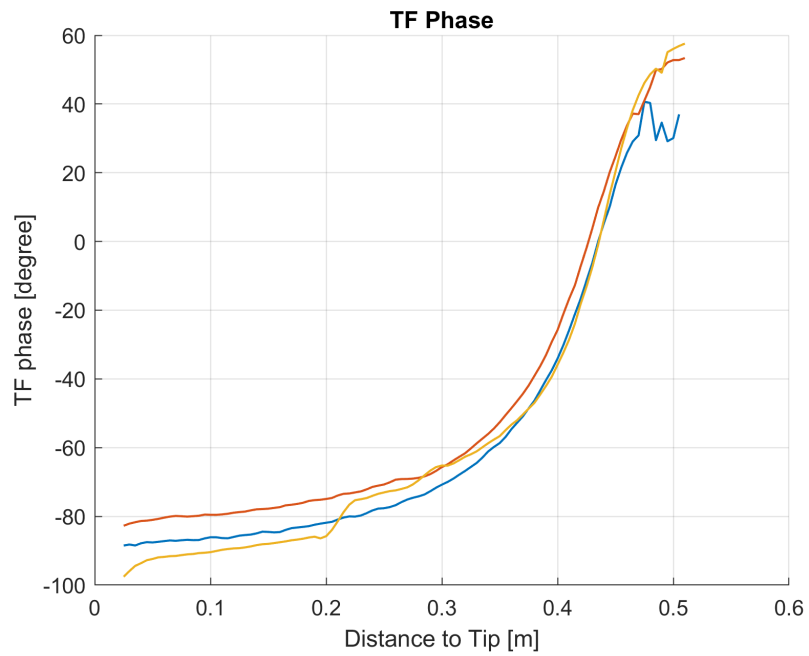
Fig. 3.28: The pathways of the insulated solid lead.

The AIMD models measured were shown in Fig. 3.29. Although the magnitude for the AIMD model along U pathway has minor difference from others, the AIMD model doesn't change as the insulated solid lead. The minor difference may come from experiment errors. As the helical winding is quite tense, the wave transmitted wouldn't reflect at the bending corner. This feature makes it possible to use same AIMD model along different pathways.

Another lead with helical winding structure was also measured. This lead has a length of 38.5 cm and 4 conductors. Same experiments were performed to compare the AIMD models using the pathways as shown in Fig. 3.30.



(a)



(b)

Fig. 3.29: (a) Amplitude of the AIMD model for the helical winding lead along S, L and U pathway in experiment; (b) Phase of the AIMD model for the helical winding lead along S, L and U pathway in experiment.

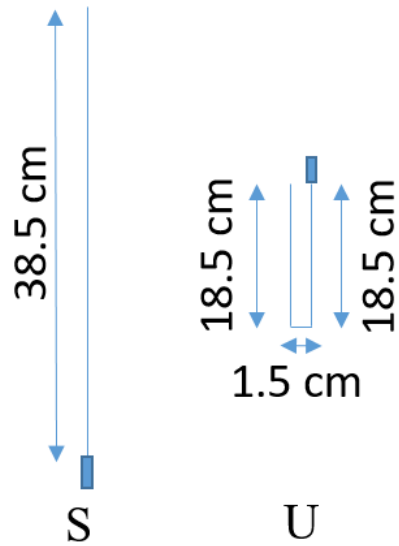
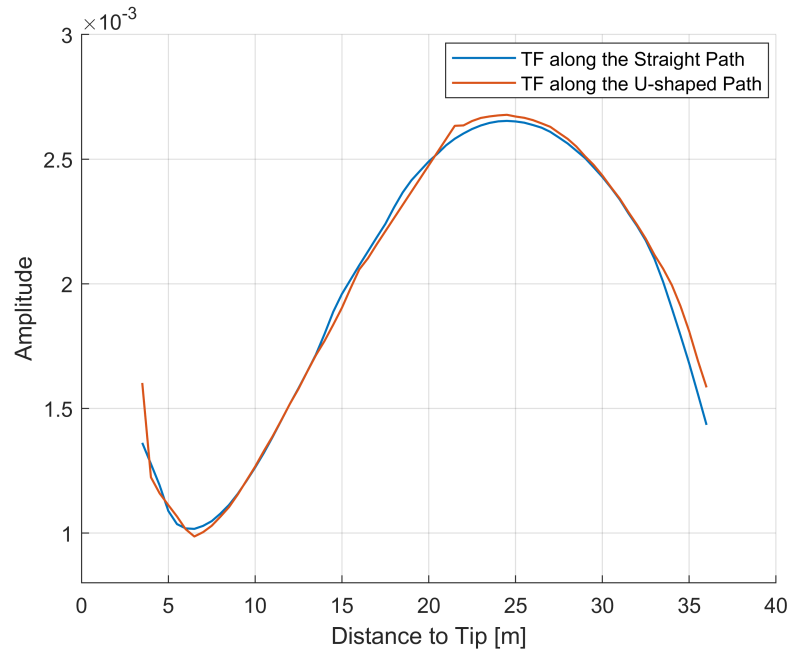
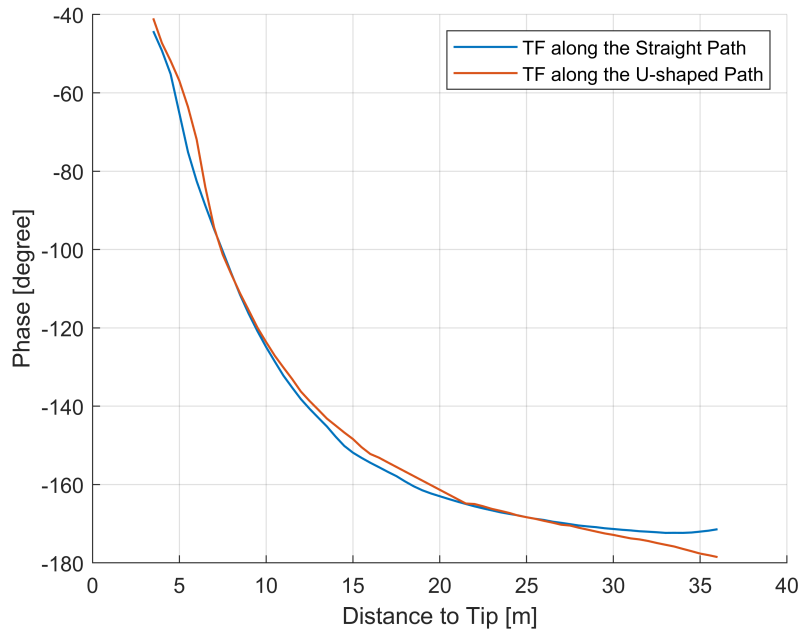


Fig. 3.30: The pathways of the insulated solid lead.

The AIMD models measured were shown in Fig. 3.31. The minor difference between two AIMD models came from the experiment setup. The two AIMD models agree with each other well. And the bending pathway doesn't affect the AIMD model.



(a)



(b)

Fig. 3.31: (a) Amplitude of the AIMD model for the helical winding lead along S and U pathway in experiment; (b) Phase of the AIMD model for the helical winding lead along S and U pathway in experiment.

## 3.6 The AIMD Model Mode Discussion

Although the AIMD model can be inverted using the transmission line model, it is based on that there is only one main mode for the transmission. In this part, the possibility of multi-mode model was discussed.

### 3.6.1 The Fourier Transform of the AIMD Model

Supposing the AIMD model of an insulated solid lead is made up with several TM modes, the Fourier transform of the AIMD model should detect these modes as long as the spatial sample size is small enough and spatial length is long enough. According to the Nyquist Sampling Theory, the Nyquist frequency is half of the sampling frequency which is cut-off frequency that one can detect through the sampling. Corresponding to the Fourier transform of the AIMD model, it is the cut-off value of  $k_z$ . And the spatial sampling distance determines the resolution of  $k_z$  that one can detect. Suppose the AIMD model is made up with

$$TF = \sum_{n=0}^M C_1^{(n)} e^{-jk_{zn}z} + C_2^{(n)} e^{jk_{zn}z}, \quad (3.32)$$

where  $C_1^{(n)}$  and  $C_2^{(n)}$  are the constant for the  $n_{th}$  mode, and  $k_{zn}$  are the wave number of the the  $n_{th}$  mode. And its Fourier transform is

$$\mathcal{F}\{TF\} = \sum_{n=0}^M B_n \delta(k_z - k_{zn}). \quad (3.33)$$

Ideally all modes in transfer function should be detected. Practically, the AIMD model is measured discretely and the length of the AIMD model is limited. Hence the sample size and spatial sample length are critical to recognize different modes.

To detect  $\Delta k_z$  difference between modes in the DFT, the length of the AIMD model should meet

$$\frac{1}{d} \leq \frac{\Delta k_z}{2\pi}, \quad (3.34)$$

which is also

$$d \geq \frac{2\pi}{\Delta k_z}, \quad (3.35)$$

where  $d$  is the length of the AIMD model. To detect  $k_z$  for a certain mode in the AIMD model, the sample size of the AIMD model should meet

$$\frac{1}{2\Delta d} \geq \frac{k_z}{2\pi}, \quad (3.36)$$

which is also

$$\Delta d \leq \frac{\pi}{k_z}, \quad (3.37)$$

where  $\Delta d$  is the sample size of the AIMD model. Hence the sample size and sample length are determined by  $k_z$  of the AIMD model.

### 3.6.2 Numerical Study

For an insulated solid lead (XTRA GUARD alpha 1563) with an inner conductor of a 0.4 mm radius and an outer coating of a 0.8 mm radius and a relative permittivity of 3.0 in saline with a relative permittivity of 78 and a conductivity of 0.47 S/m, the potential fields of the AIMD model for the  $n^{th}$  mode can be calculated by

$$A_{z1} = e^{-jk_z z} [J_n(k_{\rho 1}\rho) + AY_n(k_{\rho 1}\rho)] \quad (3.38)$$

and

$$A_{z2} = e^{-jk_z z} [BH_n^{(2)}(k_{\rho 2}\rho)], \quad (3.39)$$

where  $J_n$ ,  $Y_n$  and  $H_n^{(2)}$  are the Bessel functions of the  $n^{th}$  order. Similarly to the previous part, constant  $A$  can be got from the electric boundary condition at the radius  $a$ , we have

$$E_{z1} = 0 \quad @\rho = a, \quad (3.40)$$

which is also

$$\frac{k_{\rho 1}}{j\omega\mu\varepsilon_1} e^{-jk_z z} [J_n(k_{\rho 1}a) + AY_n(k_{\rho 1}a)] = 0. \quad (3.41)$$

Then the constant  $A$  is

$$A = -\frac{J_n(k_{\rho 1}a)}{Y_n(k_{\rho 1}a)}. \quad (3.42)$$

To make it simple,

$$A_{z1} = e^{-jk_z z} [Y_n(k_{\rho 1}a) J_n(k_{\rho 1}\rho) - J_n(k_{\rho 1}a) Y_n(k_{\rho 1}\rho)] \quad (3.43)$$

According to the electric field boundary condition at the radius of  $b$ , we have

$$E_{z1} = E_{z2} \quad @\rho = b, \quad (3.44)$$

which is also

$$\frac{k_{\rho 1}^2}{j\omega\mu\varepsilon_1} e^{-jk_z z} [Y_n(k_{\rho 1}a) J_n(k_{\rho 1}b) - J_n(k_{\rho 1}a) Y_n(k_{\rho 1}b)] = \frac{k_{\rho 2}^2}{j\omega\mu\varepsilon_2} e^{-jk_z z} B H_n^{(2)}(k_{\rho 2}b). \quad (3.45)$$

Then the constant  $B$  is

$$B = \frac{\varepsilon_2 k_{\rho 1}^2 Y_n(k_{\rho 1}a) J_n(k_{\rho 1}b) - J_n(k_{\rho 1}a) Y_n(k_{\rho 1}b)}{\varepsilon_1 k_{\rho 2}^2 H_n^{(2)}(k_{\rho 2}b)}. \quad (3.46)$$

According to the magnetic field boundary condition at the radius of  $b$ , we have

$$H_{\phi 1} = H_{\phi 2} \quad @\rho = b, \quad (3.47)$$

which is also

$$\frac{-k_{\rho 1}}{\mu_1} e^{-jk_z z} [Y_n(k_{\rho 1} a) J_n'(k_{\rho 1} b) - J_n(k_{\rho 1} a) Y_n'(k_{\rho 1} b)] = \frac{-k_{\rho 2}}{\mu_2} e^{-jk_z z} B H_n^{(2)'}(k_{\rho 2} b). \quad (3.48)$$

Still,  $k_z$  can be solved numerically as shown in Table 3.

Table 3: The Wave Number of Different Orders at Different Frequencies.

Freq(MHz)\Order	0	1	2
64	6.90 - j1.04	4.33 - j0.08	3.89 - j0.05
128	12.73 - j2.05	8.54 - j0.18	7.70 - j0.11
200	19.00 - j3.05	13.25 - j0.23	11.97 - 0.14
300	27.47 - j4.46	19.81 - j0.28	17.90 - j0.16
400	35.70 - j5.98	26.38 - j0.32	23.84 - j0.17

As the order increases,  $k_\rho$  will increase which will also cause  $k_z$  decrease. According to the  $k_z$  results, the result of the Fourier transform will accumulate in the area of small values. This will make it hard to detect different mode for the AIMD model. Usually  $\Delta d$  is 0.01 m or 0.005 m and this meets the need to detect the modes in this table. And the length of the AIMD model is usually smaller than 1 m due to the physical lead length. However, the resolution requirement here is 0.44 for  $k_z$  at the 64 MHz, which requires the length to be 14.28 m. Hence, it may be impossible to distinguish the modes in the transmission line by this method.

### 3.7 Discussion

Based on the transmission line model, the AIMD models can be developed through direct heating or voltage measurements inside the ASTM phantom. To ensure the accuracy of the model development, the condition number of the tangential components of the incident fields along these selected pathways should be as small as possible. Experiments were performed to validate the proposed method. It is shown that the AIMD models developed by this approach are accurate as compared to the models developed using the conventional approach. Further, this method does not require extra test equipment to measure the shape of the AIMD model, which makes this approach more efficient, and the disturbance involved by the test equipment can be eliminated. Experiments about optical fiber effects and bending effects were performed. Optical fiber has minimum effects on the AIMD model during tests. And the bending for different pathways affect insulated solid leads but not helical winding leads. The leads with helical winding can keep the wave continuous at the bending as the helical winding can bear more shape change. Unfortunately, it is impossible to detect whether there is higher order mode in the AIMD model. According to the Nyquist Sampling Theorem, the lead length is not enough to do so usually. The uncertainty of the inversion and validation tests is 17.78%. It includes the uncertainty of the numerical modeling and experiment uncertainty.

## 4 Optimized Design based on the AIMD Model

Since the AIMD model can be taken as a transmission line model, it is possible to design optimized validation pathway or change the AIMD model to decrease the induced voltage/heating.

### 4.1 Optimized Validation Pathways

According to ISO 10974 standard, the AIMD model developed needs validation before it can be used for estimation of induced voltage/heating in human body. From previous section, the induced voltage/heating along the orthogonal validation pathways is low over half of them. One problem during the experiments is that low induced voltage/heating brings high errors and low signal noise ratio (SNR). And z shape validation pathway was proposed to induce high induced voltage/heating so that the SNR is low. However, the z shape validation pathway may not induce high voltage/heating for other AIMD models. If the electric field in phantom is given and the AIMD model is also given, it is possible to design optimized validation pathways to make the induced voltage/heating high along these pathways. Another problem is that folded validation pathways are not quite usual in clinical pathways. Although in **Clinical pathway**, the folded pathways were used as shown in Fig. 4.1. Circular pathways occur more as leads are usually longer than clinical pathways needed. Extra length of leads form the circular pathways. In total, the ideal validation pathways should meet three conditions: 1) make the condition number of the tangential component of the incident field small; 2) close to the clinical pathways; 3) induce high voltage/heating to make the SNR high during experiments.

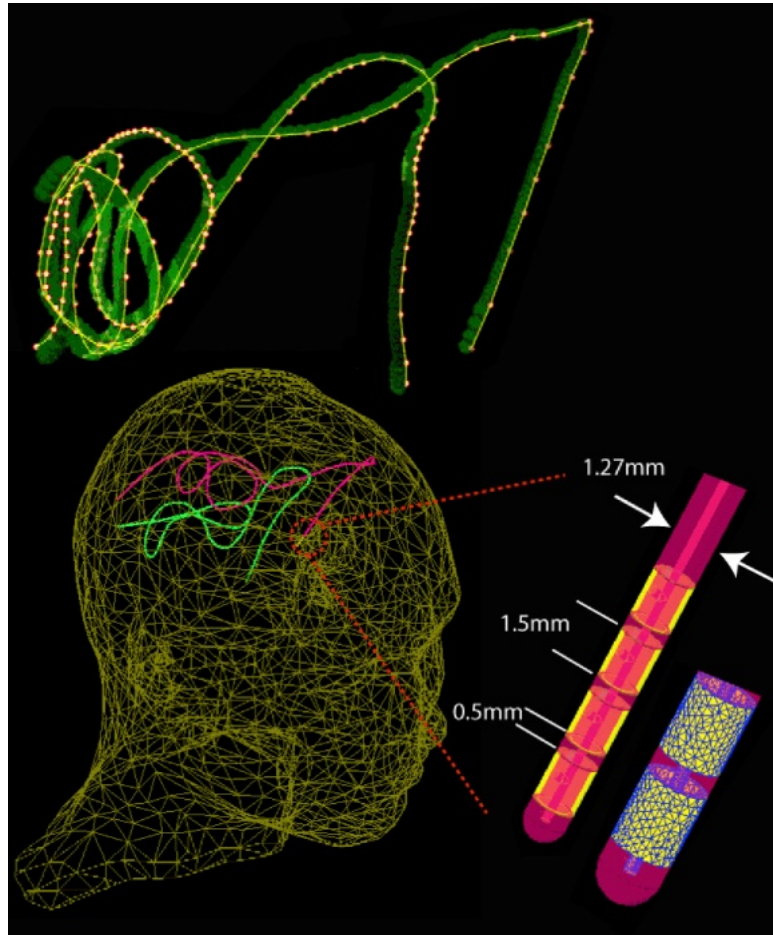


Fig. 4.1: The clinical pathway used in the deep brain stimulation.

## 4.2 Numerical Study

For simplicity, the electric field used for optimized pathways is taken as homogeneous fields, i.e., the electric field has the same strength and phase in the designed area. Induced voltage example is used here and the design for the induced heating is

the similar. Still, the induced voltage can be calculated by

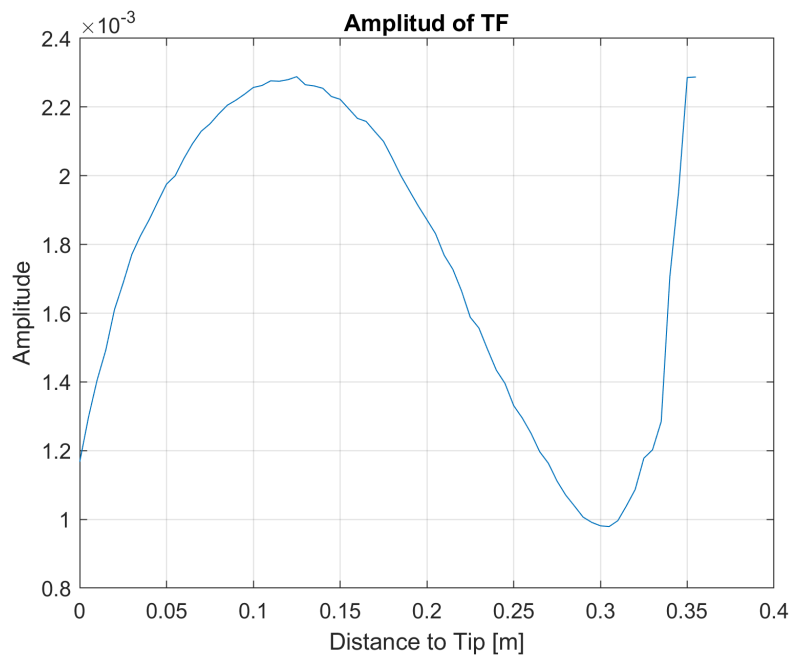
$$\begin{aligned}
 V_{ind} &= \int_L \vec{E}_{inc} \cdot TF d\hat{l} \\
 &= \int_L E_{tan} \times TF dl.
 \end{aligned} \tag{4.1}$$

Although the electric field in phantom is taken as homogeneous, the tangential components of the incident field can vary a lot by changing lead pathways. Considering pathways in the direction of the electric field or perpendicular to the electric field, the tangential components of the incident field can be 1, -1 and 0 if the magnitude of the electric field is taken as 1 V/m. Diving the AIMD model equally into eight parts, the tangential components can be also divided into eight parts which are made up with 1, -1 and 0. As the AIMD model is measured in discrete form, the total number of the measured points is not exactly divisible by 8. Zeros can be added at the end of the AIMD model to make it divisible by 8. During the validation experiment, the added length using zeros should be considered for pathways. The number of divided part can be other than eight. Eight can make the length of each part 4-6 cm as the lead length is during 30 cm to 45 cm usually. The induced voltage can be calculated by

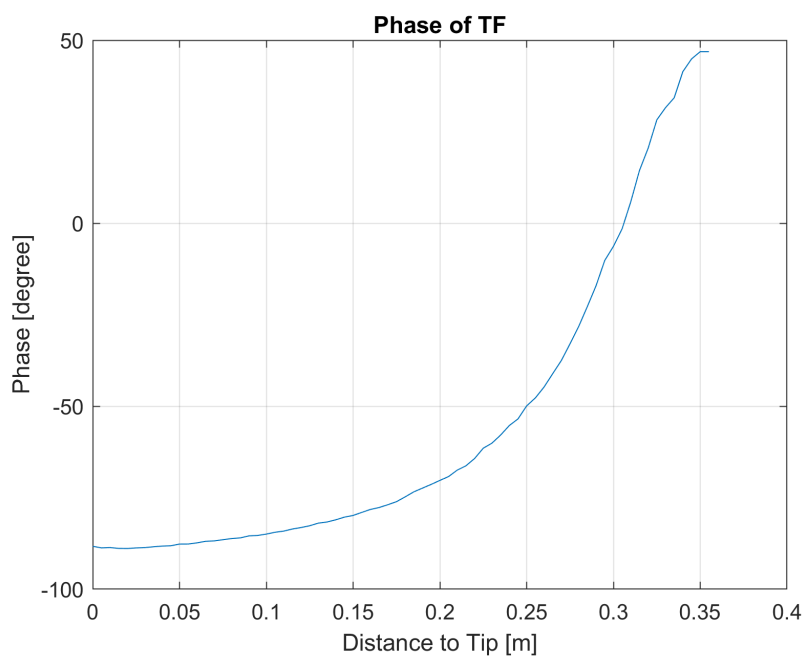
$$\begin{aligned}
 V_{ind} &\approx \Delta l \sum_{i=1}^N E_{tan}(i) \times TF(i) \\
 &\approx \Delta l \sum_{j=1}^8 E_{tan}(j) \times TF_j(j),
 \end{aligned} \tag{4.2}$$

where  $TF_j$  is the summation of the AIMD model for each part. As the tangential components of the incident field in each part is the same, the  $E_{tan}$  can be represented using one value in each part. Besides, the tangential components for the near parts can not be 1 and -1 at the same time, which makes the pathway bend 180°. The

remaining process is to find several orthogonal pathways which induce high voltage. The total number of the pathways is limited and it is easy to calculate the induced voltage for all pathways. However, the pathways that induced high voltage for a given AIMD model are quite similar as the peak position of the given AIMD model determines the induced voltage mainly. This will make the condition number of  $E_{tan}$  high. Several levels of induced voltages were chosen to make the validation pathway orthogonal. The AIMD model is taken as an example as shown in Fig. 4.2. For other AIMD models, the design process is the same. The statistic result for the induced voltage along all possible pathways is given in Fig. 4.3. The validation pathways were divided into six groups by the values of the induced voltages. Also, six groups are not necessary and six validation pathways were just as an example here. Pick one pathway from each group and find the smallest condition number for all the possible combination. The all possible combination for the six groups is quite large and it is time consuming to calculate the condition number. In order to have high efficiency, pick one pathway each time from one group and calculate the correlation for them. Pick the lowest correlation for the combination from two groups and find the next pathway from next group to make the correlation lowest.



(a)



(b)

Fig. 4.2: (a) Amplitude of the AIMD model for the optimized validation pathways; (b) Phase of the AIMD model for the optimized validation pathways.

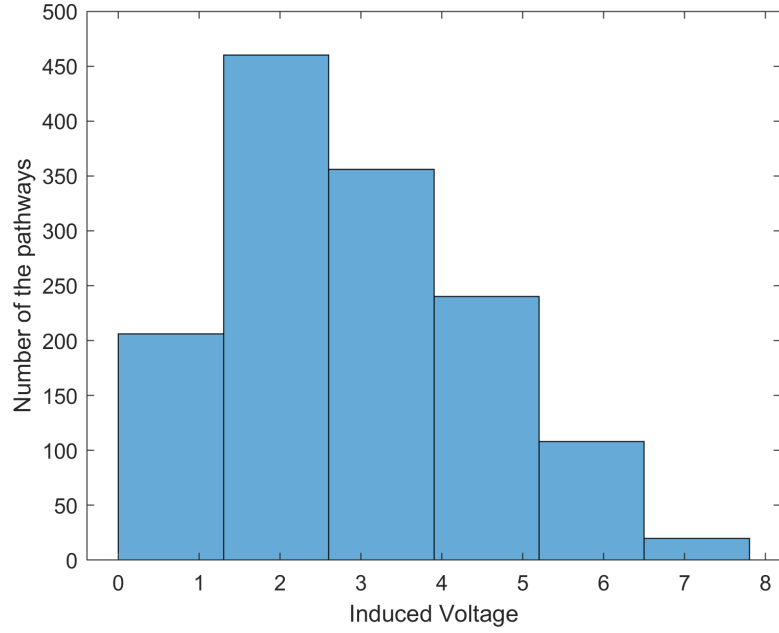


Fig. 4.3: The statistic result for all possible pathways.

The validation pathways calculated is given by

$$S_6 = \begin{bmatrix} 0 & -1 & 0 & 0 & 0 & 0 & 0 & -1 \\ 1 & 0 & 1 & -1 & -1 & 0 & 0 & 0 \\ 0 & 1 & 1 & 1 & 1 & 0 & -1 & 0 \\ 1 & 0 & -1 & 0 & 0 & -1 & -1 & 0 \\ -1 & -1 & 0 & -1 & -1 & -1 & -1 & 0 \\ 1 & 1 & 0 & -1 & -1 & -1 & -1 & -1 \end{bmatrix} \quad \kappa(S_6) = 3.15. \quad (4.3)$$

The condition number for this group is 3.15 and the induced voltages are from each group to make the SNR high. Next, it is to find the corresponding pathways in phantom. The designed pathway is shown as Fig. 4.4.

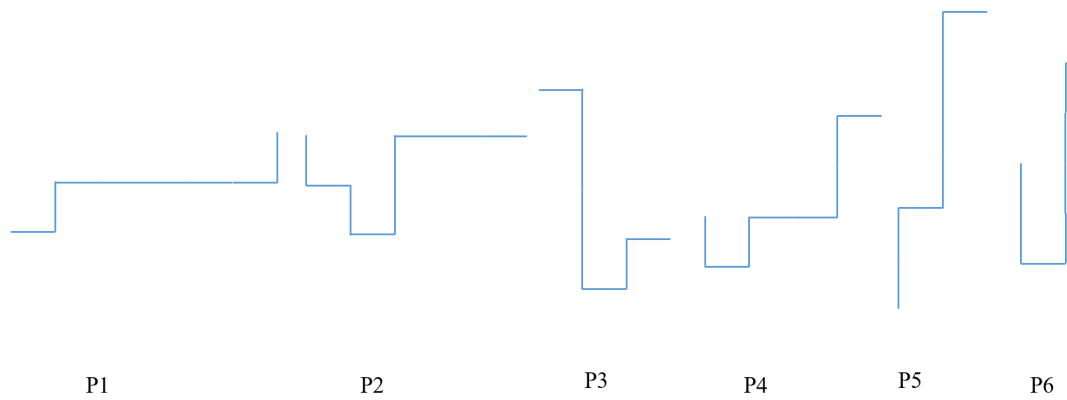


Fig. 4.4: The optimized validation pathways.

As the electric field in the ASTM phantom varies a lot as shown in Fig. 4.5, it is not easy to find a designed pathway in the ASTM phantom. The more homogeneous the electric field is, the easier it is to find the corresponding pathways.

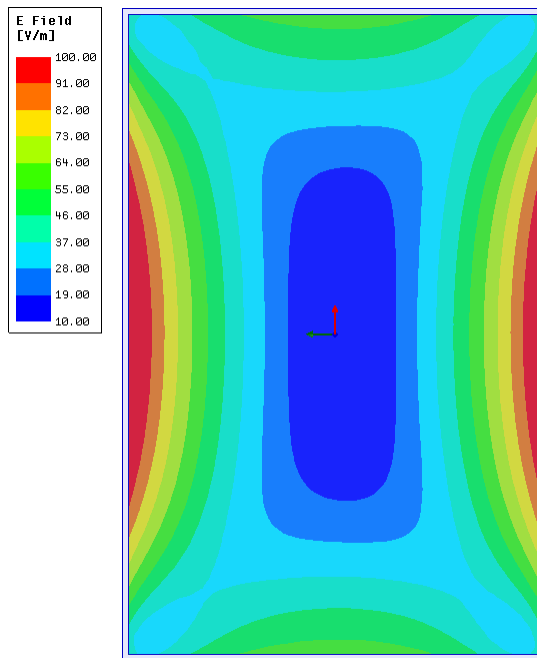


Fig. 4.5: The simulated electric field in the ASTM phantom.

Another setup was used here to find the corresponding pathways as shown in Fig.

4.6 [43]. It is a high electric field generator that resonance at 64 MHz. As shown in Fig. 4.6, the signal generator, the power amplifier, the four-way Wilkinson power divider with pre-matching circuits, and the resonator constitute the high electric field generating system. The sine wave coming from the signal generator is amplified by a power amplifier with gain of 50 dB. The matching circuit consisting of lumped elements adjusts the impedance seen by the input of the power divider to  $50 \Omega$ . It consists of two separate sets of circuitry for each frequency. The high power signal is divided into four ways with identical phase and magnitude. The special four-way feeding network is achieved by exciting the front ( $(\pm z)$ ) and back ( $-z$ ) walls respectively of the cavity as shown in Fig. 4.6 below. With the boundary condition of a PEC on the surrounding four planes ( $\pm x$ ) and ( $\pm z$ ) and a PMC on the gel-air interface ( $\pm y$ ), the resonator supports the TE<sub>10</sub> mode at 64 MHz.

The simulated electric field is shown in Fig. 4.7. Compared to the electric field in ASTM phantom, the electric field in the box is more homogeneous. It will be more appropriate to find the designed pathways. The direction of electric field in the box is mainly from up to down. The tangential components of the incident field are shown in Fig. 4.8. The reason why the phase of pathway 1 and 2 is not stable is that the amplitude of them is close to zero. Specially, the condition number of  $E_{tan}$  is 3.57, which is close to the designed one. And the induced voltage amplitude ratio is given in Table 4 as the amplitude is more significant during experiments. The optimized validation pathways can validate the AIMD model sufficiently and have a high SNR during experiments.

Still, the circular pathways were not considered here as it is impossible to make sure the induced voltage high using the designed process mentioned. A possible validation pathway was given next. As validation pathways need to be circular, the

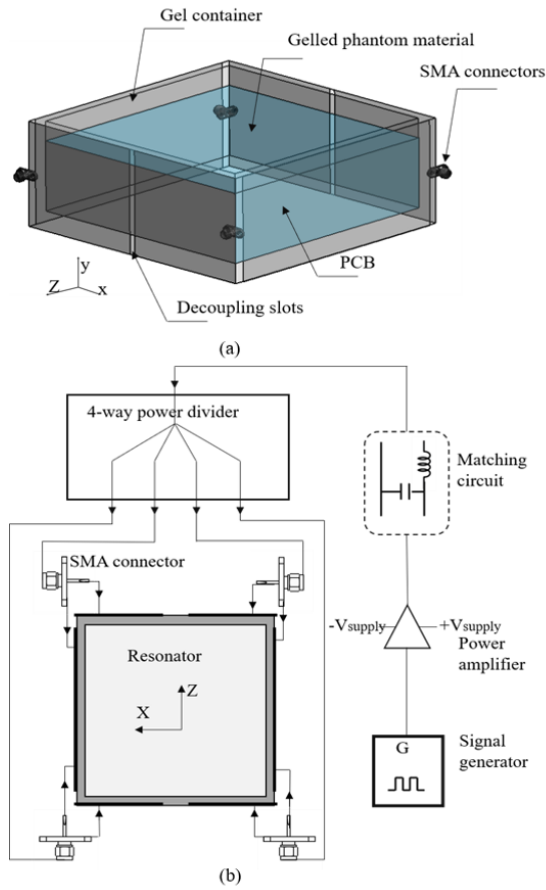


Fig. 4.6: The high electric field generating system. (a) The resonator structure; (b) The whole system constitution.

Table 4: The Induced Voltage Ratio of the Optimized Validation Pathways.

Pathway Index	Induced Voltage Amplitude Ratio
1	0.72
2	1.70
3	1.60
4	2.27
5	2.84
6	3.56

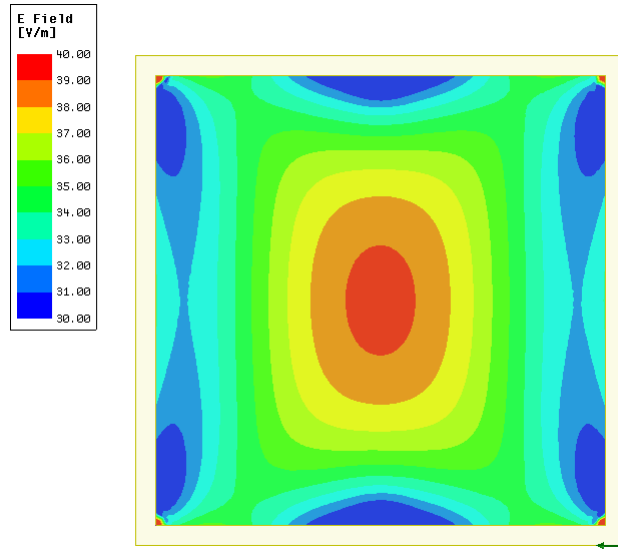
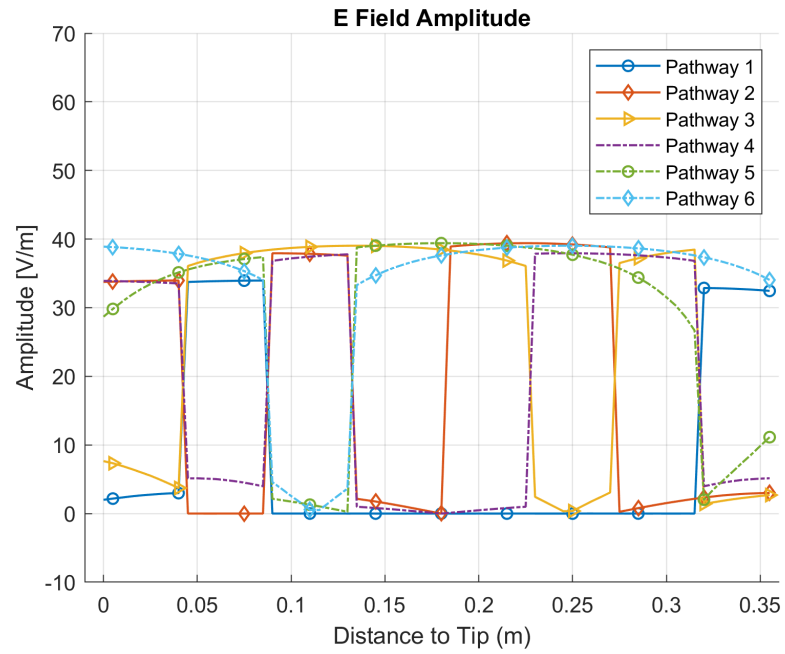
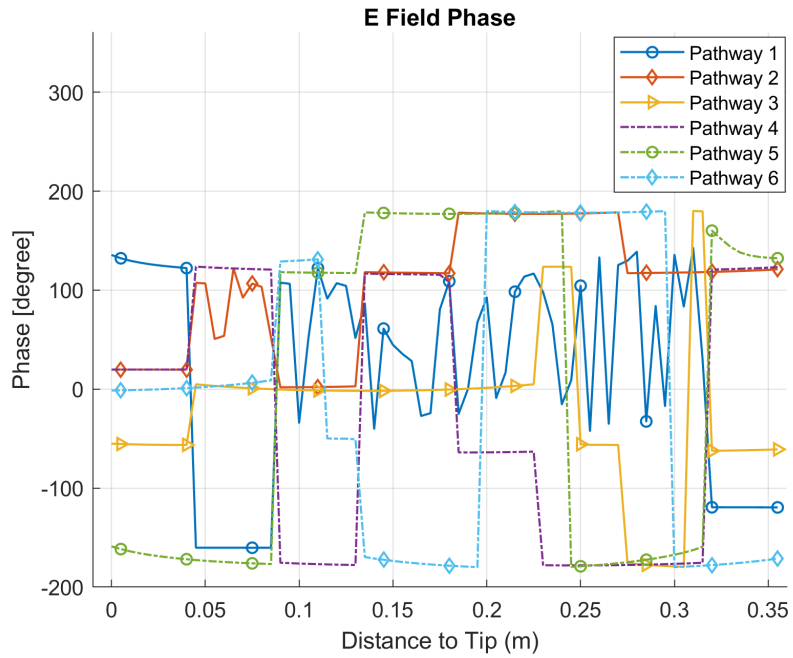


Fig. 4.7: The simulated electric field in the box.

radius of the circle and loops of the circle are the two main factors that can be changed except the location of the validation pathways. Under a homogeneous electric field, the tangential components of the incident field along circular pathways behave as the sine function or the cosine function. It will be easy for pathways to be orthogonal as sine and cosine functions are orthogonal to each other. The circular pathways are as shown in Fig. 4.9 which are composed of half circle, one circle, two circles and three circles. It is found that the tangential components of the half circle are also orthogonal to others. The tangential components of the incident fields are shown in Fig. 4.10. The peak value of all the tangential components are similar and the total time period for each validation pathway is corresponding to the total number of the circles. The condition number of these circular validation pathways is 5.10. However, the induced voltage/heating along these pathways can not ensure to be high. Still, these validation pathways are close to suggested clinical validation pathways.



(a)



(b)

Fig. 4.8: (a) Amplitude of the tangential components of the simulated incident field for the optimized validation pathways; (b) Phase of the tangential components of the simulated incident field for the optimized validation pathways.

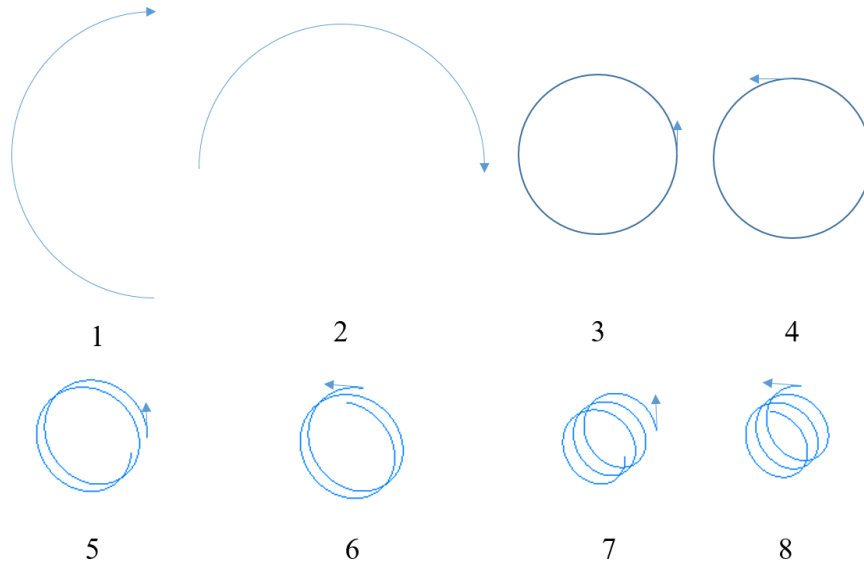
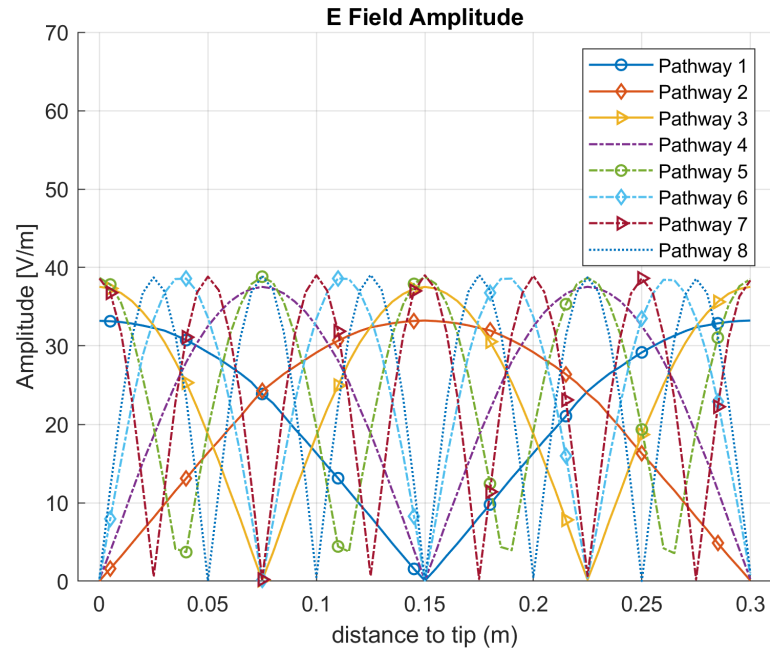


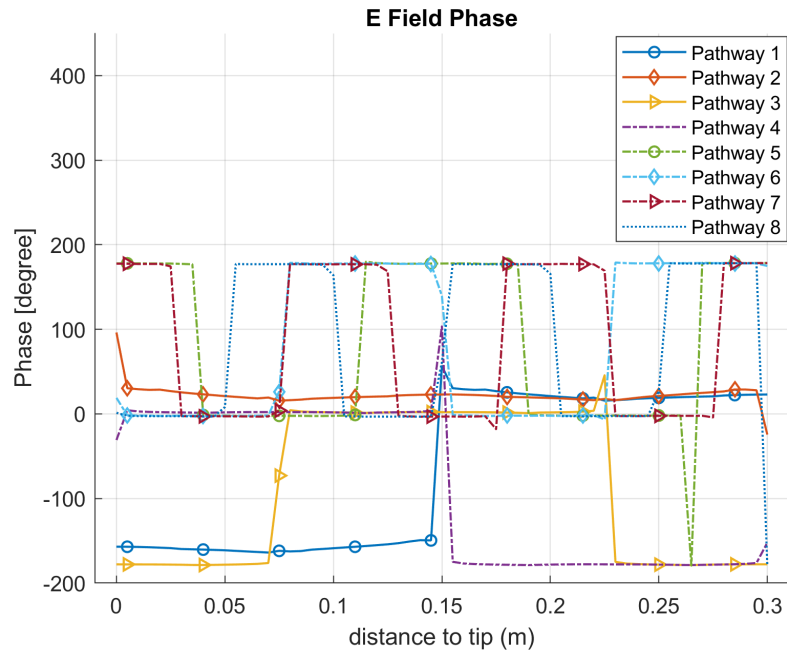
Fig. 4.9: The circular validation pathways.

### 4.3 Discussion

Folded validation pathways and circular validation pathways were proposed to validate the AIMD model. In order to validate the AIMD model sufficiently, the condition number of  $E_{tan}$  should be as small as possible. Both sets of the validation pathways meet this requirements. Optimized validation pathways were designed according to the AIMD model. By increasing the induced voltage/heating of the validation pathways for the leads, the SNR can be high to make sure the accuracy of the experiments. However, this kind of validation pathways is not close to clinical pathways. Circular validation pathways were proposed to meet this. Also, it is a trade-off to the high induced voltage/heating. By using the high E field generator, designed pathways can be better accomplished. The uncertainty of optimized design is 9.86%. Still this is based on the numerical modeling. The uncertainty includes the uncertainty of pathway shift and material property.



(a)



(b)

Fig. 4.10: (a) Amplitude of the tangential components of the simulated incident field for the circular validation pathways; (b) Phase of the tangential components of the simulated incident field for the circular validation pathways.

## 5 Conclusions

In conclusion, the standard validation pathways in ISO 10974 were discussed in chapter 2. It was found that two spurious AIMD model could be validated using these pathways. Through eigenvalue decomposition, the tangential components of the incident field along the standard validation pathways were highly correlated, which makes the validation not sufficient. For accuracy and sufficiency, two sets of validation pathways based on the Hadamard matrix were designed. These validation pathways can distinguish the difference of the AIMD model to have a sufficient validation. The key point of the validation pathways is the condition number of the tangential components of the incident fields. Low condition number can make sure each validation pathway sufficient and independent. In chapter 3, based on the proposed validation pathways, the AIMD model can be inverted efficiently. The low condition number of the tangential components of the incident fields makes the inverse problem well-conditioned. Specially, the error of inverting the AIMD model is bounded by the condition number and the error of the induced voltage/heating. In chapter 4, an optimized validation pathway design in a high electric generator were proposed to perform good validation. The optimized validation pathways based on a given AIMD model can give a high SNR and sufficient validation. Also, a set of circular validation pathways were designed to be related to the clinical pathways in simulation.

## References

- [1] “Magnetic Resonance Imaging (MRI) Exams,” Organization for Economic Co-operation and Development, Paris, France, Tech. Rep., 2019. [Online]. Available: <http://dx.doi.org/10.1787/1d89353f-en>.
- [2] E. Kanal, A. Barkovich, C. Bell, J. Borgstede, W. Bradley, J. Froelich, T. Gilk, J. Gimbel, and E. K.-K. J. Gosbee, “ACR Guidance Document for Safe MR Practices: 2007,” *American Journal of Roentgenology*, vol. 188, no. 6, pp. 1447–1474, 2007.
- [3] F. G. Shellock, T. O. Woods, and J. V. Crues III, *MR Labeling Information for Implants and Devices: Explanation of Terminology*, 2009.
- [4] S. Sohn, L. Delabarre, A. Gopinath, and J. T. Vaughan, “RF Head Coil Design with Improved RF Magnetic Near-Fields Uniformity for Magnetic Resonance Imaging (MRI) Systems,” *IEEE Transactions on Microwave Theory and Techniques*, vol. 62, no. 8, pp. 1784–1789, 2014.
- [5] I. A. Elabyad, T. Herrmann, C. Bruns, J. Bernarding, and D. Erni, “RF Shimming and Improved SAR Safety for MRI at 7 T With Combined Eight-Element Stepped Impedance Resonators and Traveling-Wave Antenna,” *IEEE Transactions on Microwave Theory and Techniques*, vol. 66, no. 1, pp. 540–555, Jan. 2018, ISSN: 1557-9670.

- [6] P. Bluem, P. Van de Moortele, G. Adriany, and Z. Popović, “Excitation and RF Field Control of a Human-Size 10.5-T MRI System,” *IEEE Transactions on Microwave Theory and Techniques*, vol. 67, no. 3, pp. 1184–1196, Mar. 2019, ISSN: 1557-9670. DOI: 10.1109/TMTT.2018.2884405.
- [7] A. Kordzadeh and N. De Zanche, “Control of Mutual Coupling in High-Field MRI Transmit Arrays in the Presence of High-Permittivity Liners,” *IEEE Transactions on Microwave Theory and Techniques*, vol. 65, no. 9, pp. 3485–3491, Sep. 2017, ISSN: 1557-9670.
- [8] K. Byron, S. A. Winkler, F. Robb, S. Vasanaawala, J. Pauly, and G. Scott, “An MRI Compatible RF MEMs Controlled Wireless Power Transfer System,” *IEEE Transactions on Microwave Theory and Techniques*, vol. 67, no. 5, pp. 1717–1726, May 2019, ISSN: 1557-9670.
- [9] S. X. Xin, Q. Huang, Y. Gao, B. Li, Y. Xu, and W. Chen, “Fetus MRI at 7 T: B1 Shimming Strategy and SAR Safety Implications,” *IEEE Transactions on Microwave Theory and Techniques*, vol. 61, no. 5, pp. 2146–2152, May 2013, ISSN: 1557-9670. DOI: 10.1109/TMTT.2013.2247053.
- [10] F. Gao, F. Zhang, H. Wakatsuchi, and D. F. Sievenpiper, “Synthesis and Design of Programmable Subwavelength Coil Array for Near-Field Manipulation,” *IEEE Transactions on Microwave Theory and Techniques*, vol. 63, no. 9, pp. 2971–2982, Sep. 2015, ISSN: 1557-9670. DOI: 10.1109/TMTT.2015.2450711.

- [11] Z. Chen, K. Solbach, D. Erni, and A. Rennings, “Improving B1 Efficiency and Signal-to-Noise-Ratio of a Surface Coil by a High-Impedance-Surface RF Shield for 7-T Magnetic Resonance Imaging,” *IEEE Transactions on Microwave Theory and Techniques*, vol. 65, no. 3, pp. 988–997, Mar. 2017, ISSN: 1557-9670. DOI: 10.1109/TMTT.2016.2631169.
- [12] I. A. Elabyad, M. Terekhov, M. R. Stefanescu, D. Lohr, M. Fischer, and L. M. Schreiber, “Design and Evaluation of a Novel Symmetric Multichannel Transmit/Receive Coil Array for Cardiac MRI in Pigs at 7 T,” *IEEE Transactions on Microwave Theory and Techniques*, vol. 67, no. 9, pp. 3928–3945, Sep. 2019, ISSN: 1557-9670. DOI: 10.1109/TMTT.2019.2913636.
- [13] T. Kawamura, K. Saito, S. Kikuchi, M. Takahashi, and K. Ito, “Specific Absorption Rate Measurement of Birdcage Coil for 3.0-T Magnetic Resonance Imaging System Employing Thermographic Method,” *IEEE Transactions on Microwave Theory and Techniques*, vol. 57, no. 10, pp. 2508–2514, Oct. 2009, ISSN: 1557-9670. DOI: 10.1109/TMTT.2009.2029712.
- [14] N. P. Gandji, G. Lee, G. Semouchkin, E. Semouchkina, T. Neuberger, and M. Lanagan, “Development and Experimental Testing of Microstrip Patch Antenna-Inspired RF Probes for 14 T MRI Scanners,” *IEEE Transactions on Microwave Theory and Techniques*, vol. 67, no. 1, pp. 443–453, Jan. 2019, ISSN: 1557-9670. DOI: 10.1109/TMTT.2018.2874266.

- [15] M. Fiek, T. Remp, C. Reithmann, and G. Steinbeck, “Complete Loss of ICD Programmability after Magnetic Resonance Imaging,” *Pacing and Clinical Electrophysiology*, vol. 27, no. 7, pp. 1002–1004, 2004.
- [16] J. A. Erlebacher, P. T. Cahill, F. Pannizzo, and R. J. R. Knowles, “Effect of Magnetic Resonance Imaging on DDD Pacemakers,” *The American journal of cardiology*, vol. 57, no. 6, pp. 437–440, 1986.
- [17] R. Tanaka, T. Yumoto, N. Shiba, M. Okawa, T. Yasuhara, T. Ichikawa, K. Tokunaga, I. Date, and Y. Ujike, “Overheated and Melted Intracranial Pressure Transducer as Cause of Thermal Brain Injury during Magnetic Resonance Imaging: Case Report,” *Journal of Neurosurgery*, vol. 117, no. 6, pp. 1100–1109, 2012.
- [18] J. A. Nyenhuis, S.-M. Park, R. Kamondetdacha, A. Amjad, F. G. Shellock, and A. R. Rezai, “MRI and Implanted Medical Devices: Basic Interactions with An Emphasis on Heating,” *IEEE Transactions on Device and Materials Reliability*, vol. 5, no. 3, pp. 467–480, 2005.
- [19] E. Mattei, M. Triventi, G. Calcagnini, F. Censi, W. Kainz, G. Mendoza, H. I. Bassen, and P. Bartolini, “Complexity of MRI Induced Heating on Metallic Leads: Experimental Measurements of 374 Configurations,” *Biomedical Engineering Online*, vol. 7, no. 1, p. 11, 2008.
- [20] L. Golestanirad, L. M. Angelone, J. Kirsch, S. Downs, B. Keil, G. Bonmassar, and L. L. Wald, “Reducing RF-induced Heating near Implanted Leads Through

- High-dielectric Capacitive Bleeding of Current (CBLOC),” *IEEE Transactions on Microwave Theory and Techniques*, vol. 67, no. 3, pp. 1265–1273, 2019.
- [21] S. McCabe and J. Scott, “A Novel Implant Electrode Design Safe in the RF Field of MRI Scanners,” *IEEE Transactions on Microwave Theory and Techniques*, vol. 65, no. 9, pp. 3541–3547, 2017.
- [22] P. Nordbeck, I. Weiss, P. Ehses, O. Ritter, M. Warmuth, F. Fidler, V. Herold, P. M. Jakob, M. E. Ladd, H. H. Quick, and W. R. Bauer, “Measuring RF-induced Currents Inside Implants: Impact of Device Configuration on MRI Safety of Cardiac Pacemaker Leads,” *Magnetic Resonance in Medicine: An Official Journal of the International Society for Magnetic Resonance in Medicine*, vol. 61, no. 3, pp. 570–578, 2009.
- [23] E. Mattei, G. Calcagnini, F. Censi, M. Triventi, and P. Bartolini, “Numerical Model for Estimating RF-induced Heating on a Pacemaker Implant during MRI: Experimental Validation,” *IEEE Transactions on Biomedical Engineering*, vol. 57, no. 8, pp. 2045–2052, 2010.
- [24] S.-M. Park, R. Kamondetdacha, and J. A. Nyenhuis, “Calculation of MRI-induced Heating of an Implanted Medical Lead Wire with an Electric Field Transfer Function,” *Journal of Magnetic Resonance Imaging: An Official Journal of the International Society for Magnetic Resonance in Medicine*, vol. 26, no. 5, pp. 1278–1285, 2007.

- [25] S. Feng, R. Qiang, W. Kainz, and J. Chen, “A Technique to Evaluate MRI-induced Electric Fields at the Ends of Practical Implanted Lead,” *IEEE Transactions on Microwave Theory and Techniques*, vol. 63, no. 1, pp. 305–313, 2014.
- [26] H. G. Mond and D. Grenz, “Implantable Transvenous Pacing Leads: the Shape of Things to Come,” *Pacing and clinical electrophysiology*, vol. 27, no. 6p2, pp. 887–893, 2004.
- [27] A. F2182-11a, “Standard Test Method for Measurement of Radio Frequency Induced Heating on or near Passive Implants during Magnetic Resonance Imaging,” 2014.
- [28] T. ISO, “10974: Assessment of the Safety of Magnetic Resonance Imaging for Patients with an Active Implantable Medical Device,” *Geneva, Switzerland: International Organization for Standardization*, 2018.
- [29] Q. Zeng, J. Liu, L. M. Angelone, T. Lloyd, S. Wedan, J. Chen, and W. Kainz, “Investigation of RF-induced Heating near Interventional Catheters at 1.5 T MRI: A Combined Modeling and Experimental Study,” *IEEE Transactions on Electromagnetic Compatibility*, vol. 61, no. 5, pp. 1423–1431, 2018.
- [30] Q. Zeng, Q. Wang, J. Zheng, W. Kainz, and J. Chen, “Evaluation of MRI RF Electromagnetic Field Induced Heating near Leads of Cochlear Implants,” *Physics in Medicine & Biology*, vol. 63, no. 13, p. 135020, 2018.
- [31] G. H. Golub and C. Reinsch, “Singular Value Decomposition and Least Squares Solutions,” in *Linear Algebra*, Springer, 1971, pp. 134–151.

- [32] J. Hadamard, “Resolution d’une Question Relative aux Determinants,” *Bull. des sciences math.*, vol. 2, pp. 240–246, 1893.
- [33] F. Pukelsheim, “The Three Sigma Rule,” *The American Statistician*, vol. 48, no. 2, pp. 88–91, 1994.
- [34] F. A. Graybill, *Theory and Application of the Linear Model*. Duxbury press North Scituate, MA, 1976, vol. 183.
- [35] S. Feng, Q. Wang, C. Wen, J. Zheng, W. Kainz, and J. Chen, “Simplified Transfer Function Assessment of Implantable Leads for MRI Safety Evaluations,” *IEEE Transactions on Electromagnetic Compatibility*, vol. 61, no. 5, pp. 1432–1437, 2018.
- [36] L. Golestanirad, J. Kirsch, G. Bonmassar, S. Downs, B. Elahi, A. Martin, M.-I. Iacono, L. M. Angelone, B. Keil, L. L. Wald, and J. Pilitsis, “RF-induced Heating in Tissue near Bilateral DBS Implants during MRI at 1.5 T and 3T: The Role of Surgical Lead Management,” *NeuroImage*, vol. 184, pp. 566–576, 2019.
- [37] W. C. Gibson, *The Method of Moments in Electromagnetics*. CRC press, 2014.
- [38] J. Liu, J. Zheng, Q. Wang, W. Kainz, and J. Chen, “A Transmission Line Model for the Evaluation of MRI RF-induced Fields on Active Implantable Medical Devices,” *IEEE Transactions on Microwave Theory and Techniques*, vol. 66, no. 9, pp. 4271–4281, 2018.
- [39] E. Zastrow, M. Capstick, E. Cabot, and N. Kuster, “Piece-wise Excitation System for the Characterization of Local RF-induced Heating of AIMD during MR

- Exposure,” in *2014 International Symposium on Electromagnetic Compatibility, Tokyo*, IEEE, 2014, pp. 241–244.
- [40] Z. Wang, J. Zheng, Y. Wang, W. Kainz, and J. Chen, “On the Model Validation of Active Implantable Medical Device for MRI Safety Assessment,” *IEEE Transactions on Microwave Theory and Techniques*, 2019.
- [41] G. H. Golub and C. F. Van Loan, *Matrix Computations*. JHU press, 2012, vol. 3.
- [42] Y. Wang, Q. Wang, J. Liu, Q. Zeng, J. Zheng, W. Kainz, and J. Chen, “On the Development of Equivalent Medium for Active Implantable Device Radiofrequency Safety Assessment,” *Magnetic Resonance in Medicine*, vol. 82, no. 3, pp. 1164–1176, 2019.
- [43] Y. Wang, S. Song, J. Zheng, Q. Wang, S. A. Long, W. Kainz, and J. Chen, “A Novel Device Model Validation Strategy for 1.5 T and 3 T MRI Heating Safety Assessment,” *IEEE Transactions on Instrumentation and Measurement*, 2020.

## A Appendix

Derivatives of Bessel functions are

$$\begin{aligned}
 \frac{d}{dx} J_0(x) &= -J_1(x) & \frac{d}{dx} J_n(x) &= \frac{1}{2} (J_{n-1}(x) - J_{n+1}(x)) \\
 \frac{d}{dx} Y_0(x) &= -Y_1(x) & \frac{d}{dx} Y_n(x) &= \frac{1}{2} (Y_{n-1}(x) - Y_{n+1}(x)) \\
 \frac{d}{dx} H_0^{(2)}(x) &= -H_1^{(2)}(x) & \frac{d}{dx} H_n^{(2)}(x) &= \frac{1}{2} (H_{n-1}^{(2)}(x) - H_{n+1}^{(2)}(x)).
 \end{aligned} \tag{A.1}$$

Electric and magnetic field of TM mode in an insulated solid wire are

$$\begin{aligned}
 \psi &= A_z \\
 E_z &= \frac{1}{j\omega\mu\varepsilon} \left( \frac{\partial^2}{\partial z^2} + k^2 \right) \psi & H_z &= 0 \\
 E_\rho &= \frac{1}{j\omega\mu\varepsilon} \frac{\partial^2 \psi}{\partial \rho \partial z} & H_\rho &= \frac{1}{\mu\rho} \frac{\partial \psi}{\partial \phi} \\
 E_\phi &= \frac{1}{j\omega\mu\varepsilon} \frac{\partial^2 \psi}{\partial \phi \partial z} & H_\phi &= -\frac{1}{\mu} \frac{\partial \psi}{\partial \rho}.
 \end{aligned} \tag{A.2}$$